

**IMAGING CHAIN SIMULATION PROGRAM FOR EARTH
OBSERVATION SATELLITE IMAGERS**

**YER GÖZLEM GÖRÜNTÜLEYİCİLERİ İÇİN
GÖRÜNTÜLEME ZİNCİRİ MODELLEME PROGRAMI**

SEVİ KÖKSAL

ASSOC. PROF. DR. ÖZLEM DUYAR COŞKUN

Supervisor

Submitted to

Graduate School of Science and Engineering of Hacettepe University

as a Partial Fulfillment to the Requirements

for the Award of the Degree of Master of Science

in Physics Engineering.

2020

ABSTRACT

IMAGING CHAIN SIMULATION PROGRAM FOR EARTH OBSERVATION SATELLITE IMAGERS

Sevi KÖKSAL

Master of Science, Department of Physics Engineering

Supervisor: Assoc. Prof. Dr. Özlem Duyar Coşkun

September 2020,118 pages

In the scope of this thesis study, it is aimed to characterize the imagers used in earth observation satellites by the imaging chain model method. Imager image quality performances were evaluated by using GIQE equation and NIIRS scale by imaging chain modeling. IQA (Image Quality Analysis) program was developed for imaging chain simulation. IQA program generates MTF, SNR, RER and GIQE budgets for the predefined imagers. Besides, IQA performs image simulations panchromatic and multispectral band images. Preliminary design of a multispectral TDI imager operating in panchromatic, blue, green and red bands has been made. Imaging chain links an example imager design is characterized by using IQA program. In this context, MTF, SNR, RER and GIQE performance budgets are generated under optic, electronic, platform stability and atmosphere degradations. Operational requirement budget ranges of the imager were determined by using IQA simulations. GIQE breakdown budgets with ± 0.3 are simulated for varying platform smear errors, platform jitter errors, wavefront errors, defocusing errors, number of TDI steps and solar zenith angles. Also the panchromatic image simulations related to the degradation factors are generated.

Keywords: imaging chain, MTF, PSF, RER, GIQE, NIIRS, image simulation

ÖZET

YER GÖZLEM GÖRÜNTÜLEYİCİLERİ İÇİN GÖRÜNTÜLEME ZİNCİRİ MODELLEME PROGRAMI

Sevi KÖKSAL

Yüksek Lisans, Fizik Mühendisliği

Danışman: Doç. Dr. Özlem Duyar Coşkun

Eylül 2020, 118 sayfa

Bu tez çalışması kapsamında, yer gözlem uydularında kullanılan görüntüleyicilerin görüntüleme zinciri modeli yöntemiyle karakterize edilmesi amaçlanmıştır. Görüntüleme zinciri modellenmesi ile görüntüleyiciler GIQE denklemi ve NIIRS skalası kullanılarak değerlendirilmiştir. Görüntü zinciri değerlendirmesi için IQA (Image Quality Analysis) programı geliştirilmiştir. IQA programı tasarım parametreleri belirtilen görüntüleyici için MTF, RER, SNR ve GIQE bütçelerini oluşturmaktadır. Bunun yanında IQA pankromatik ve görünür bantta bulunan renkli kanallar için görüntü modellemesi yapmaktadır. Mavi, kırmızı, yeşil ve pankromatik bantta görüntüleme yapan multi-spektral TDI algılayıcıya sahip örnek görüntüleyicinin ön tasarımı yapılmıştır. Örnek görüntüleyicinin görüntü zinciri kırımları geliştirilen IQA programı ile karakterize edilmiştir. Bu bağlamda MTF, SNR, RER ve GIQE performans bütçeleri optik, elektronik, platform stabilite ve atmosfer bozulmaları kapsamında oluşturulmuştur. Görüntü kalitesi parametresi modellemeleri kullanılarak görüntüleyicinin operasyonel gereksinim bütçe aralıkları belirlenmiştir. Lineer platform hız hatası, rastgele platform hız hatası, dalga cephesi hatası, odaklanma hatası, TDI adım sayısı ve değişen güneş zenit açısı

değerlerine bağılı GIQE kırımım bütçeleri ± 0.3 hata payıyla pankromatik görüntü çıktılarıyla beraber modellenmiştir.

Anahtar kelimeler: görüntüleme zinciri, MTF, PSF, RER, GIQE, NIIRS, görüntü simülatörü

ACKNOWLEDGEMENT

This thesis is a result of the collaboration of my work in Turkish Aerospace Optics and Radar Systems Division and my graduation project in the department of Physics Engineering at Hacettepe University. Incredible effort and patience is concluded in this study. This thesis could not exist without the support of following people:

Foremost, I would like to express my sincere gratitude to my supervisor Assoc. Prof. Dr. Özlem Duyar Coşkun for giving me opportunity to do research with her and providing guidance during my thesis study. Her patience, motivation, visionary attitude and immense knowledge help me in all steps of this study. I would like to thank to my colleagues at Hacettepe University Thin Film Preparation and Characterization Laboratory for sharing their useful opinions on my project. I am thankful to express my gratitude to Dr. Özgür Selimoğlu for generously sharing his knowledge on imaging chain modeling and electro-optical payload design for my thesis study.

I would also like to express my deepest gratitude to Turkish Aerospace for supporting me through my graduation education and motivating me to study in this thesis topic.

I would like to thank to my parents Dr. Zehra Tülin Yenilmez and Kemal Yenilmez for their supportive manners, and endless encouragement throughout my entire education life. I know that this thesis study means a lot for you both. And finally, I acknowledge my beloved husband, Yusuf Ziya Köksal, for supporting me endlessly during this thesis study.

Sevi Köksal

2020, Ankara

CONTENTS

ABSTRACT	I
ÖZET	II
ACKNOWLEDGEMENT	IV
CONTENTS	V
LIST OF TABLES	VII
LIST OF FIGURES	IX
ABBREVIATIONS AND SYMBOLS.....	XII
DEFINITIONS	XVIII
1 INTRODUCTION	1
2 IMAGE QUALITY ANALYSIS PROGRAM	3
2.1 IQA Inputs	3
2.1.1 Spectral Transmission Data Input.....	4
2.1.2 EOIPL Design Parameter Inputs	4
2.1.3 Viewing Geometry and Atmospheric Condition inputs.....	5
2.1.4 MTF Optimization Parameter Inputs.....	9
2.1.5 Constant input and calculation sensitivity parameters of IQA	11
2.1.6 Input Image	12
2.2 Imaging Chain Model	14
2.3 NIIRS Rating Calculation Module by Using GIQE v4. Model	22
2.3.1 Ground Sampling Distance.....	24
2.3.2 Sampling, Sampling Quality and Aliasing	24
2.3.3 Modulation Transfer Function and Relative Edge Response.....	26
2.3.4 Signal to Noise Ratio (SNR) Calculation	41
2.4 Image Simulation Module.....	46
2.4.1 Digital Number to Band Average Albedo Conversion	47
2.4.2 Band Average Surface Albedo to TOA Radiance Conversion.....	49
2.4.3 Applying Polychromatic MTF to Spectrally varying TOA Radiance	53
2.4.4 GSD Resampling.....	57

2.4.5	Image Radiance to Photoelectron Count per Pixel Conversion	58
2.4.6	Noise Addition to Photo-electron Count	58
2.4.7	Photoelectron Count to Digital Number Conversion.....	60
2.5	IQA Operational Flow and IQA Outputs.....	62
3	EXAMPLE EO IPL DESIGN	63
4	RESULTS	68
5	CONCLUSION	78
	REFERENCES	80
	APPENDIX-A PAPERS PUBLISHED FROM THESIS WORK	86
	CIRRICULUM VITAE	93

LIST OF TABLES

Table 2.1.3.1. Model atmosphere input parameters of PcModWin5 program used in IQA simulations	7
Table 2.1.3.2. Surface parameters of PcModWin5 program used in IQA simulations	7
Table 2.1.3.3. Solar Irradiance Parameters of PcModWin5 program used in IQA simulations	7
Table 2.1.3.4. Aerosol Parameters of PcModWin5 program used in IQA simulations	8
Table 2.1.3.5. Geometry and Spectral Band of PcModWin5 program used in IQA simulations	8
Table 2.1.3.6. Solar/Lunar Geometry (3A1) – Run Number 1 of 1 of PcModWin5 program used in IQA simulations	9
Table 2.1.4.1. MTF subcomponents are calculated by selecting the optimized parameter necessary to achieve MTF optimization input values	11
Table 2.1.5.1. Constant parameters of IQA program.	11
Table 2.1.5.2 Calculation sensitivity parameters of IQA program.....	12
Table 2.1.3. Estimated mean albedo values for RGB bands.....	14
Table 2.3.1. GIQE v.4 coefficients for visible imagery	23
Table 2.3.2. Validation cases of GIQE v.4. Equation	24
Table 2.4.3.1. Polychromatic MTF equations included in image simulation module of IQA program.....	55
Table 3.1. Commercial high resolution electro-optic imaging satellites	64
Table 3.2. EOIPL system design parameters.....	67
Table 4.1. MTF calculations are validated by using GENSAT1 and GENSAT2 designs included in Picasso and ICS articles	69
Table 4.2. SNR at constant albedo calculations are validated by using GENSAT2 design included in ICS article	69

Table 4.3. MTF breakdown of example EO IPL.....	72
Table 4.4. Optimized degradation parameters of example EO IPL.....	73
Table 4.5. GIQE budget simulations with ± 0.3 error for example EO IPL.....	73
Table 4.6. Smear GIQE budget with ± 0.3 error of example EO IPL.....	73
Table 4.7. Jitter GIQE budget with ± 0.3 error for example EO IPL.....	74
Table 4.8. Defocusing GIQE budget with ± 0.3 error for example EO IPL.....	75
Table 4.9. WFE GIQE budget with ± 0.3 error for example EO IPL.....	76
Table 4.10. GIQE budget with ± 0.3 error depending on TDI level for PAN band.	76
Table 4.11. GIQE budget with ± 0.3 error depending on TDI level for MS band.	77
Table 4.12. GIQE budget with ± 0.3 error depending on SZA change.....	78

LIST OF FIGURES

Figure 2.1. Image quality analysis (IQA) program simulates the GIQE v.4. model and image outputs by using EO IPL system inputs and optimization parameters.	3
Figure 2.1.2.1. EO IPL design parameters are entered into IQA program between eighth and twenty-second lines.	5
Figure 2.1.3.1. Viewing geometry of the EO IPL design.....	6
Figure 2.1.3.2 Viewing geometry and atmospheric conditions are specified in IQA MATLAB program between the twenty-seventh and thirty sixth lines	9
Figure 2.1.4.1. Image quality degradation factor optimization algorithm of IQA program.....	10
Figure 2.1.4.2. MTF optimization parameters input in IQA program.....	10
Figure 2.1.6.1. Sample image is downloaded from USGS data server. Albedo control points for 0100UUUTAR and 0425UUUASP materials are selected from the example image input.	13
Figure 2.2.1. Each pixel on a digital image represents a DN. Maximum DN is represented by DR.	15
Figure 2.2.2. Imaging chain model is used throughout GIQE model calculation.	16
Figure 2.2.3. An object plane radiance distribution is sampled by using delta function decomposition.	16
Figure 2.2.4. Fourier transform decomposes a digital image to its sinusoidal subcomponents with varying spatial frequencies.	18
Figure 2.2.5. Fourier transform of a sinusoidal subcomponent is defined by delta function	19
Figure 2.2.6. Sinusoidal subcomponent of an radiance decomposition.	21
Figure 2.3.2.1. Balancing Q parameter in EO IPL design Characteristics of the image quality is depending on whether the spatial resolution is limited by optics or detector	26

Figure 2.3.3.1. Satellite level MTF breakdown of IQA program includes payload, atmosphere turbulence and platform stability degradations.	27
Figure 2.3.3.2 Atmosphere degradations due to random refractive index fluctuations in IQA program are simulated by spatially averaging the radiance data on each pixel.	33
Figure 2.3.3.3 Linear motion error is defined as the spatial averaging of the distance which is determined by the product of the velocity mismatch along the boresight and the integration time in IQA program.	34
Figure 2.3.3.4. Effects of the random motion errors on image quality is defined by the Gaussian distribution function in IQA program	35
Figure 2.3.3.5. TDI degradation arises because of the clocking rate mismatches in the FPA	36
Figure 2.3.3.6. Knife edge targets are used for MTF and RER measurement from space	37
Figure 2.3.4.1. Orbit scheme of a satellite.	42
Figure 2.3.1. Flow chart of the image simulation process depending on GIQE model simulated by IQA program.	47
Figure 2.4.1.1. Spectral surface albedo data of 0425UUUASP and 0100UUUTAR downloaded from ECOSTRESS spectral library	48
Figure 2.4.1.2. Global albedo measurement taken by MODIS	49
Figure 2.4.2.1. Light paths included in MODTRAN simulation atmospheric model scheme	50
Figure 2.4.2.2. Example 40 SZA signal and haze data calculation by using MODTRAN and IQA	52
Figure 2.4.3.1. Spatial and spectral resolution scale of polychromatic MTF is calculated by using MTF optimization parameters simulated in GIQE model and spectral radiance data generated by MODTRAN program.	54
Figure 2.4.3.2. After taking the Fourier transform center of the TOA radiance spectrum is shifted to match the scale of polychromatic MTF function.	56
Figure 2.4.3.3. Degraded radiance spectrum is calculated by multiplying MTF and TOA radiance spectrum simulations.	57
Figure 2.4.6.1. Quantization noise example	59

Figure 2.4.7.1. Quantum step equivalence is the slope between number of electrons in the well and the DR.....	61
Figure 2.5.1. Operational flow of the IQA program.....	62
Figure 2.5.2. GIQE output is generated as a table in “.fig” file format.	63
Figure 3.1. Cassegrain telescope example simulated in ZEMAX.....	65
Figure 3.2. Subpixel design of the example EOIPL detector	65
Figure 3.3. Multispectral TDI detector architecture of the EOIPL design.....	66
Figure 3.4. Total spectral transmission for example EOIPL design.....	68
Figure 4.1. Image simulation outputs of IQA program for Picasso GENSAT1(left) and ICS GENSAT2 (right), respectively.	70
Figure 4.2. IQA PAN (top), blue (lower left), green (lower middle) and red (lower right) band image simulations for example EOIPL design, respectively.....	71
Figure 4.3. PAN band image simulations for no smear (left), 0.1 pixel smear (middle) and 0.15 pixel smear (right) degraded image simulations, respectively.	74
Figure 4.4. PAN band image simulations for EOIPL design (left), 0.3 pixel jitter (middle) and 0.6 pixel jitter (right) degraded image simulations, respectively. .	74
Figure 4.5. PAN band image simulations for EOIPL design (left), 0.25 peak to peak WFE (middle) and 0.5 peak to peak WFE (right) degraded image simulations, respectively.	75
Figure 4.6. PAN band image simulations for EOIPL design (left), 0.10 λ WFE (middle) and 0.15 λ WFE (right) degraded image simulations, respectively.....	76
Figure 4.7. PAN band image simulations for 32 TDI step (left), 16 TDI step (middle) and 8 TDI step (right) degraded image simulations, respectively.	77

ABBREVIATIONS AND SYMBOLS

Abbreviations

2D	Two Dimensional
ADC	Analog to Digital Converter
AFRL	Air Force Research Laboratory
DN	Digital Number
DR	Dynamic Range
DSF	Diffraction Spatial Frequency
EOIPL	Electro-Optic Imaging Payload
ERF	Edge Response Function
ERQ	Edge Response Equation
ESF	Edge Spread Function
FWC	Full Well Capacity
FWHM	Full Width Half Maximum
FPA	Focal Plane Array
FT	Fourier Transform
GIQE	General Image Quality Equation
GRND RFLT	Ground Reflected
GSD	Ground Sampling Distance
IQA	Image Quality Analysis
IR	Infrared
IRARS	Imagery Resolution and Reporting Standards
ISR	Input Spectral Radiance
LSI	Linearly Shift Invariant

JPL	Jet Propulsion Laboratory
MCPI	Multispectral Cassegrain Pushbroom Imager
MODIS	Moderate Resolution Imaging Spectrometer
MODTRAN	Moderate Resolution Atmospheric Transmission
MS	Multispectral
MTF	Modulation Transfer Function
MTFC	Modulation Transfer Function Compensation
NASA	National Aeronautics and Space Administration
NIIRS	National Image Interpretability Rating Scale
NIR	Near Infrared
NSF	Nyquist Spatial Frequency
OTF	Optical Transfer Function
PAN	Panchromatic
PSF	Point Spread Function
PTF	Phase Transfer Function
QSE	Quantum Step Equivalence
RER	Relative Edge Response
RGB	Red Green Blue
SNR	Signal to Noise Ratio
SOL SCAT	Solar Scattered
SR	Surveillance and Reconnaissance
SSP	Sampling Spatial Frequency
SZA	Sun Zenith Angle
TDI	Time Delay Integration
TOA	Top of Atmosphere
WFE	Wavefront Error
QSE	Quantum Step Equivalence

Symbols

α_{abs}	Absorption Coefficient
a.u.	Arbitrary Unit
GSD_{across}	Across Direction Ground Sampling Distance
GSD_{along}	Along Direction Ground Sampling Distance
h	Altitude
$A(x_0, y_0)$	Aperture Function
d_{atm}	Atmosphere Smear
$L_{bs}(\lambda)$	Backscattered Radiance Coefficient from the Atmosphere
V_{charge}	Charge Motion Velocity
G_c	Conversion Gain
l	Correlation Length
d_{smear}	Detector Smear Error
L_D	Depletion Width
L_{diff}	Diffusion Length
f_{optics}	Diffraction Spatial Frequency Cut off
δ	Dirac-Delta Function
$E_{g\lambda}$	Downwelling Spectral Irradiance on the Surface.
$B(\lambda)$	Downwelling solar radiation
$A(\lambda)$	Downwelling Solar Radiation that Reaches TOA After Reflected from the Object
m_{earth}	Earth Mass
D_{earth}	Earth Radius
f_{eff}	Effective Focal Length
E	Electric Field Strength
f_{factor}	Fill Factor

$FT(\lambda)$	Filter Transmission
GSD_{GM}	Geometrical Mean Ground Sampling Distance
$REER_{GM}$	Geometrical Mean Relative Edge Response
G_{grav}	Gravity Constant
$L_{GR}(\lambda)$	Ground Reflected Radiance
V_{grnd}	Ground Velocity
T_{int}	Integration Time
$I(x, y)$	Intensity of Light
σ_{jitter}	Jitter Motion Standard Deviation
D	M1 Mirror diameter
λ_{max}	Maximum Wavelength of the Spectral Band
λ_{min}	Minimum Wavelength of the Spectral Band
λ_{mean}	Mean Wavelength
G	Noise Gain
$n_{noise_added}(x, y)$	Noise Added Photo-electron Count
L_h	Haze
n_{photon}	Number of Photon Reaching the Detector Plane
V_{object}	Object Motion Velocity
D_{obs}	Obscuration Diameter
e	Obscuration Rate
H	Overshoot Ratio
W_{pp}	Peak to Peak Wavefront Error
d_{blur}	Platform Smear
h_p	Planck Constant
$P(x, y)$	Pupil Function
d	Pixel Displacement

p	Pixel Pitch Size
R	Propagation Distance of Light
f_r	Radial Spatial Frequency
$\phi_{aperture}$	Radiant Flux Reaching the Entrance Aperture of the Camera
ϕ_{image}	Radiant Flux Reaching the Imaging Plane Inside the Camera
$nd_{(x,y)}$	Randomly Distributed Matrix
σ_{read_noise}	Read Noise
$f_{sampling}$	Sampling spatial frequency cut off
Q	Sampling Quality
m_{sat}	Satellite Mass
V_{orb}	Satellite Orbital Velocity
$L_s(\lambda)$	Signal
SNR_r	Signal to Noise Ratio at Constant Albedo
SNR_{GIQE}	Signal to Noise Ratio in GIQE v.4
f	Spatial Frequency
f_x	Spatial Frequency Changing Along x
f_y	Spatial Frequency Changing Along y
Δf	Spatial Frequency Increment
$L(\lambda)$	Spectral Radiance Data
$QE(\lambda)$	Spectral Quantum Efficiency
c	Speed of Light
$S(\lambda)$	Spherical Albedo Coefficients of MODTRAN
$L_{SS}(\lambda)$	Solar Scattered Radiance
σ_{noise}	Standard Deviation of Total Noise
ρ_λ	Surface Spectral Albedo

d_{error}	TDI error
$TT(\lambda)$	Total Spectral Transmission
$\sigma_{uniform}$	Standard Deviation of Uniformly Distributed Function
$E_{u\lambda}$	Upwelling Spectral Irradiance Emitted from the Surface
λ	Wavelength
ν_n	Wavenumber
N	Quantization
σ_{noise}	Quantization Noise

DEFINITIONS

Defocusing: Focusing error arise when the distance between the optical elements and the imaging plane does not meet the pre-designed length,

Depletion Width: Depth of the depletion region from the detector surface,

Diffraction Spatial Frequency Limit: Maximum spatial frequency that is limited by the diffraction (aperture size, focal length, wavelength),

Diffusion Length: Distance that the generated photoelectrons can randomly walk,

Full Well Capacity: maximum electron count that detector holds without saturating,

Edge Response: Image radiance data distribution along the knife edge transition,

Ground Sampling Distance: The distance where the pixel size projected on the ground,

Mirror RMS error: Root mean square of the statistically derived optical path difference on the wave front,

Modulation Depth: Defines the contrast,

Modulation Transfer Function: Defines the systems modulation response to varying spatial frequencies from zero to infinity,

Noise Gain: Amplification of the noise caused by Modulation Transfer Function Compensation,

Nyquist Frequency: Maximum spatial frequency limit that an imaging system can sample while avoiding aliasing,

Overshoot Ratio: Peak value of the normalized edge response after Modulation Transfer Function Compensation, (geometric height of overshoot due to post-processing image sharpening),

Phase Transfer Function: Measure of the change in the phase of the waves at each spatial frequency,

Pixel Smear: Smear effect on the image caused by the mismatch between the charge packet velocity and the boresight stability, in another words, pixel clock rate and image scan velocity mismatch results on the image,

Polychromatic Modulation Transfer Function: Defines the systems modulation response to varying spatial frequencies and wavelength,

Quantization Noise: Noise rising from the uncertainty in the level of the signal electron counts inside the corresponding quantization step depth,

Read Noise: Noise rising from the variations on reading voltage level,

Relative Edge Response: Difference between the half pixel shifted edge response function values from the edge center,

Sampling Quality: Ratio between the sampling spatial frequency limit and the optical spatial frequency limit,

Sampling Spatial Frequency Limit: Maximum spatial frequency that is limited by the sampling (pixel size),

Signal to Noise Ratio: Ratio between the signal count electrons and the system noise,

Spatial Frequency: Smallest distance between two dots in the object plane that is still be resolved in the image,

Transfer Charges: the number of charge transfers to the output amplifier,

Wavefront Error: Optical path difference errors on the entire wave front,

Wavefront Ripple Amplitude: Normalized spatial frequency of the correlation length (used for a tuning parameter to fit the WFE MTF models to measured optical data).

1 INTRODUCTION

Electro-optic imaging systems are widely used for acquiring intelligence data in Surveillance and Reconnaissance (SR) systems [1]. The most significant purpose of the SR systems is to collect high quality image data covering wide target area. Image data with high resolution serves an important role in many applications like security, environmental imaging and disaster urgent action planning [2-4]. Requirement sets derived from image quality and mechanical design budgets bring out heavier and larger satellite design solutions. As an example a larger telescope aperture increases the light gathered by the camera. Due to these design criteria satellite solutions become very expensive.

Relating the image quality parameters to the final information extracted from the image is held by performance prediction model applications. Image quality performance prediction approaches are influential methods for evaluating the EO IPL (Electro-optic Imaging Payload) characteristics. Performance prediction approaches provide valuable information to design engineers, system engineers, image analysts and mission planning engineers. Following items can be given as examples of the image quality modeling applications:

- i. estimating how various physical factors affect the image quality,
- ii. selecting system subcomponents by using similar metrics,
- iii. predicting image quality budget on payload and satellite level during system engineering applications,
- iv. evaluating the EO IPL calibration parameters during mission planning,
- v. understanding the image quality better on the end-users perspective, how each image quality parameter effect the real image,
- vi. constituting the requirements set of the platform that EO IPL is assembled,
- vii. optimizing the EO IPL design parameters.

Ability of the observer to extract information from a scene is based on ability to detect sharp edges and tonal changes in the scene for various imaging conditions. The existence of noise and blurring in the image degrade the image quality performance. Also the spectral, spatial and radial resolution defines the imaging sensitivity of the EO IPL. Physical image quality parameters and image simulations are used for predicting the EO IPL performance. There are numerous examples of imaging chain analysis of EO IPLs in literature[5-11].

Performance measurement methods and metrics used in extracting information are derived from physical image quality metrics and EOIPL design parameters.

NIIRS (National Image Interpretability Rating Scale) ratings are used to identify the maximum level of useful information that can be extracted from an image and to relate the image interpretability to the physical image quality parameters [12-14]. Interpretation tasks like large facility detection and small target identification with varying difficulties are categorized to standardize the image quality evaluation of EOIPL's [12]. Image quality performance goals are described by using NIIRS scale. GIQE (General Image Quality Equation) is used for predicting the NIIRS performance of an EOIPL. GSD (Ground Sampling Distance), RER (Relative Edge Response) and SNR (Signal to Noise Ratio) are the parameters which GIQE considered during NIIRS scale evaluation [15]. These parameters are simulated by a model called imaging chain [12, 14, 16].

The main purpose of this thesis is to design an image quality evaluation program which relates the physical parameters to the final image simulation extracted from the EOIPL. In this context, an imaging chain simulation program, IQA (Image Quality Analysis), was developed. GSD, SNR and RER parameters are calculated by using IQA program. Also image simulations are generated by considering the image quality parameters calculated in GIQE calculation module. An example EOIPL design with multispectral pushbroom architecture was made by using iterations of IQA program to achieve NIIRS scale of 5 for panchromatic (PAN) band and NIIRS scale of 4 for multispectral (MS) band. The EOIPL design parameters necessary to achieve predefined image quality values are generated. At last the requirement set from the satellite system and atmosphere degradations were calculated.

First of all in chapter 2 the inputs, theoretical background, outline, operational flow and the outputs of the IQA program will be outline. GIQE calculation and image simulation algorithms used in IQA program are defined. In chapter 3 a preliminary design step for a submeter resolution multispectral EOIPL design is shown. Finally, in chapter 4, outputs generated from IQA program by using EOIPL design parameters are given. The validation of MTF optimization algorithm and SNR calculation is given in chapter 4. Also the GIQE breakdown for different imaging condition scenarios are generated for each degradation links in the imaging chain.

2 IMAGE QUALITY ANALYSIS PROGRAM

Image Quality Analysis program lets user to predict the image quality performance of Multispectral Cassegrain Push broom (MCP) EOIPL within NIIRS scale. Version 4 of GIQE is simulated by using imaging chain model during performance evaluation. PAN and RGB band image simulations of the calculated GIQE output are generated within visible band. Image Quality Analysis (IQA) program can be used during design, performance prediction and operational steps of an EOIPL. Outline of the IQA program is given in Figure 2.1.

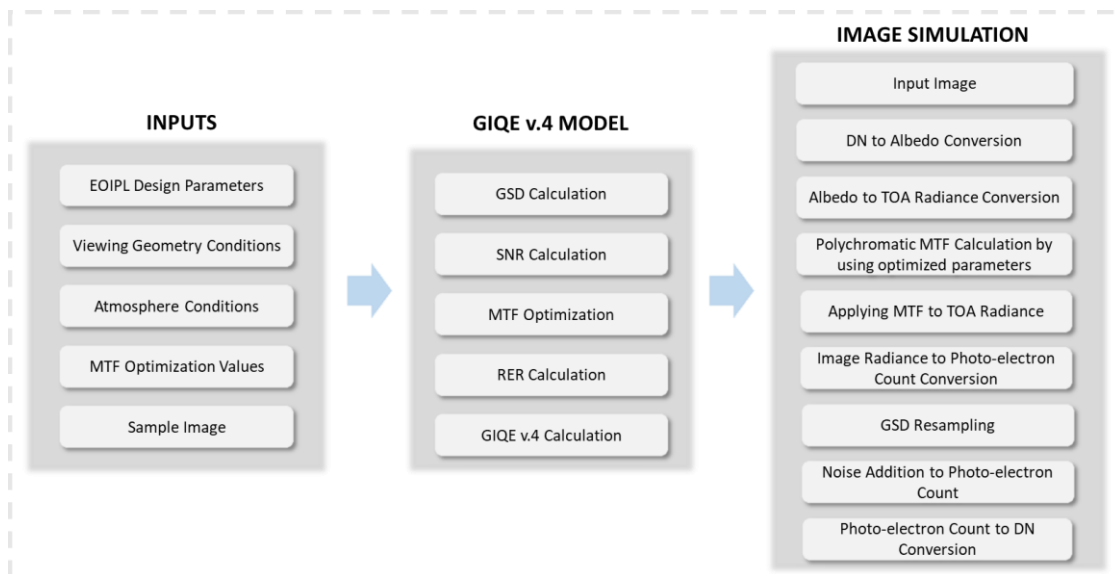


Figure 2.1. Image quality analysis (IQA) program simulates the GIQE v.4. model and image outputs by using EOIPL system inputs and optimization parameters.

2.1 IQA Inputs

Main inputs of the IQA program are the EOIPL design parameters, viewing geometry, atmosphere conditions, MTF optimization values, number of TDI steps and a sample image with high spatial and spectral resolution. GIQE model and image simulations are calculated by considering the optimization and design parameter inputs. Following inputs should be set up before running the IQA MATLAB program.

- spectral transmission excel file,
- EOIPL design parameters in IQA Program,

- viewing geometry in IQA program,
- atmospheric conditions in IQA program,
- MTF optimization parameters in IQA program,
- calculation sensitivity parameters in IQA program

2.1.1 Spectral Transmission Data Input

Spectral transmission data file applicable for IQA program consists of an excel file containing wavelength data in the first column and total spectral transmission data in the second column respectively. The excel file format should contain the following rules:

- The first element of wavelength and spectral transmission data must be included in A2 and B2 cells, respectively,
- The spectral range included in spectral transmission data should be between 400 nm and 1000 nm. For wavelength increments which there are no light transmission spectral transmission must be set 0,
- Sheet 1 should contain PAN spectral transmission data,
- Sheet 2, Sheet 3 and Sheet 4 should contain the blue, green, and red band transmission data, respectively.

2.1.2 EOIPL Design Parameter Inputs

IQA program calculates the GIQE model and simulates the image which is related to the GIQE model by taking into EOIPL design parameter inputs. EOIPL design inputs should be specified between the eighth line and the twenty-second line of the IQA MATLAB program as given in the example included in Figure 2.1.2.1.

```

8 % EO IPL design parameters
9 - aperture = 690; % M1 diameter (mm)
10 - obsrate = 0.1; % obscuration diameter / M1 diameter
11 - focallength = 12000; % focal length (mm)
12 - pixel = 0.01; % PAN pixel pitch size (mm)
13 - pixel_MS = pixel*4; % MS pixel pitch size (mm)
14 - meanwavelength = 575*10^-6; % mean wavelength of PAN band (mm)
15 - Read_Noise = 50; % read noise (e-)
16 - FWC = 15000; % full well capacity (e-)/pixel
17 - fill_factor = 1; % detector fill factor
18 - Np = 4; % number of phase for scanning CCD
19 - quantization = 12; % ADC Quantization
20 - TDI = 32; % Number of TDI Steps
21 - gain = 1.8; % conversion gain
22 - smear pixel d = 0.00001; % PAN Pixel Detector Smear (pxl)

```

Figure 2.1.2.1. EO IPL design parameters are entered into IQA program between eighth and twenty-second lines.

Aperture size, obscuration rate and focal length parameters represents the telescope while, the pixel size, read noise, full well capacity, phase number, quantization, TDI, mean wavelength and conversion gain parameters indicates the characteristics of the focal plane assembly (FPA).

2.1.3 Viewing Geometry and Atmospheric Condition inputs

The IQA program is designed to characterize the image quality of EO IPL observing the ground in nadir case. EO IPL scan direction parallel to satellite orbital motion is defined as along scan direction in Push broom imaging geometry. The direction perpendicular to the along scan direction is defined as across scan direction. Projection of each TDI line in the across scan direction covers the swath width of the EO IPL on the ground. Reflected radiance from GSD is degraded by atmosphere and finally accumulated as photo-electrons in detector. Viewing geometry included in the IQA program is illustrated in Figure 2.1.3.1

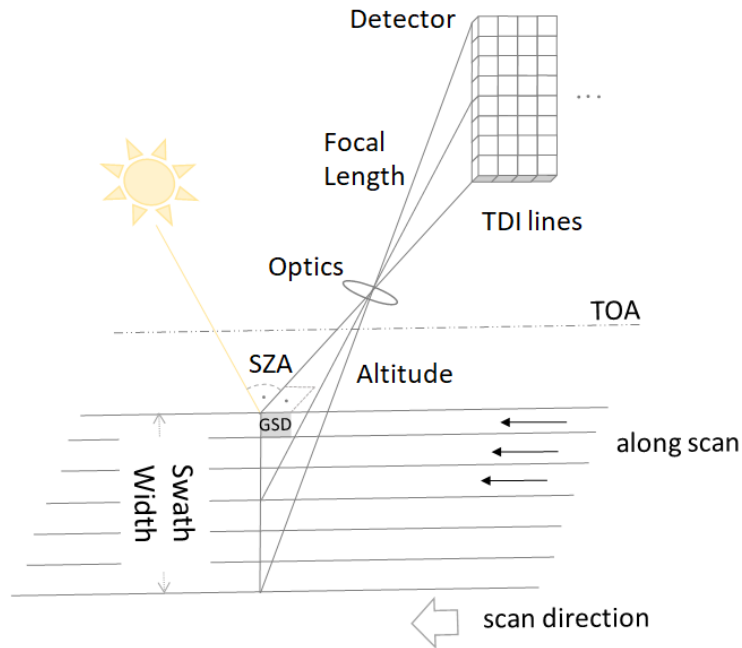


Figure 2.1.3.1. Viewing geometry of the EOIPL design.

Viewing conditions of the IQA simulations consist of two-path light propagation geometry as it can be seen in the Figure 2.1.3.1. Especially the SNR and the image simulations are strongly dependent on the spectral transmission characteristics of the atmosphere. The spectral transmission characteristics of the sun illumination are strongly dependent on the SZA and atmospheric conditions. This two-path light propagation spectral characteristics of the atmosphere are evaluated by using spectral radiance data generated with MODTRAN radiative transfer code. Model atmosphere, surface parameters, solar irradiance, aerosol, geometry and spectral band and Solar/Lunar geometry (3A1) – Run Number 1 parameters are kept as constants included in Table 2.1.3.1, Table 2.1.3.2, Table 2.1.3.3, Table 2.1.3.4, Table 2.1.3.5 and Table 2.1.3.6, respectively. A spectral radiance data library is generated and embedded in IQA MATLAB program by using PcModWin5 program. Input Spectral Radiance (ISR) values are generated for following conditions:

- SZA (0°, 10°, 20°, 25°, 30°, 40°, 45°, 50°, 60°, 70°, 75°)
- Albedo (0.07, 0.15, 0.20, 0.30, 0.70)
- Atmosphere Model (Midlatitude Summer Model, Midlatitude 1976 Summer Model, Midlatitude Winter Model)

Table 2.1.3.1. Model atmosphere input parameters of PcModWin5 program used in IQA simulations.

Parameter	Value
Calculation Option	MODTRAN
Model Atmosphere	Mid-Latitude Summer
Type of Atmospheric Path	Slant Path to Space of Ground
Mode of Execution	Radiance with Scattering
Execute with Multiple Scattering	No Multiple Scattering
Temperature and Pressure Altitude Profile	Default to Model
Water Vapor Altitude Profile	Default to Model
Ozone Altitude Profile	Default to Model
Methane Altitude Profile	Default to Model
Nitrous Oxide Altitude Profile	Default to Model
Carbon Monoxide Altitude Profile	Default to Model
Water Vapor Column Choices	Use default water vapor column
Ozone Column Choices	Use default ozone column
CO2 Mixing Ratio (ppm)	400

Table 2.1.3.2. Surface parameters of PcModWin5 program used in IQA simulations.

Parameter	Value
Surface Albedo Flag	Use Surface albedo value
Surface Albedo (PAN,R,G,B)	variable
Surface Albedo (NIR)	variable
Temperature at First Boundary	0

Table 2.1.3.3. Solar Irradiance Parameters of PcModWin5 program used in IQA simulations.

Parameter	Value
Spectral Triangular Filter Function	Use Default Top-Of-Atmosphere (TOA) Solar-Data
Top of Atmosphere Parameters	Do not scale TOA irradiance

Table 2.1.3.4. Aerosol Parameters of PcModWin5 program used in IQA simulations.

Parameter	Value
Aerosol Model Used	Rural - Vis = 23km
Seasonal Modification to Aerosol	Spring-Summer
Aerosol Optical Properties	Default properties
Stratospheric Aerosols (2-30 km)	Background Stratospheric
Air Mass Character for Navy Maritime Aerosols	0
Surface Meteorological Range (VIS)	0
Rain Rate (mm/hr)	0
Ground Altitude Above Sea Level (km)	0

Table 2.1.3.5. Geometry and Spectral Band of PcModWin5 program used in IQA simulations.

Parameter	Value
Path Type	Observer Height, Zenith Angle
Observer Height (km)	120
Zenith Angle (°)	180
Initial Frequency (nm)	1000
Final Frequency (nm)	400
Slit Function Type	Triangular
FWHM Type	Absolute
Type of Plot out Output	Radiance
Plot out File Units	Micrometers
Degrade Type	Only Total Rad/Trans
Spectral flux table	Omit spectral flux table
Spectral Flux Atmospheric Levels to Output	0
Index of Refraction Profile spectral Frequency (1/cm)	0
Slant Range for K-distribution output	Default : Full slant range data only
Slant Range (km)	0

Table 2.1.3.6. Solar/Lunar Geometry (3A1) – Run Number 1 of 1 of PcModWin5 program used in IQA simulations.

Parameter	Value
Solar/Lunar Geometry Type	Azimuth and Zenith Angle
Aerosol Phase Function	MIE Generated
Day of Year	1
Extraterrestrial Source	Sun
Azimuth Angle at Observer LOS to Sun	0
Sun Zenith Angle (°)	variable

Altitude, Sun Zenith Angle (SZA), boresight stability motion error and atmosphere model inputs are specified for the viewing geometry and atmospheric condition inputs of IQA program between the twenty-seventh and thirty sixth lines of the IQA MATLAB program as included in the Figure 2.1.3.2.

```

26 % geometry input parameters
27 - altitude = 600*1000; % (m) altitude
28 - SZA = 40; % sun zenith angle (degrees) among [0 - 10 - 20 - 25 - 30 - 40 - 45 - 50 - 60 - 70 - 75]
29 - boresight_stability = 100; % (mm/s) for TDI MTF degradation calculations
30 - GSD_in = 0.1524; % (m) image GSD
31
32 % atmosphere model selection
33 - Atmosphere_Model = 'Mid_Latitude_Summer_Model'; % type the MODTRAN atmosphere model
34 % 'Mid_Latitude_Summer_Model' (45 degrees North, July)
35 % 'Mid_Latitude_1976_US_Standard_Model'
36 % 'Mid_Latitude_Winter_Model' (45 degrees North, January)

```

Figure 2.1.3.2 Viewing geometry and atmospheric conditions are specified in IQA MATLAB program between the twenty-seventh and thirty sixth lines.

2.1.4 MTF Optimization Parameter Inputs

IQA program calculates the degradation factors necessary to attain predefined image quality parameters. Optimization calculations are based on MTF image quality parameters. Image quality degradation factor optimization algorithm is illustrated in Figure 2.1.4.1. Each subcomponent of total system MTF can be calculated separately by using the properties of convolution product in Fourier domain. MTF datasets for varying degradation factors are generated for MTF subcomponents. Degradation factor which the NSF (Nyquist Spatial Frequency) MTF value matches the predefined degradation is selected. Optics, RMS mirror WFE, defocusing, detector, platform smear, platform jitter and atmospheric

smear are the input image quality parameters of the IQA program. The optics breakdown consists of diffraction and tolerance WFE MTF subcomponents. By degrading tolerance WFE optics subcomponent is calculated. Detector MTF is the product of footprint and diffusion MTF breakdowns. Detector MTF subcomponent is optimized by changing depletion width of the detector. Peak to peak WFE, depletion width, smear error and jitter error are optimized by taking defocusing, platform smear, platform jitter and atmosphere smear MTF values into consideration. It should be noted that WFE ripple amplitude and diffusion length parameters are kept constant during optimization calculations. Figure 2.1.4.1 represents the image quality parameter inputs and related parameters.

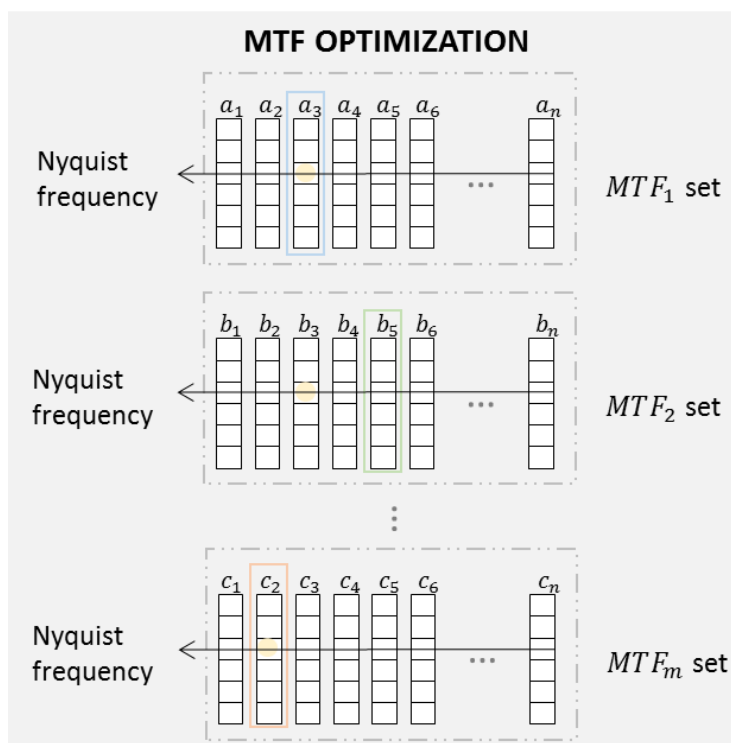


Figure 2.1.4.1. Image quality degradation factor optimization algorithm of IQA program.

```

56 % image quality optimization parameters
57 - Optics_optimization = 0.3489; % diffraction MTF*Tolerance MTF
58 - RMS_optimization = 0.9060; % RMS mirror WFE MTF
59 - Defocusing_optimization = 1; % defocusing MTF
60 - Detector_optimization = 0.59; % footprint MTF*difussion MTF
61 - Platform_smear_optimization = 1; % linear velocity mismatch
62 - Jitter_optimization = 1; % random direction & velocity mismatch
63 - Atmosphere_optimization =1; % atmosphere turbulence MTF
64 - CTE_MTF_optimization = 1; % charge transfer efficiency MTF

```

Figure 2.1.4.2. MTF optimization parameters input in IQA program.

MTF optimization parameters are determined between the fifty-sixth and sixty-fourth lines of IQA program as given in Figure 2.1.4.2.

Table 2.1.4.1. MTF subcomponents are calculated by selecting the optimized parameter necessary to achieve MTF optimization input values.

Input parameter	Optimized parameter	Constant parameters
Optics MTF	Tolerance WFE	WFE ripple amplitude
RMS mirror WFE MTF	RMS WFE	WFE ripple amplitude
Defocusing MTF	Peak to peak WFE	-
Detector MTF	Depletion width	diffusion length
Platform smear MTF	Smear error	-
Platform jitter MTF	Jitter error	-
Atmosphere smear MTF	Atmosphere smear error	-

2.1.5 Constant input and calculation sensitivity parameters of IQA

As previously mentioned, some image quality parameters kept as constant for optimization purposes. Also there are some physical constants included in the calculations of the IQA. Constant input parameters of IQA are given in Table 2.1.5.1. Calculation sensitivity parameters used in IQA simulation is given in Table 2.1.5.2.

Table 2.1.5.1. Constant parameters of IQA program.

Variable	Value	Unit
Wavefront ripple amplitude	0.1	λ
Diffusion length	150	μm
Number of charge transfers to the output amplifier	10	e^-
Gravity constant	6.673×10^{-11}	Nm^2/kg^2
Earth mass	5.98×10^{24}	kg
Earth radius	6.38×10^6	mm

Calculation sensitivity of IQA program is determined with following parameters:

- Input spatial frequency scale of the MTF calculations is ranging from zero to the system cut off spatial frequency. “div” parameter defines the

spatial frequency division sensitivity of the input spatial frequency scale. For example if div is equal to 300, spatial frequency scale is ranging from 0 to system cut off frequency with system cut off frequency/300 increment.

- Spectral resolution of the EOIPL spectral transmission data is not always in the same scale with the spectral resolution of the input radiance generated by using PcModWin5 program. For the weighting integral calculations used during SNR analysis and image simulation, input spectral radiance data set necessary to ensure the spectral resolution is selected. “wave_sensitivity” parameter defines the wavelength selection sensitivity for MODTRAN radiance data according to the spectral transmission input.
- Imaging chain subcomponent MTF graphs are optimized by calculating MTF data sets for varying degradation factors. The MTF dataset which the Nyquist frequency MTF value matches the predefined MTF is selected. Span parameter defines the sensitivity of the MTF value selection at sampling NSF.
- MTF subcomponents are calculated through input spatial frequency limited by system spatial frequency cut off. Depending on the value of the sampling quality parameter, sampling Nyquist frequency index in the input spatial frequency array is changing. “Nyquist_span” parameter defines the sensitivity of sampling Nyquist frequency selection from the input spatial frequency array.

Table 2.1.5.2 Calculation sensitivity parameters of IQA program.

Variable	Value
div	300
wave_sensitivity	3
span	0.001
Nyquist span	0.2

2.1.6 Input Image

An input image with higher or equal spectral band width, high SNR and higher spatial resolution is necessary in IQA program to simulate the degradations of the imaging chain. Ideal input scene should have infinite spectral and spatial resolution [16]. Because of the fact that it is impossible to find such ideal image, in practice a sample image that satisfies the necessities of the simulated EOIPL. It is important to state that input image should be selected depending on

which EOIPL characteristics mostly desired to evaluate. For examining how multiple multispectral bands add up to form a final image a hyperspectral input image with high spectral resolution must be applied. On the other hand for investigating the spatial resolution capabilities of the EOIPL, sample image with high spatial resolution should be preferred. It is stated that the input image should have four times better spatial resolution than the simulated EOIPL spatial resolution [16]. Despite the TOA (Top of Atmosphere) radiance can be simulated for different SZA values, shadows in the image simulations still stay fixed in the image simulation [16]. High resolution ortho-imagery of Austin Bergstrom Airport seen in Figure 2.1.6.1 with spatial resolution of 0.1524 is downloaded from the Earth Explorer data base of United States Geological Survey with 1321607_135050 entity ID. The image is taken by using RC30 aerial sensor of Leica in 2003 at Texas by CAPCOG agency. Central latitude and longitude of the sample image is (30°12'09.51"N, 97°40'16.09"W) [17]. RC30 sensor was used during 2000s to provide wide coverage ortho-imagery in Switzerland. RGB (Red Green Blue), NIR (Near Infra-red) and PAN band imagery are available in RC30. 1321607_135050 image contains red, green and blue bands. Because of RGB sensitive sensor ranges between 100 to 670 nm, it is applicable for the image simulations in the visible region [18].

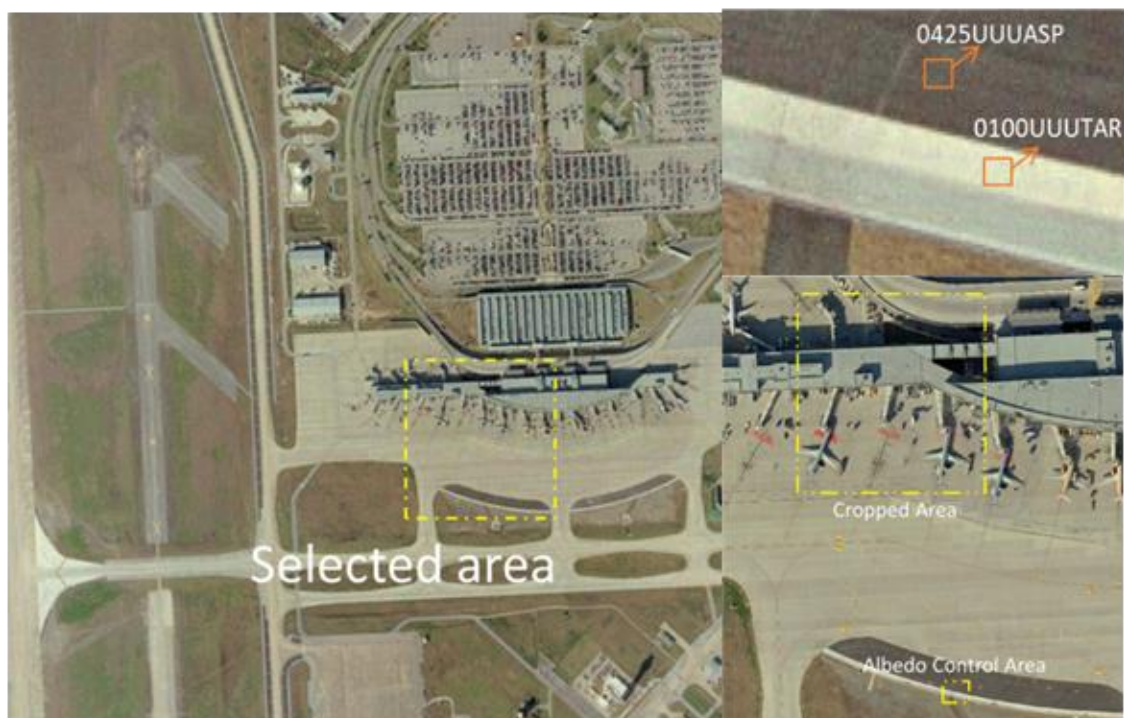


Figure 2.1.6.1. Sample image is downloaded from USGS data server. Albedo control points for 0100UUUTAR and 0425UUUASP materials are selected from the example image input.

Cropped area in Figure 2.1.6.1 is used in PAN image simulations. 9x9 pixels of 0100UUUTAR and 0425UUUASP materials are selected from Albedo Control Area in Figure 2.1.6.1. To convert sample input scene to albedo each spectral band is multiplied by mean albedo ratio. Albedo values for 0100UUUTAR are between 0.15-0.29 while albedo values for 0425UUUASP is ranging from 0.698 to 0.863. Albedo values estimated for each band are given in Table 2.1.3.

Table 2.1.3. Estimated mean albedo values for RGB bands.

Band	0100UUUTAR albedo (a.u.)	0425UUUASP albedo (a.u.)
Red	0.860	0.230
Green	0.085	0.231
Blue	0.076	0.196

After the conversion of input scene to the albedo mean albedo values average albedo values along x axis are calculated for each band. Mean albedo values in Table 2.1.3 shows good consistency with the values given in ECOSTRESS library. Mean albedo of PAN band is calculated by summing red, green and blue band mean albedo values. Finally, mean albedo value is converted to spectrally varying TOA radiance data as encountered in chapter 2.4.1.

2.2 Imaging Chain Model

A digital Image is defined as an array with each element representing a pixel. The emitted and reflected electromagnetic radiation from GSD is recorded as an integer Digital Number (DN) during each sampling interval. DN represents the amount of energy reaching the sensor depending on wavelength. Each band has a different DN value. Allowed brightness range of each pixel is defined as Dynamic Range (DR). DR in a digital image is determined by bites [14-19]. Example of a digital image is given in Figure 2.2.1 [14].

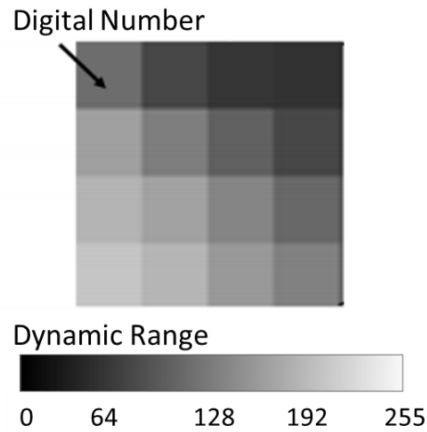


Figure 2.2.1. Each pixel on a digital image represents a DN. Maximum DN is represented by DR.

A chain of physical events like atmospheric conditions, diffraction and sampling degrades the brightness value of each pixel. Each link in this chain can be evaluated separately by common image quality metrics like GSD, SNR and RER in imaging chain model. Finally, the imaging chain is used to simulate the images that would be produced by the EO IPL [12, 14, 20, 21].

Imaging chain model is used to represent the simulated images as the convolution of the object radiance and Point Spread Function (PSF). PSF is defined as the response of the EO IPL to a single point object in linear shift invariant (LSI) systems. In LSI systems, full width half maximum (FWHM) of the blurred image of a point object does not change depending on the image location [12, 14, 22, 23]. Linearity and shift invariance are necessary to be able to represent the image simulation as a convolution process [24, 25]. In linear systems an individual PSF can be superimposed in the image plane to model image radiance distribution [20]. Incoherent imaging systems are linear in irradiance (W/cm^2), while coherent imaging systems are linear in electric field (V/cm^2) [12, 20, 26]. Because of the fact that the extraterrestrial source in the imaging chain for IQA is sun, illumination on the detector array is spatially incoherent. It should be noted that in imaging chain model nonlinearity behavior of IR band and the shift variance of the aberrations are neglected. Linearity requirements for visible band spectrum are satisfied for LSI systems. However, impulse response of the infra-red (IR) band detectors are depending on input radiance level, because of the radiance level dependence nonlinearities arises in the imaging system for IR band [26]. Also it should be considered that aberrations violate the shift invariance assumptions in LSI systems [12, 14, 20].

To prevent the violation of LSI, IQA program is applied on EOIPL systems which are operating in visible band with radially symmetrical aberration PSF.

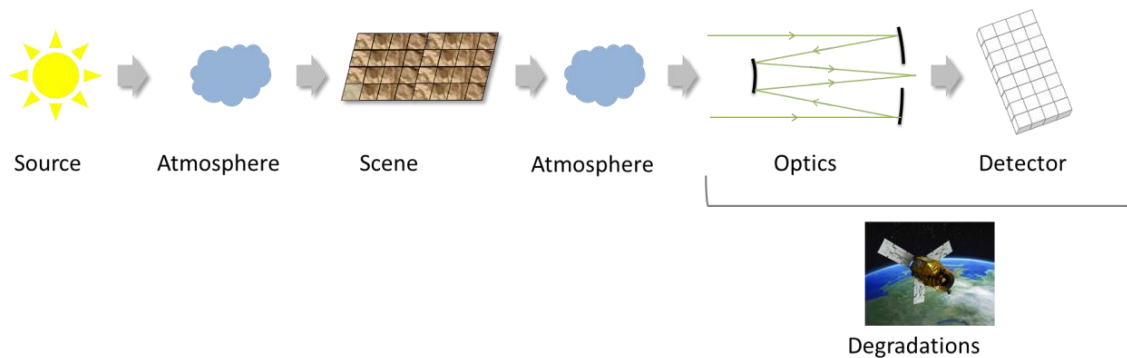


Figure 2.2.2. Imaging chain model is used throughout GIQE model calculation.

Representation of the object radiance distribution data is defined as a delta function decomposition in imaging chain simulations. A sample radiance distribution is represented by shifting and scaling properties of the delta function. In Figure 2.2.3, a delta function decomposition with x and y spatial periods is given. By using shifting property of the delta function, object radiance distribution is decomposed as spatially averaged radiance level for each GSD. Also the amplitude of the radiance data for each GSD is defined by using the scaling property of the delta function.

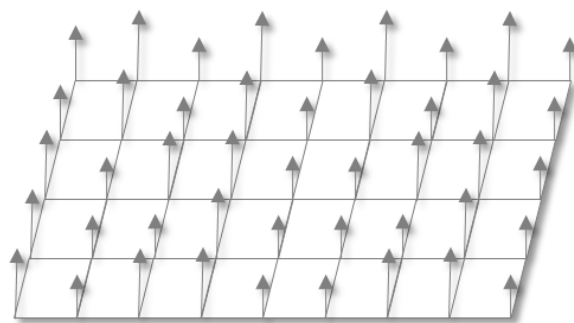


Figure 2.2.3.. An object plane radiance distribution is sampled by using delta function decomposition.

While the object radiance distribution passes through each subcomponent of the EOIPL, radiance distribution components reflected from each GSD degrade.

Finally, the object radiance distribution is converted to the image radiance distribution. Optical imaging operations are acting like linear mappings of object radiance distributions into image radiance distributions [26, 27]. Convolution product is used for defining the relationship between the image radiance distribution and the object radiance distribution in spatial domain. Linearity of the imaging system brings the ability to express the image radiance distribution as the superposition integral of the object radiance distribution and PSF. PSF is simply the weighting factor applied to the object radiance distribution. If the system is an ideal imager, had a perfect image quality, the PSF is a delta function [20]. Imaging equation can be defined as [26, 27]:

$$g(x, y) = \iint PSF(x, y ; x', y') o(x', y') dx' dy' \quad Eq. 2.1$$

$$g(x, y) = PSF(x, y) ** o(x, y) \quad Eq. 2.2$$

where $g(x, y)$ is the image radiance distribution, $o(x, y)$ is the object radiance distribution, $PSF(x, y)$ is the point spread function, (x, y) is the spatial position, (x', y') is the convolution position in the spatial domain.

Imaging chain can also be considered in spatial frequency domain with units of line pair per mm (lp/mm) [14, 20, 28]. Imaging equation in spatial frequency domain is stated as the Fourier transform in the spatial domain [20, 27, 29].

$$FT \{g(x, y) = PSF(x, y) ** o(x, y)\} \quad Eq. 2.3$$

$$G(f_x, f_y) = OTF(f_x, f_y) O(f_x, f_y) \quad Eq. 2.4$$

where $o(x, y)$ is the object radiance, $g(x, y)$ is the image radiance, $G(f_x, f_y)$ is the image radiance spectrum, $O(f_x, f_y)$ is the object radiance spectrum.

By taking the Fourier transform of object radiance distribution, it is decomposed into its sinusoidal subcomponents with varying spatial frequencies as the radiance spectrum. Schematic example of the Fourier transform of an object radiance distribution is given in Figure. The basis set of Fourier transform is composed of two-dimensional sinusoidal radiance functions and has spatial period in both x and y directions. Fourier transform example of sinusoidal

subcomponents is given in Figure 2.2.5 [14]. Fourier domain spatial frequency set is defined as $f_x = 1/x$ and $f_y = 1/y$ [20].

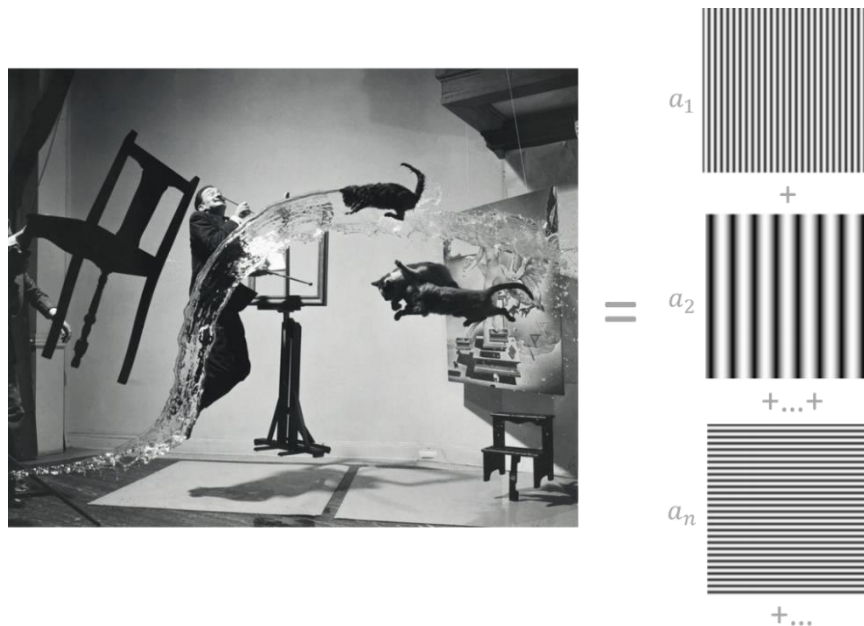


Figure 2.2.4. Fourier transform decomposes a digital image to its sinusoidal subcomponents with varying spatial frequencies.

Fourier transform of each sinusoidal subcomponent can be expressed with following equation in one dimension. A sinusoidal subcomponent function with amplitude A and bias B is given by [14]:

$$O_{a_1}(x) = A \cos(2\pi f_x x) + B \quad \text{Eq. 2.5}$$

where f_x is spatial frequency, x is spatial position.

The Fourier transform of the sinusoidal subcomponent function is expressed with [14]:

$$FT\{AO_{a_1}(x)\} = \frac{A}{2} \delta(f_x - f_{a_1}) + \frac{A}{2} \delta(f_x + f_{a_1}) + B\delta(f_x) \quad \text{Eq. 2.6}$$

where f_x is spatial frequency, x is spatial position, f_{a_1} is the spatial frequency of the sinusoidal subcomponent with a_1 weight.

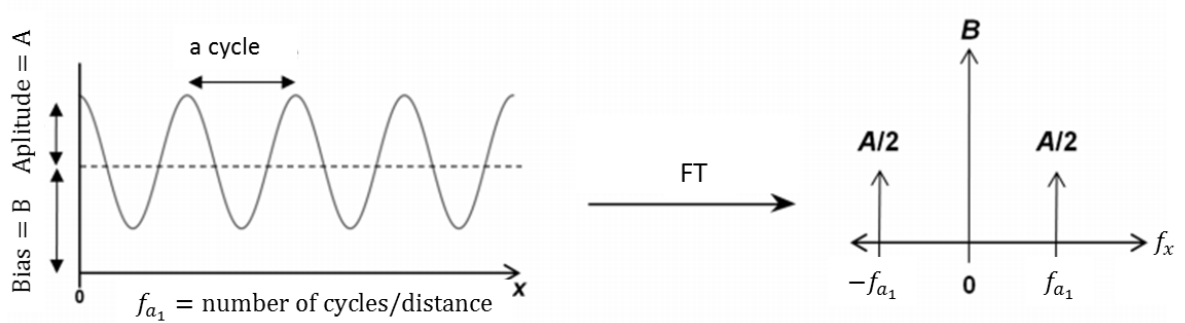


Figure 2.2.5. Fourier transform of a sinusoidal subcomponent is defined by delta function [14].

Each point on the radiance spectrum represents the spatial frequency of a sinusoidal subcomponent. Also the brightness values of the spectrum points correspond to the amplitude of the sinusoidal component. The Fourier transform of the object radiance distribution is given by [14]:

$$FT\{AO_{a_1}(x)\} = \frac{A}{2}\delta(f_x - f_{a_1}) + \frac{A}{2}\delta(f_x + f_{a_1}) + B\delta(f_x) \quad Eq. 2.7$$

$$o(x, y) = \int_{-\infty}^{\infty} \int_{-\infty}^{\infty} O(f_x, f_y) e^{2\pi i(xf_x + yf_y)} df_x df_y \quad Eq. 2.8$$

where $o(x, y)$ is object radiance, $O(f_x, f_y)$ is the object radiance spectrum, (f_x, f_y) is spatial frequency in two dimension, (x, y) is spatial position in two dimension.

Image quality degradation factors put a limit on the maximum spatial frequency that the EOIPL can sample and decreases the radiance amplitude value of each spatial frequency. Optical Transfer Function (OTF) represents the image quality degradation factors in the imaging chain and defined as the Fourier transform of the PSF. By using the convolution theorem properties OTF, MTF and PTF (Phase Transfer Function) equations can be derived by [24-26]:

$$FT\{AO_{a_1}(x)\} = \frac{A}{2}\delta(f_x - f_{a_1}) + \frac{A}{2}\delta(f_x + f_{a_1}) + B\delta(f_x) \quad Eq. 2.9$$

$$G(f_x, f_y) = OTF(f_x, f_y)O(f_x, f_y) \quad Eq. 2.10$$

$$OTF(f_x, f_y) = |OTF(f_x, f_y)|e^{-i\theta(f_x, f_y)} \quad Eq. 2.11$$

$$MTF(f_x, f_y) = |OTF(f_x, f_y)| \quad Eq. 2.12$$

$$PTF(f_x, f_y) = e^{-i\theta(f_x, f_y)} \quad Eq. 2.13$$

where $OTF(f_x, f_y)$ is optical transfer function, $PTF(f_x, f_y)$ is the phase transfer function, $MTF(f_x, f_y)$ is modulation transfer function, $\theta(f_x, f_y)$ is the phase function.

For the cases that PSF function does not satisfy the symmetry conditions, the Fourier transform of PSF is a complex function which has a magnitude term referred as MTF and PTF, respectively [20]. PTF defines the change in the phase of waves at each spatial frequency, while MTF defines the magnitude response of the optical degradations to sinusoidal functions at each spatial frequency [14]. For EOIPL with real and symmetrical PSF, PTF equals to zero. Magnitude of the Fourier transform of the PSF equals to the MTF. Each links in the imaging chain can be interpreted as multiple convolutions in the imaging equation. By using the Fourier Transform properties, total MTF of the EOIPL can be expressed as the product of the subcomponent MTF functions such as optics, detector and smear MTF [24]:

$$MTF_{system}(f_x, f_y) = MTF_{optics}(f_x, f_y) MTF_{detector} MTF_{smear} \dots \quad Eq. 2.14$$

In LSI EOIPL systems sinusoidal radiance input is imaged as another sinusoidal output with decreased amplitude. Modulation depth (contrast) is defined as the ratio of the amplitude radiance variation and bias level [20]:

$$M(f_x, f_y) = \frac{I_{max}(f_x, f_y) - I_{min}(f_x, f_y)}{I_{max}(f_x, f_y) + I_{min}(f_x, f_y)} \quad Eq. 2.15$$

where $M(f_x, f_y)$ is modulation function, $I_{max}(f_x, f_y)$ is maximum of the radiance input, $I_{min}(f_x, f_y)$ is minimum of the radiance input.

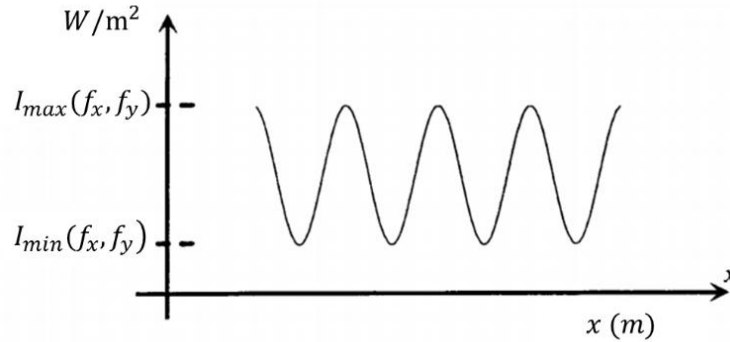


Figure 2.2.6. Sinusoidal subcomponent of an radiance decomposition.

MTF is defined as the ratio of the output modulation to the input modulation at each spatial frequency subcomponent [20, 29]:

$$MTF(f_x, f_y) = \frac{M_{out}(f_x, f_y)}{M_{in}(f_x, f_y)} \quad Eq. 2.16$$

where $M_{in}(f_x, f_y)$ is input modulation, $M_{out}(f_x, f_y)$ is output modulation.

Analytical parameters that can be modeled in IQA program by imaging chain analysis are as following [30]:

- i. Spectral radiance data,
- ii. Target characteristics (reflectivity, size and spatial characteristics of the target),
- iii. Imaging conditions (weather conditions, obscurations in the aperture, scattering in the atmosphere, altitude),

- iv. EO IPL characteristics (spectral quantum efficiency, spectral optical transmission, spectral filter transmission, optical aperture size, pixel size, detector quantum efficiency, detector diffusion, detector noise, detector quantization).

2.3 NIIRS Rating Calculation Module by Using GIQE v4. Model

IQA program calculates the GIQE parameter of EO IPL to evaluate the image quality by considering National Image Interpretability Rating Scale (NIIRS). Imaging chain model is used in GIQE parameter calculation. Ground sampling distance (GSD), Relative edge response (RER) and signal to noise ratio (SNR) parameters are calculated for evaluating the resolution characteristics of the EO IPL. Imaging chain model represents an EO IPL by considering spatial, spectral and radiometric resolutions. RER determines spatial and spectral resolutions of the EO IPL, while SNR calculation represents the spectral and radiometric resolutions. GSD is related with spatial resolution. Simulated resolution types included in IQA program are given as [19]:

- Spatial resolution: the ability to distinguish two spatially separate objects on the ground,
- Spectral resolution: ability to differentiate the difference in the albedo of the same ground objects with different wavelengths, also determined by the number of spectral bands used while splitting spectrally the radiance received from the object,
- Radiometric resolution: the ability of a remote sensing system to distinguish the difference in the intensity of the radiant energy from the object to the EO IPL, determined by the level of quantization of the converted electrical signal from radiant energy.

NIIRS is released by Imagery Resolution and Reporting Standards (IRARS) Committee in 1970's. NIIRS scale is used to understand the communication between image interpretability and physical image quality parameters. The first NIIRS scale was used to determine imaging performance of the EO IPL operating in visible band. Between 1994 and 1999 NIIRS scales covering IR, MS (Multispectral) and radar systems were published [12]. Visible image interpretability scale released in March 1994 while Multispectral Imagery Interpretability Rating Scale released in February. Leachtenauer stated that MS

NIIRS is currently under development [12]. NIIRS levels define various interpretation task descriptions used by intelligence community. Exploitation tasks that can be performed on the image is defined with NIIRS rating [30, 13].

General Image Quality Equation (GIQE) is an empirical model that was developed in 1980s by IRARS Committee [15, 12]. NIIRS performance is predicted by using GIQE model by the functions of scale, expressed as GSD; sharpness, calculated with RER and spectral resolution, by Signal-to Noise Ratio [15]. Three validation cases of GIQE v.4. are indicated in Table 2.3.2. Linear regression method was used between calculated and observed GIQE datasets. Visible band calculations have differ from observations with 0.212 standard error for case1 and 0.307 for case 2 [12]. Also it is stated that the standard error of GIQE is ± 0.3 NIIRS for visible band [14, 29]. 0.986 and 0.934 R^2 values represent good consistency of the GIQE v.4 equation in visible band. On the other hand 0.80 R^2 and 0.38 standard error for IR band shows GIQE is not sensitive to IR band as it is to visible band. Considering the literature, the standard error of GIQE v.4 calculations are accepted as ± 0.3 NIIRS for visible band and ± 0.4 for IR band [12, 29, 30]. Version 4 of the GIQE equation is given with coefficients presented in [15]:

$$GIQE\ v.4 = c_0 + c_1 \log_{10}(GSD_{GM}) + c_2 \log_{10}(RER_{GM}) + c_3 \frac{G}{SNR} + c_4 H \quad Eq. 2.17$$

where GSD_{GM} : Ground Sampling Distance geometric mean, RER_{GM} : Relative Edge Response geometric mean, SNR : Signal to Noise Ratio, G : noise gain, H : overshoot ratio.

Table 2.3.1. GIQE v.4 coefficients for visible imagery.

Coefficient Set	c_0	c_1	c_2	c_3	c_4
$RER_{GM} < 0.9$	10.251	-3.16	2.817	-0.334	0.656
$RER_{GM} > 0.9$	10.251	-3.32	1.559	-0.334	0.656

Table 2.3.2. Validation cases of GIQE v.4. Equation [15, 12].

System Parameter	Case 1		Case 2		Case 3	
	min	max	min	max	min	max
Band	visible	visible	visible	visible	IR	IR
GSD (inch)	3	80	3	238	3	238
RER	0.2	1.3	0.2	1.3	0.2	1.3
H	0.90	1.90	0.90	1.39	0.9	1.39
G	1	19	1	19	1	19
SNR	2	130	2	130	2	130
R^2	0.986		0.934		0.800	
Standard error	0.282		0.307		0.380	

2.3.1 Ground Sampling Distance

GSD is defined as the projection of the distance between the center of two adjacent pixels on the object plane as illustrated in Figure 2.1.3.1. Spatial resolution and the details of the objects decrease as the GSD increases. GSD is depending on altitude, focal length and pixel size parameters. According to the definition in GIQE v.4. model IQA program calculates the GSD term as the mean of the along and across direction GSD values with the following equations [16, 30]:

$$GSD = \frac{h p}{f_{eff}} \quad Eq. 2.18$$

$$GSD_{GM} = \sqrt{GSD_{along} GSD_{across}} \quad Eq. 2.19$$

where GSD: Ground Sampling Distance, f_{eff} : effective focal length, h: altitude, p: pixel pitch size.

2.3.2 Sampling, Sampling Quality and Aliasing

EOIPL samples the scene as a digital number depending on the pixel size. Sampling limits the resolution by spatially averaging the radiance reflected inside the GSD area on the ground. The number of object details that end-user can distinguish decreases as the sampling interval increases. Each digital number on the image matrix represents the average radiance fall over a detector sampling pitch. Properties of the sampling can be clarified better by

assuming an object that has a wave pattern. To distinguish the characteristics of this sinusoidal object, there should be at least one pixel on the detector plane for each maximum and minimum radiance points on the object. Minimum sampling limit that ensures recognition of the scene details is defined as Nyquist sampling. The degradation of the wave pattern because of the insufficient number of pixels is defined as aliasing. To avoid aliasing the sampling frequency of the EO IPL must be less than the NSF. Sampling Spatial Frequency (SSF) equals to reciprocal of the pixel pitch size. NSF is defined as the half of the SSF which is expressed as [9]:

$$f_{sampling} = \frac{1}{p} \quad Eq. 2.20$$

$$f_{Nyquist} = \frac{f_{sampling}}{2} \quad Eq. 2.21$$

where $f_{sampling}$ is SSF limit, $f_{Nyquist}$ is NSF

On the other hand, spatial frequency limit of an EO IPL may be originated from the optical design limits. Maximum spatial frequency resolution of a circular aperture that can resolve two point objects is defined as Sparrow criterion [14]. The Diffraction Spatial Frequency (DSF) limit of the EO IPL is given as:

$$f_{optics} = \frac{D}{\lambda_{mean} f_{eff}} \quad Eq. 2.22$$

where D is M1 mirror diameter, λ_{mean} is mean wavelength of the band, f_{eff} is effective focal length.

Sampling Quality (Q) parameter is defined as the ratio of SSF limit to the DSF limit. During EO IPL design steps the value of Q is optimized to ensure the image quality performance characteristics that meets the end-user needs. As the diffraction limit increases the resolution of the image is limited by the optics. The optics blurring effects become dominant on the final product. On the other hand for a lower SSF limit than the DSF limit the end image becomes more

pixilated and aliased. In Figure 2.3.2.1 the cases that occur during Q parameter optimization is adduced. Sampling quality parameter is expressed as [14]:

$$Q = \frac{f_{sampling}}{f_{optics}} \tag{Eq. 2.23}$$



Figure 2.3.2.1. Balancing Q parameter in EOIPL design Characteristics of the image quality is depending on whether the spatial resolution is limited by optics or detector [14].

2.3.3 Modulation Transfer Function and Relative Edge Response

MTF represents the EOIPL modulation (contrast) transfer capability depending on the spatial frequency inputs ranging from zero to infinity. It is used to describe how the imaging chain degrades the modulation through the imaging chain. MTF is defined as the absolute value of the complex Fourier transform of the PSF. Typical MTF decreases gradually depending on spatial frequency increment. At system spatial frequency limit MTF is equal to 0 while MTF is 1 at zero spatial frequency. MTF is evaluated as the mean of the along and across scan direction RER parameters in IQA program by considering GIQE v.4 model [12]. The system MTF is calculated over normalized spatial frequency ranging from zero to system cut off spatial frequency [14]. Nyquist Spatial Frequency (NSF) is defined as the half of the sampling spatial frequency. MTF value of the total system is indicated as the value of the MTF at NSF. Total system MTF at NSF is defined as the products of the subcomponent MTF values at NSF. The MTF breakdown of the payload and satellite level MTF calculations included in IQA are presented in Figure 2.3.3.1. Payload level MTF is the product of optics MTF and detector MTF. Satellite level MTF is calculated by degraded payload MTF by atmosphere turbulence and platform stability errors.

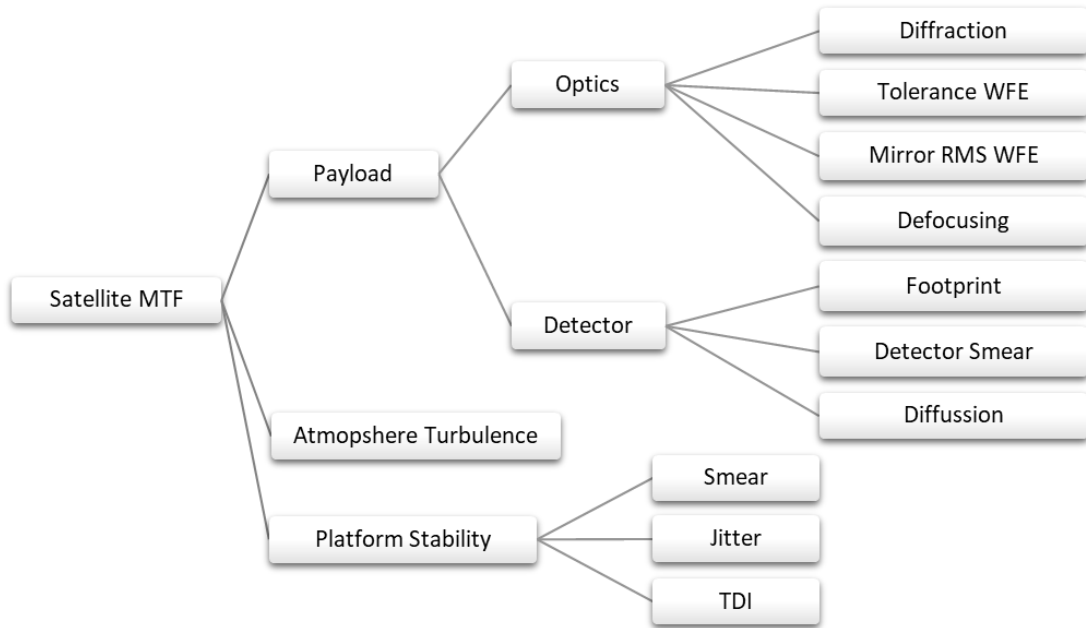


Figure 2.3.3.1. Satellite level MTF breakdown of IQA program includes payload, atmosphere turbulence and platform stability degradations.

Optics system MTF of IQA program consists of diffraction, tolerance WFE (Wave Front Error), mirror rms WFE and defocusing breakdowns as represented in Figure 2.3.3.1.

$$MTF_{optics} = MTF_{diffraction} MTF_{tolerance} MTF_{rms_{mirror}} MTF_{defocus} \quad Eq. 2.24$$

In a perfect EOIPL system image radiance distribution is equal to the object radiance distribution with delta function PSF. Due to the nature of the light, the width of the PSF widens and the image quality degrades. According to Huygens's principle during the propagation of a wavefront each points on that wavefront acts like a source of spherical waves. By adding these spherical waves propagating waveform is acquired. When the wavefront passes through the aperture of an EOIPL its form becomes deformed by the edges of the aperture by diffraction. Aperture geometry of the EOIPL is defined as the aperture function that has a value of 0 for the spatial locations that reflects and diffracts light, one for the locations where there is no disturbance on the wavefront geometry. Incoming electric field strength after passing the aperture is given by [14]:

$$E(x, y) = \frac{e^{-iw(t-t_0)}}{i\lambda} \int_{-\infty}^{\infty} \int_{-\infty}^{\infty} E_0(x_0, y_0) A(x_0, y_0) \frac{e^{ikR}}{|R|} dx_0 dy_0 \quad \text{Eq. 2.25}$$

where R is the propagation distance, $A(x_0, y_0)$ is the aperture function, $E_0(x_0, y_0)$ is the incoming electric field, w is the harmonic field frequency, λ is the wavelength.

For the diffraction along a pinhole of an incident plane wave, aperture function is delta function and $E_0(x_0, y_0)$ is constant. The diffracted light has a spherical wave in this case. When the distance between the object plane and the aperture is comparable with the size of the aperture, Fresnel diffraction pattern is observed. It is also called near-field diffraction. The light passing through the aperture is approximated as waves with parabolic shape. For the distances that far away, the diffraction pattern is defined by Fraunhofer diffraction or far field diffraction. For the far field diffraction case where R is greater than wavelength the Fraunhofer diffraction of the light field is equal to the Fourier transform of the aperture geometry function at $x_0 = x/\lambda R$ and $y_0 = y/\lambda R$. For the imaging chain applications because of the fact that altitude is far more than the wavelength order of the spectral band, Fraunhofer diffraction approximation is used to simulate the light passing through the edges of the aperture geometry. Intensity of the light is the square of the electric field by definition.

$$I(x, y) = |E(x, y)|^2 = \frac{E_0^2}{(\lambda R)^2} |A(x_0, y_0)|^2 \quad \text{Eq. 2.26}$$

where R is the propagation distance, $A(x_0, y_0)$ is the aperture function, $E_0(x_0, y_0)$ is the incoming electric field, λ is the wavelength.

The diffraction PSF is depending on aperture function:

$$PSF_{diffraction}(x, y) \propto |A(x_0, y_0)|^2 \quad \text{Eq. 2.27}$$

For the circularly symmetrical central obscured aperture geometry the PSF is defined as:

$$PSF_{diffraction}(x) = \left(\frac{E_0 \pi D^2}{4 \lambda f_{eff}} \right)^2 \left[\text{somb} \left(\frac{Dx}{\lambda f_{eff}} \right) - \left(\frac{D_{obs}}{D} \right)^2 \text{somb} \left(\frac{D_{obs} x}{\lambda f_{eff}} \right) \right]^2 \quad Eq. 2.28$$

$$\text{somb}(t) = \frac{2 J_1(\pi t)}{\pi t} \quad Eq. 2.29$$

where D is the M1 mirror diameter, E_0 is incoming electric field, λ is wavelength, f_{eff} is effective focal length, D_{obs} is obscuration diameter, x is spatial position, $\text{somb}(t)$ is sombero function, J_1 is Bessel function of the first kind.

MTF is defined as the absolute value of the Fourier transform of the PSF function.

$$MTF_{diffraction}(f) = [FT \{PSF_{diffraction}(x)\}] \quad Eq. 2.30$$

Diffraction MTF for circularly symmetrical obscured aperture is calculated over normalized spatial frequency on DSF by using following equation [31]:

$$MTF_{diffraction}(f) = \left\{ \frac{2}{\pi} \left[\frac{A+B+C}{1-e^2} \right] \right\} \quad Eq. 2.31$$

$$A(f) = \cos^{-1}(f) - f\sqrt{1-f^2} \quad ; 0 \leq f \leq 1 \quad Eq. 2.32$$

$$B(f) = \begin{cases} e^2 \left(\cos^{-1} \frac{f}{e} - \frac{f}{e} \sqrt{1 - \frac{f^2}{e^2}} \right) & ; 0 \leq f \leq e \\ 0 & ; f > e \end{cases} \quad Eq. 2.33$$

$$C(f) = \begin{cases} -\pi e^2 & ; 0 \leq f \leq \frac{1-e}{2} \\ -\pi e^2 + e \sin(\phi) + \frac{\phi}{2} (1+e^2) - (1-e^2) \tan^{-1} \left(\frac{1+e}{1-e} \tan \frac{\phi}{2} \right) & ; \frac{1-e}{2} \leq f \leq \frac{1+e}{2} \\ 0 & ; f > \frac{1+e}{2} \end{cases} \quad Eq. 2.34$$

$$\phi(f) = \cos^{-1} \frac{1 + e^2 - 4f^2}{2e} \quad \text{Eq. 2.35}$$

$$e = \frac{D_{obs}}{D} \quad \text{Eq. 2.36}$$

where A, B, C and ϕ are obscured diffraction MTF constants, e is obscuration ratio, D is the M1 mirror diameter, D_{obs} is obscuration diameter, f is normalized spatial frequency.

Wavefront errors are modeled as the degradations in the ideal spherical wave functions and defined by wavefront deviations (denoted as $W(x,y)$). Pupil function is defined as the combination of the wavefront deviation function and aperture function.

$$P(x, y) = A(x, y)e^{ikW(x,y)} \quad \text{Eq. 2.37}$$

where $P(x, y)$ is pupil function, $A(x, y)$ is aperture function, $W(x, y)$ is wavefront deviation function.

According to the Rayleigh's Rule on quarter wavelength for the cases with $W(x,y)$ is smaller than the quarter of the wavelength, image quality is not affected by wavefront errors. In general, the wavefront errors change the PSF over the image plane. This is violating the LSI rule of the imaging chain simulations. IQA program simulates the image quality parameters and the image simulations of an EOIPL which is in the preliminary design steps. WFE degradations are represented by using statistical models in IQA program. Root mean square of the statistically derived wavefront deviation function is used for the estimation of the image quality degradations of wavefronts in this step. Tolerance WFE and mirror rms WFE MTF's are calculated by using Hufnagel statistical model for aberration MTF. The cut off input spatial frequency of WFE MTF calculations are defined with diffraction limit. IQA program simulates the WFE degradation with following equation [14]:

$$MTF_{WFE}(f) = \exp\left((2\pi WFE)^2(1 - \exp\left(-4\left(\frac{f}{l}\right)^2\right))\right) \quad Eq. 2.38$$

where WFE is the root mean square of the wavefront deviations, l is the correlation length of the roughness of the surface.

Also the defocusing degradation MTF are calculated over normalized spatial frequency on diffraction cut off spatial frequency by using Shannon's approximation in IQA program [14]:

$$MTF_{defocus}(f) = \frac{2J_1[8\pi W_{pp}f(1-f)]}{8\pi W_{pp}f(1-f)} \quad Eq. 2.39$$

where W_{pp} is peak to peak wavefront error, J_1 is Bessel function of the first kind.

Detector MTF in IQA program is calculated by degrading the footprint MTF with detector smear and diffusion as given in Figure 2.3.3.1.

$$MTF_{detector} = MTF_{footprint} MTF_{diffusion} MTF_{smear} \quad Eq. 2.40$$

Each pixel on the detector array is spatially averaging the radiance falling on pixel pitch size. For the detector types with square pixel shape, the foot print PSF is defined as:

$$PSF_{footprint}(x) = \text{rect}\left(\frac{x}{p}\right) \quad Eq. 2.41$$

where p is pixel pitch size, $\text{rect}(x)$ is rectangular function.

Footprint MTF is calculated over the normalized spatial frequency on SSF by using following equation [14]:

$$MTF_{footprint}(f) = sinc(pf) \quad Eq. 2.42$$

where p is pixel pitch size.

Photo-electrons generated inside the substrate of the detector well are randomly diffusing until they find themselves in different well they were generated. Random directional diffusion of photo-electrons cause degradation of the image quality. Sieb's model for diffusion MTF is calculated over normalized spatial frequency on sampling cut off spatial frequency by using following equation [14]:

$$MTF_{diffusion}(f) = \frac{1 - \frac{\exp(-\alpha_{abs}(\lambda)L_D)}{1 + \alpha_{abs}(\lambda)L(f)}}{1 - \frac{\exp(-\alpha_{abs}(\lambda)L_D)}{1 + \alpha_{abs}(\lambda)L_{diff}}} \quad Eq. 2.43$$

$$L(f) = \frac{L_{diff}}{\sqrt{1 + (2\pi L_{diff}f)^2}} \quad Eq. 2.44$$

where α_{abs} is the absorption coefficient of the detector material, L_D is the depletion width and L_{diff} is the diffusion length.

Exposure time of one pixel is defined as the integration time. Serial readout difference of pixels causes degradation for each pixel in the imaging chain. This degradation is defined as detector smear MTF and it is calculated over normalized spatial frequency on sampling cut off spatial frequency by using following equation [14]:

$$MTF_{smear}(f) = sinc(d_{smear}f) \quad Eq. 2.45$$

where d_{smear} is defined as the detector smear error.

The random fluctuations in the refractive index through light path cause deviations in the wavefront direction. Among such a distance of an altitude in the order of kilometers, these random fluctuations are calculated over a rectangular PSF with atmosphere smear degradation factor in IQA program. Atmosphere degradations on the MTF are calculated by using spatial frequency normalized on sampling cut off spatial frequency. Atmosphere degradation MTF included in IQA is given as the following relation [20]:

$$MTF_{atmosphere}(f) = sinc(d_{atm}f) \quad Eq. 2.46$$

where d_{atm} is the atmosphere smear error.

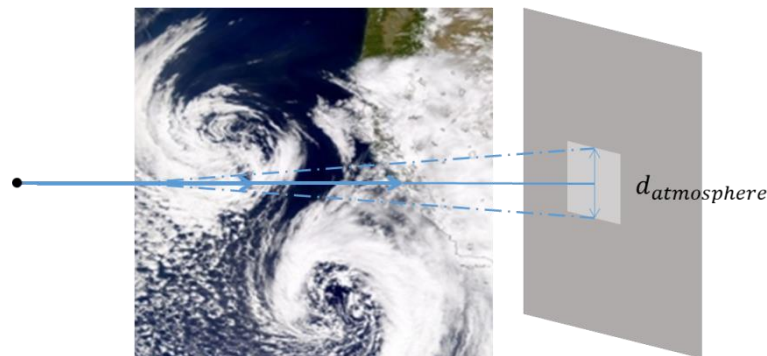


Figure 2.3.3.2 Atmosphere degradations due to random refractive index fluctuations in IQA program are simulated by spatially averaging the radiance data on each pixel.

Platform stability degradations are evaluated by taking into account of smear, jitter and TDI (Time Delay Integration) MTF degradations as expressed in Figure 2.3.3.1. Satellite smear is originated because of the spatial averaging of light over the area on the detector plane that scanned with linear velocity error among integration time. Satellite smear PSF is defined as the rectangular function. Satellite smear degradation is calculated over normalized spatial frequency on sampling cut off spatial frequency by using following equation [14]:

$$MTF_{smear}(f) = \text{sinc}(d_{blur}f) \quad \text{Eq. 2.47}$$

$$d_{blur} = v_{img}T_{int} \quad \text{Eq. 2.48}$$

where d_{blur} is the platform stability smear error, V_{img} is the velocity mismatch along boresight, T_{int} is the integration time for each pixel

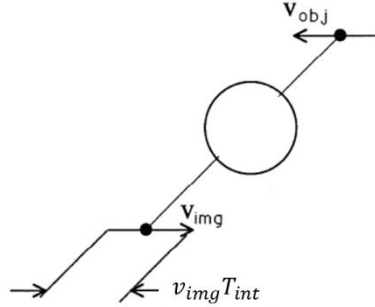


Figure 2.3.3.3 Linear motion error is defined as the spatial averaging of the distance which is determined by the product of the velocity mismatch along the boresight and the integration time in IQA program.

Platform jitter motion is defined as the random motion in each direction of the satellite with high frequency. Gaussian distribution function is used for the definition of the platform jitter motion PSF.

$$PSF_{jitter}(f) = \frac{1}{\sigma_{jitter}\sqrt{2\pi}} e^{-\frac{f^2}{2\sigma_{jitter}^2}} \quad \text{Eq. 2.49}$$

where σ_{jitter} is the jitter motion standard deviation.

By taking the absolute value of the PSF, jitter MTF degradation included in IQA program is calculated over normalized spatial frequency on sampling cut off spatial frequency by using following equation [14]:

$$MTF_{jitter}(f) = \exp(-2(\pi\sigma_{jitter}f)^2) \quad Eq. 2.50$$

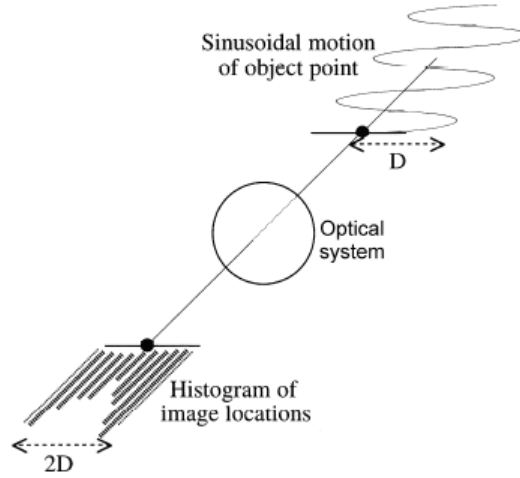


Figure 2.3.3.4. Effects of the random motion errors on image quality is defined by the Gaussian distribution function in IQA program [20].

Due to the clocking rate mismatches, packet of charges are not always synchronized with the velocity of the image plane in TDI imaging. This mismatch brings out blurring in the image. TDI MTF degradation in IQA program is calculated over normalized spatial frequency on sampling cut off spatial frequency by using following equation [14]:

$$V_{charge} = \frac{p}{T_{int}} \quad Eq. 2.51$$

$$d_{error} = \text{abs}(V_{object} - V_{charge}) \quad Eq. 2.52$$

where p is the pixel pitch size, T_{int} is the integration time of a pixel pitch, V_{charge} is the velocity of a charge packet, V_{object} is object velocity, d_{error} is the boresight stability error.

$$MTF_{TDI}(f) = \frac{\sin(\pi TDI d_{error}f)}{TDI \sin(\pi TDI d_{error}f)} \quad Eq. 2.53$$

where TDI is the number of TDI steps.

$$MTF_{platform} = MTF_{smear} MTF_{jitter} MTF_{TDI} \quad \text{Eq. 2.54}$$

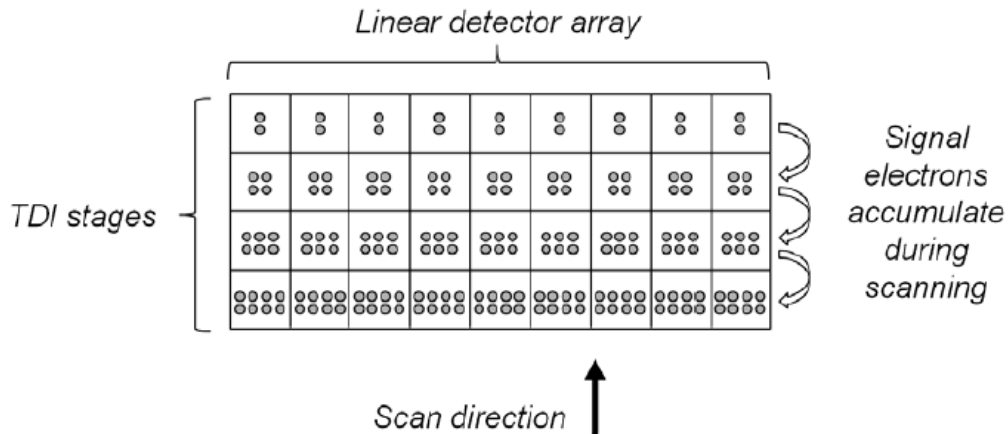


Figure 2.3.3.5. TDI degradation arises because of the clocking rate mismatches in the FPA [21].

Sharpness transfer degradations of the object radiance matrix due to the links in the imaging chain are represented by RER (Relative Edge Response). The edge response of a step function object is defined as Edge Response Function (ERF). RER is the difference between the half pixel shifted ESF values from the sharp edge transition. To evaluate relationship between MTF and RER value, convolution and the Fourier Transform of the imaging equation are calculated. Measurement of the RER and MTF values are held by using knife edge targets according to the ISO 12233 standard [28]. A knife edge target calibration site at McMahon-Wrinkle Airport in Texas is given in Figure 2.3.3.6.



Figure 2.3.3.6. Knife edge targets are used for MTF and RER measurement from space [32].

Derivation of the RER function for a EOIPL system is given with following steps. The diffraction limited resolution of the EOIPL is represented with the DSF limit in the Fourier domain. Spatial position is defined as one divided by spatial frequency. Imaging equation can also be expressed in the terms of the dimensionless ratio of laterally changing distance in the imaging plane and the spatial position diffraction cut off limit [14].

$$i(v) = o(v) * PSF(v) \quad Eq. 2.55$$

$$x_{optics} = \frac{\lambda f_{eff}}{D} \quad Eq. 2.56$$

$$v = \pi \frac{z}{x_{optics}} \quad Eq. 2.57$$

where x_{optics} is the spatial position diffraction cut off limit, v is dimensionless ratio of laterally changing distance in the imaging plane and the spatial position diffraction cut off limit, $i(v)$ is the image radiance distribution, $o(v)$ is the object radiance distribution.

The step function object input can be visualized as a sharp edge transition. The Edge Response Function (ERF) is defined as the image output of the EOIPL with step function object input [33]:

$$ERF(v) = i(v) \quad Eq. 2.58$$

$$o(v) = \begin{cases} 0 & v < 0 \\ 1 & v > 0 \end{cases} \quad \text{Eq. 2.59}$$

where $ESF(v)$ is the edge spread function, $o(v)$ is the object radiance distribution.

MTF is defined as the absolute value of the Fourier Transform of the PSF. By using the convolution of Fourier transform identity image radiance spectrum can be calculated as the product of the MTF and object radiance spectrum (Fourier transform of the step function in this case). By taking the inverse Fourier transform of the image radiance spectrum, one can calculate ESF function as following:

$$I(w) = O(w)MTF(w) \quad \text{Eq. 2.60}$$

$$\frac{w}{2} = \frac{f}{f_{optics}} \quad f = \frac{w}{\frac{2\lambda f_{eff}}{D}} \quad \text{Eq. 2.61}$$

$$f = \frac{w}{\frac{2\lambda f_{eff}}{D}}$$

where w is the double amount of the normalized spatial frequency of the EOIPL, f is the spatial frequency, $I(w)$ is image radiance spectrum, $O(w)$ is object radiance spectrum, f_{eff} is the effective focal length, D is the M1 mirror diameter.

The ESF is also can be expressed as the inverse Fourier transform of the image spectrum of the step function object input degraded by MTF function [33]:

$$ESF(v) = i(v) = IFT(I(w)) = IFT(O(w)MTF(w)) \quad \text{Eq. 2.62}$$

The object function spectrum is given as the Fourier transform of the step function input:

$$FT(O(v)) = O(w) = \pi\delta(w) + \frac{1}{iw} \quad \text{Eq. 2.63}$$

ESF is calculated by taking the inverse Fourier transform of the MTF and object spectrum product [33].

$$ESF(v) = \int_{-\infty}^{\infty} \left\{ O(w) = \pi\delta(w) + \frac{1}{iw} \right\} MTF(w) e^{i w v} dw \quad \text{Eq. 2.64}$$

$$\pi + \frac{1}{i} \int_{-\infty}^{\infty} \frac{MTF(w)}{w} e^{i w v} dw$$

There are two constraints of the ESF derivation. MTF is 0 outside the normalized spatial frequency cut off and 1 for zero normalized spatial frequency. ESF is 1 at infinity normalized distance. By using Dirichlet Integral identity and Euler formula, ESF function is calculated as:

$$ESF(v) = \pi + \frac{1}{i} \int_{-\infty}^{\infty} \frac{MTF(w)}{w} \cos(wx) dw + \int_{-\infty}^{\infty} \frac{MTF(w)}{w} \sin(wx) dw \quad \text{Eq. 2.65}$$

$$\lim_{x \rightarrow \infty} \int_{-\infty}^{\infty} \frac{\sin(vx)}{c} dx = \pi f(0) \quad \text{Eq. 2.66}$$

Second term of the equation is eliminated because of the fact that integral of an odd function equals to zero. $\frac{1}{2\pi}$ normalization factor comes from the constraints.

$$ESF(v) = \pi + \int_{-\infty}^{\infty} \frac{MTF(w)}{w} \sin(wv) dw \quad \text{Eq. 2.67}$$

$$\lim_{v \rightarrow \infty} ESF(v) = 1, \quad \text{Eq. 2.68}$$

$$ESF(v) = \frac{1}{2} + \frac{1}{2\pi} \int_{-2}^2 \frac{MTF(w)}{w} \sin(wv) dw \quad \text{Eq. 2.69}$$

By substituting the distance normalized on diffraction resolution and normalized spatial frequency values to the equation, ESF depending on lateral distance can be derived.

$$wv = 2 \frac{f}{f_{optics}} \pi f_{optics} z = 2\pi f z \quad Eq. 2.70$$

$$ESF(z) = \frac{1}{2} + \int_0^{f_{cutoff}} \frac{MTF(f)}{\pi 2 \frac{f}{f_{optics}}} \sin(2\pi f z) d\left(2 \frac{f}{f_{optics}}\right) \quad Eq. 2.71$$

$$ESF(z) = \frac{1}{2} + \int_0^{f_{cutoff}} \frac{MTF(f)}{\pi f} \sin(2\pi f z) df \quad Eq. 2.72$$

Lateral distance z is converted to pixel displacement to find ESF depending on pixel position. Edge Response Equation (ERQ) depending on pixel displacement is calculated as in following equation [14]:

$$z = p * d \quad Eq. 2.73$$

$$ESF(d) = \frac{1}{2} + \int_0^{f_{cutoff}} \frac{MTF(f)}{\pi f} \sin(2\pi f p d) df \quad Eq. 2.74$$

where d is pixel displacement, p is pixel pitch size and z is the laterally changing distance on the detector plane.

Leachtenauer defines f_{cutoff} as the optics cut off normalized to the effective sample spacing [12]. ESF is calculated over normalized spatial frequency on sampling cut off spatial frequency $\gamma = \frac{f}{f_{det}}$. For $Q > 1$ EOIL system f_{cutoff} is equal to f_{optics} .

$$ESF(d) = \frac{1}{2} + \int_0^{f_{cutoff}} \frac{MTF(\gamma)}{\pi \gamma f_{det}} \sin(2\pi f p d) d(f_{det} \gamma) \quad Eq. 2.75$$

$$ESF(d) = \frac{1}{2} + \int_0^{1/Q} \frac{MTF(\gamma)}{\pi \gamma} \sin(2\pi d \gamma) d\gamma \quad Eq. 2.76$$

$$\gamma = \frac{f}{f_{optics}} \quad Eq. 2.77$$

where γ is the normalized spatial frequency on DSF limit.

RER parameter is calculated by using following equations in IQA program [8, 34-37]:

$$RER = ESF(0.5) - ESF(-0.5) \quad Eq. 2.78$$

$$RER = 2 \int_0^{1/Q} \frac{MTF(\gamma)}{\pi\gamma} \sin(\pi\gamma) d\gamma \quad Eq. 2.79$$

It is important to note that, even for the system design solutions including the same MTF value at NSF the area under the MTF graph could differ for different links in the imaging chain. It should be considered that considering the RER parameter for evaluating the contrast transfer quality of the EOIPL provides more reliable information than considering the MTF value at NSF.

2.3.4 Signal to Noise Ratio (SNR) Calculation

SNR is used in evaluation of the radiometric resolution of the EOIPL systems in IQA program. For the case where the noise fluctuations are more than the signal levels coming from the scene, the objects in the image become indistinguishable. SNR is defined as the ratio between signal level electrons to the background noise level electrons [14]:

$$SNR = \frac{Signal}{Noise} \quad Eq. 2.80$$

IQA program simulates the image quality of an EOIPL which is operating in a satellite system imaging in visible band. SNR is depending on the imaging geometry, atmosphere conditions, total spectral transmission data of the EOIPL

and integration time parameters. Integration time of a satellite EOIPL in orbit is defined as the required time for collecting light reflected from the GSD area. It is calculated depending on the satellite ground velocity and the GSD. The orbit scheme of a satellite is demonstrated in Figure 2.3.4.1.

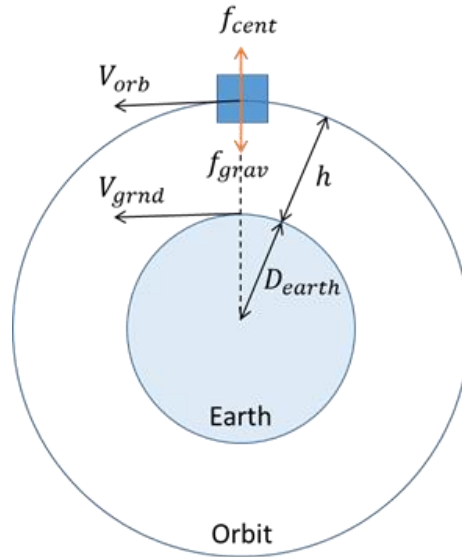


Figure 2.3.4.1. Orbit scheme of a satellite.

From the equality of the centripetal and gravitational forces, orbital velocity of the satellite can be derived by following equations.

$$\frac{m_{sat} V_{orb}^2}{D_{earth} + h} = \frac{G_{grav} (m_{sat} m_{earth})}{(D_{earth} + h)^2} \quad Eq. 2.81$$

$$V_{orb} = \sqrt{\frac{g * m_{earth}}{D_{earth} + h}} \quad Eq. 2.82$$

where m_{sat} is satellite mass, m_{earth} is earth mass, D_{earth} is earth radius, V_{orb} is orbital velocity of the satellite, h is altitude, g is gravitational constant.

By using the similarity identity between orbital and ground velocities from Figure 2.3.4.1 the ground velocity of the satellite can be derived. Integration time is the ratio between GSD and ground velocity of the satellite.

$$\frac{V_{orb}}{V_{grnd}} = \frac{D_{earth} + h}{D_{earth}} \quad Eq. 2.83$$

$$V_{grnd} = \frac{D_{earth} V_{orb}}{D_{earth} + h} \quad Eq. 2.84$$

$$T_{int} = \frac{GSD}{V_{grnd}} \quad Eq. 2.85$$

where V_{grnd} is the ground velocity of satellite.

SNR is calculated by the ratio of predicted number of signal electron to number of noise electron. Signal electron is generated by weighting the input irradiance spectrum derived from MODTRAN (Moderate Resolution Atmospheric Transmission) by imaging chain design parameters. Integration time, number of TDI step, altitude, GSD, diameter of M1 mirror, diameter of obscuration and spectral response of the EOIPL are the factors that are considering during signal calculation. Radiant flux reaching the entrance aperture of the camera is calculated by integrating the spectral radiance, aperture and solid angle product [38].

$$\phi_{aperture} = \int_{\lambda_{min}}^{\lambda_{max}} L(\lambda) \frac{GSD^2}{h^2} \left(\frac{\pi}{4} D^2 (1 - e) \right) d\lambda \quad Eq. 2.86$$

where $L(\lambda)$ spectral radiance, h is altitude, D is M1 mirror diameter, e is the obscuration ratio, λ is wavelength.

Radiance flux reaching the imaging plane inside the camera is calculated by addition of telescope transmission spectrum as a weight factor to the integral [39].

$$\phi_{image} = \int_{\lambda_{min}}^{\lambda_{max}} L(\lambda) \frac{GSD^2}{h^2} \left(\frac{\pi}{4} D^2 (1 - e) \right) TT(\lambda) d\lambda \quad Eq. 2.87$$

where $TT(\lambda)$ is the total spectral transmission.

Radiance flux reaching the detector during integration time within number of TDI steps is calculated by using following equation [14].

$$\phi_{detector} = \int_{\lambda_{min}}^{\lambda_{max}} L(\lambda) \frac{GSD^2}{h^2} \left(\frac{\pi}{4} D^2 (1 - e) \right) TT(\lambda) TDI T_{int} f_{factor} d\lambda \quad Eq. 2.88$$

where TDI is the number of TDI steps, T_{int} is integration time of a pixel, f_{factor} is the fill factor of the detector array.

Number of photons reaching the detector plane is calculated by dividing radiance flux reaching the detector plane to photon energy. [16]

$$n_{photon} = \int_{\lambda_{min}}^{\lambda_{max}} T_{int} TDI \frac{\frac{GSD^2}{h^2} L(\lambda) \left(\frac{\pi}{4} D^2 (1 - e) TT(\lambda) f_{factor} \right)}{\frac{h_p c}{\lambda}} d\lambda \quad Eq. 2.89$$

Number of signal electrons generated at the detector from the scene is calculated by adding the filter spectral transmission and spectral quantum efficiency to the integral [14].

$$Signal = \int_{\lambda_{min}}^{\lambda_{max}} T_{int} TDI \frac{\frac{GSD^2}{h^2} L(\lambda) \left(\frac{\pi}{4} D^2 (1 - e) T(\lambda) f_{factor} \right)}{\frac{h_p c}{\lambda}} d\lambda \quad Eq. 2.90$$

$$TT(\lambda) = QE(\lambda) * FT(\lambda) * TT(\lambda) \quad Eq. 2.91$$

The electrons generated due to the photon collection at detector pixel surface are digitized as voltage at ADC (Analog to Digital Converter). Quantum step equivalence used in scaling the signal electron count to digital counts [16].

$$QSE = G_c \frac{FWC}{DR} \quad Eq. 2.92$$

$$DR = 2^N - 1 \quad Eq. 2.93$$

$$counts = int\left(\frac{Signal}{QSE}\right) \quad Eq. 2.94$$

where QSE is quantum step equivalence, G_c is the conversion gain, N is level of quantization, FWC is full well capacity, DR is the dynamic range.

Total noise variance is calculated as the summation of the variance of each noise subcomponents because of the fact that random noise contributors are independent. Photon noise, read noise and quantization noise are calculated as the noise subcomponents of the EOIP. Photon noise is observed because of the random arrival time of the photons on the detector surface within integration time. Photon noise is simulated as Poisson distribution and the photon noise variance is equal to the number of signal electrons. Another noise contribution is read noise. Detector voltage variances give rise to read noise. Quantization of signal into digital counts brings uncertainty to the actual signal electron count level as quantization noise [14].

$$Noise = \sqrt{Signal + RN^2 + QN^2} \quad Eq. 2.95$$

$$QN = \frac{QSE}{\sqrt{12}} \quad Eq. 2.96$$

where QN is the quantization noise, QSE is quantum step equivalence.

SNR at constant albedo is defined as the ratio of the target signal to standard deviation of the noise at constant albedo [40].

$$SNR_r = \frac{Signal_r}{Noise_r} \quad Eq. 2.97$$

In GIQE v.4. SNR is defined as the ratio of the DC differential scene signal level to rms electrons of noise. DC differential scene is defined as the difference in the detector output between two Lambertian surface with different albedo values. QIQE v.4. assumes that these two Lambertian target have 7% and 15% albedo. SNR calculation included in IQA program is given with following equation [12, 38, 40]:

$$SNR_{GIQE} = \frac{Signal_{r=0.15} - Signal_{r=0.07}}{Noise_{r=0.15}} \quad Eq. 2.98$$

2.4 Image Simulation Module

Image simulations are necessary to demonstrate the relation between the physical degradation links in the imaging chain and to acquire better understanding of how image quality parameters effect the final image [41, 42]. Specifying the EO IPL system tradeoffs during the design steps is one of the important applications of image simulation utilization. Especially for determining the requirement sets for image quality performance metrics of specific applications image simulations are used. Also image simulations are employable during mission planning activities. Same EO IPL system even differs in performance for different dates of the year, atmospheric conditions and SZA (Sun Zenith Angle) values because of the fact that imaging geometry includes two-path light propagation. Mission tasks can be simulated by using image simulations to have better estimation of acceptable acquisition dates and conditions [38].

IQA program image simulation module applies imaging chain model to a sample image with higher spatial frequency than simulated EO IPL system. Polychromatic MTF application, GSD resampling and noise addition are the main steps of the function. Image simulation module algorithm included in IQA program is given in Figure 2.3.41. Conversion of DN values of image data to real physical parameters is necessary to observe the image quality degradation on the sample image. Radiance value of each pixel on the sample image data was calculated by first estimating the albedo levels of each pixel than by

applying MODTRAN generated radiance data to the simulated albedo values. After generating radiance dependent sample image polychromatic MTF is applied to the radiance data. Degraded polychromatic radiance data is converted to photo-electron count for each pixel by taking weighted sum of polychromatic radiance data with total spectral transmission data. Number of noise electron is applied to the image by using uniform distribution function. Finally resampling based on GSD calculations and quantization conversion to radiance dataset are applied to obtain digital counts of the simulated image [10, 16, 38, 43].

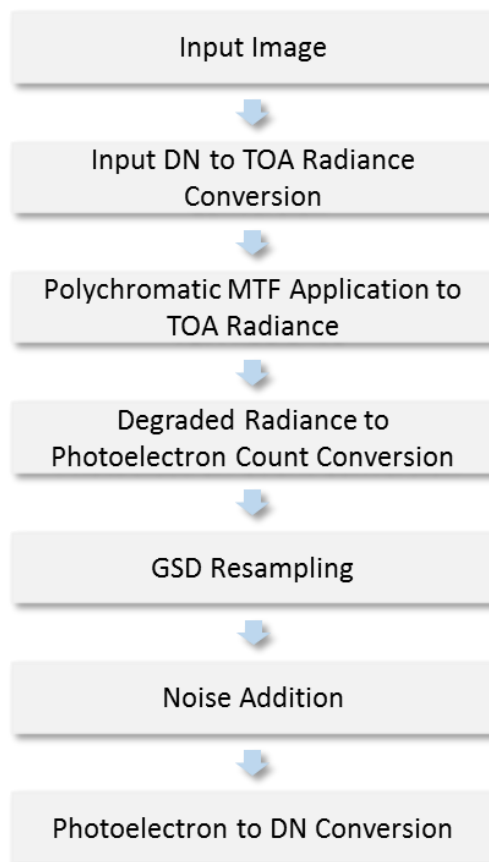


Figure 2.3.41. Flow chart of the image simulation process depending on GIQE model simulated by IQA program.

2.4.1 Digital Number to Band Average Albedo Conversion

Input sample image consists of 2D DN matrix. To evaluate the effects of imaging chain on the sample image, DN values of each pixel should be converted to data which represents real physical quantities. The term albedo

which means white originally in Latin language is defined as the amount of the sun light which is reflected from an object. Surface spectral albedo is defined by [44]:

$$\rho_{\lambda} = \frac{\int_{\lambda_1}^{\lambda_2} E_{u\lambda} d\lambda}{\int_{\lambda_1}^{\lambda_2} E_{g\lambda} d\lambda} = \frac{\int_{\lambda_1}^{\lambda_2} \rho_{\lambda} E_{g\lambda} d\lambda}{\int_{\lambda_1}^{\lambda_2} E_{g\lambda} d\lambda} \tag{Eq. 2.99}$$

where $E_{u\lambda}$ is upwelling spectral irradiance emitted from the surface, $E_{g\lambda}$ is the downwelling spectral irradiance on the surface.

ECOSTRESS version 1.0 Spectral Library which was released in 2018 by NASA Jet Propulsion Laboratory (JPL) , is a spectral surface albedo library of man-made and natural materials. For calculating the albedo values of each pixel position albedo data of “Construction Tar (0100UUUTAR)” and “Asphaltic Concrete (0425UUUASP)” materials are selected from ECOSTRESS spectral library provided by NASA JPL. Asphaltic concrete is defined as variegated asphaltic concrete with mostly limestone and some quartz aggregate with rough and black in color. On the other hand, construction tar is defined as black and glossy. The albedo values of two materials are shown in Figure 2.4.1.1.

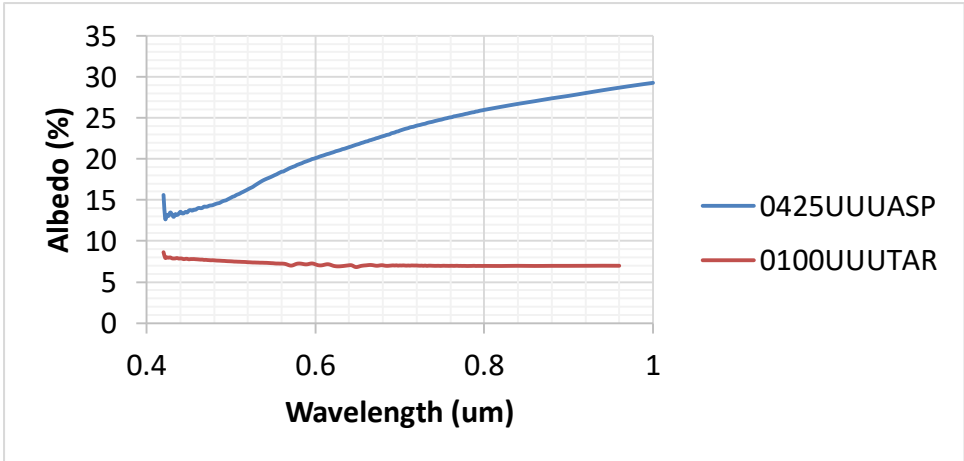


Figure 2.4.1.1. Spectral surface albedo data of 0425UUUASP and 0100UUUTAR downloaded from ECOSTRESS spectral library [16].

From the input sample image, the pixel areas containing 0100UUUTAR and 0425UUUASP materials are selected to find the ratio between the surface albedo and DN value of simulated spectral band at mean wavelength. To convert the DN to the albedo, two dimensional DN matrix is multiplied with mean albedo conversion ratio. PAN (Panchromatic) band mean albedo data matrix is calculated as adding the red, green and blue band mean albedo data matrixes with the same weight [16]. Global albedo measurement reflected from earth surface taken by MODIS (Moderate Resolution Imaging Spectrometer) of NASA is given in Figure 2.4.1.2.

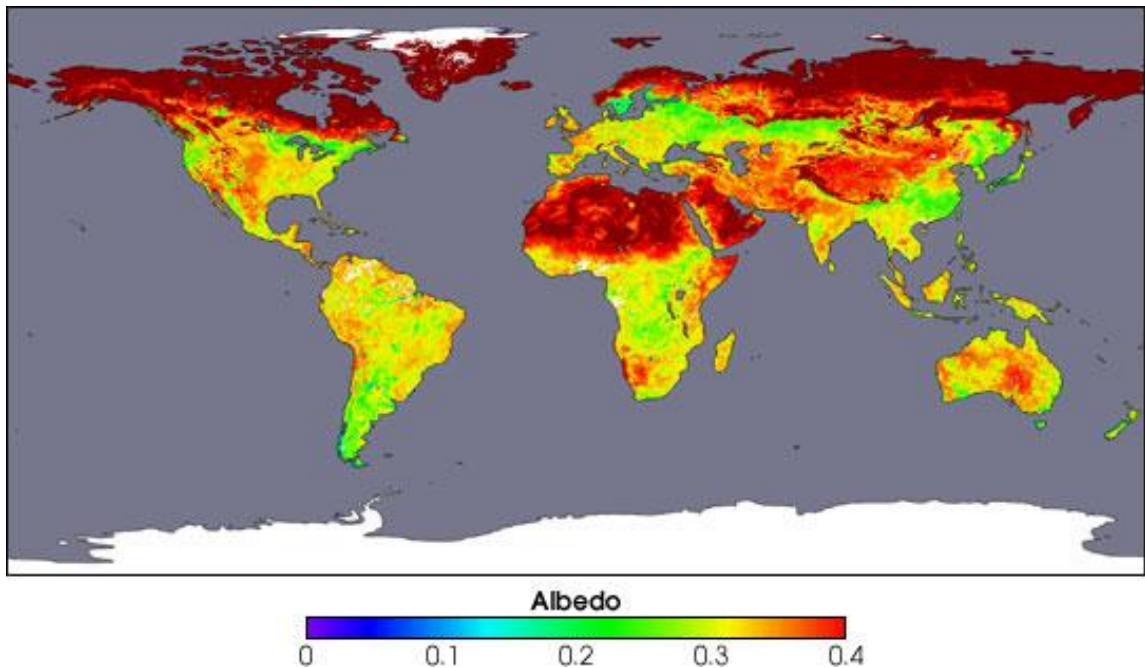


Figure 2.4.1.2. Global albedo measurement taken by MODIS [45].

2.4.2 Band Average Surface Albedo to TOA Radiance Conversion

Band average surface albedo is converted to TOA radiance for introducing the input sample image spectral characteristic. Spectral radiance viewing a Lambertian target at detector pixel is expressed as [16, 46-48]:

$$L(\lambda) = \frac{A(\lambda)\rho_\lambda}{1 - \rho_e S(\lambda)} + \frac{B(\lambda)\rho_e}{1 - \rho_e S(\lambda)} + L_{bs}(\lambda) \quad \text{Eq. 2.100}$$

where ρ_e is average albedo of the background region, $S(\lambda)$ is the spherical albedo coefficient of the atmosphere, $L_{bs}(\lambda)$ is the back-scattered radiance coefficient from the atmosphere, $A(\lambda)$ is the coefficient of downwelling solar radiation that reaches TOA after reflected from the object, $B(\lambda)$ is the coefficient of downwelling solar radiation that finds its way to TOA after reflected from background.

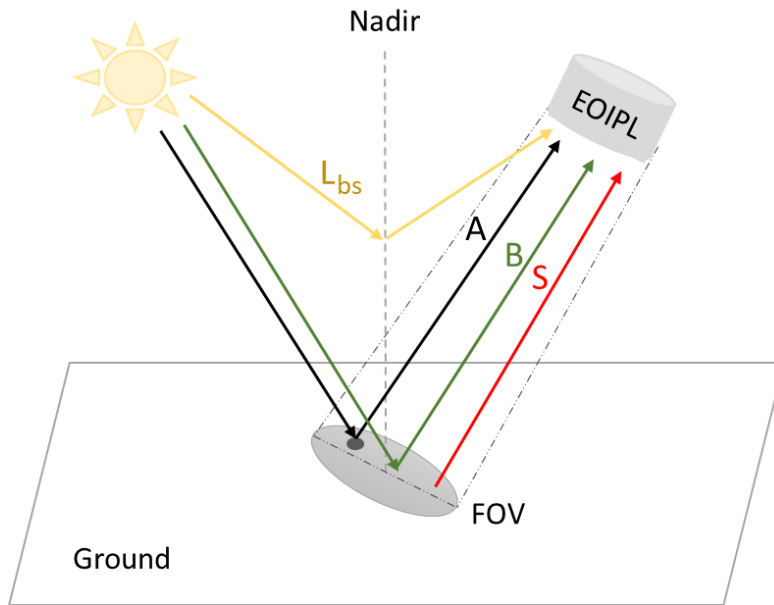


Figure 2.4.2.1. Light paths included in MODTRAN simulation atmospheric model scheme.

Spectral radiance is also expressed as the summation of the reflected signal and haze terms from the atmosphere [10, 16].

$$L(x, y) = \rho_\lambda(x, y)L_s(\lambda) + L_h(\lambda) \quad \text{Eq. 2.101}$$

where the signal and the haze terms are expressed as:

$$L_s(\lambda) = \frac{A(\lambda)}{1 - \rho_e S(\lambda)} \quad \text{Eq. 2.102}$$

$$L_h(\lambda) = \frac{B(\lambda)\rho_e}{1 - \rho_e S(\lambda)} + L_{bs}(\lambda) \quad \text{Eq. 2.103}$$

Moderate Resolution Atmospheric Transmission (MODTRAN) radiative transfer code released by Air Force Research Lab. (AFRL) is used to generate signal and haze terms of the spectral radiance. MODTRAN code calculates radiance at a specific path through an atmospheric model. Self-emission of the atmosphere, scattering by solar or lunar radiance, solar irradiance through the path to space and multiple scattering from sun or atmosphere in the path are the main contributors of the radiance simulations of MODTRAN. Physical parameters like pressure, temperature, extinction coefficient and molecular absorption are defined for 33 atmospheric layers up to 100 km altitude. Also aerosol models are applied to simulate the particles in the path. Following atmospheric models are included in MODTRAN:

- 1976 US Standard
- Tropical (15° North)
- Mid-latitude Summer (July, 45° North)
- Mid-latitude Winter (January, 45° North)
- Subarctic Summer (July, 60° North)
- Subarctic Winter (January, 50° North)

Ground Reflected (GRND RFLT) and Solar Scattered (SOL SCAT) (denoted by $L_{GR}(\lambda)$ and $L_{SS}(\lambda)$) columns in the standart MODTRAN output file represents the haze and signal terms.

$$L_{GR}(\lambda) = \frac{A(\lambda)\rho_\lambda}{1 - \rho_e S(\lambda)} \quad \text{Eq. 2.104}$$

$$L_{SS}(\lambda) = \frac{B(\lambda)\rho_e}{1 - \rho_e S(\lambda)} + L_{bs}(\lambda) \quad \text{Eq. 2.105}$$

Path terms of the radiance data for same geometry and atmosphere conditions can be calculated by using two data sets varying only with albedo values [16, 46].

$$S(\lambda) = \frac{\frac{L_{GR_1}(\lambda)}{\rho_{\lambda_1}} - \frac{L_{GR_2}(\lambda)}{\rho_{\lambda_1}}}{L_{GR_1}(\lambda) - L_{GR_2}(\lambda)} \quad \text{Eq. 2.106}$$

$$A(\lambda) = L_{GR_1}(\lambda)L_{GR_2}(\lambda) \frac{\frac{1}{\rho_{\lambda_1}} - \frac{1}{\rho_{\lambda_2}}}{L_{GR_1}(\lambda) - L_{GR_2}(\lambda)} \quad \text{Eq. 2.107}$$

$$B(\lambda) = L_{GR_1}(\lambda)L_{GR_2}(\lambda) \frac{(L_{SS_1}(\lambda) - L_{SS_2}(\lambda)) \left(\frac{1}{\rho_{\lambda_1}} - \frac{1}{\rho_{\lambda_2}} \right)}{(L_{GR_1}(\lambda) - L_{GR_2}(\lambda))^2} \quad \text{Eq. 2.108}$$

$$L_{bs}(\lambda) = \frac{L_{GR_1}L_{SS_2} - L_{GR_2}L_{SS_1}}{L_{GR_1}(\lambda) - L_{GR_2}(\lambda)} \quad \text{Eq. 2.109}$$

After generating the path terms, for the specific atmospheric and geometric conditions the spectral radiance for varying albedo can be calculated for each pixel. In spite of generating pixel-by-pixel radiance data from MODTRAN, path terms are calculated from MODTRAN outputs with different albedo values. Finally a data cube for spatially and spectrally varying conditions (denoted as $L(x, y, \lambda)$) is generated. An example signal and haze spectral data generated from MODTRAN is given in Figure 2.4.2.2.

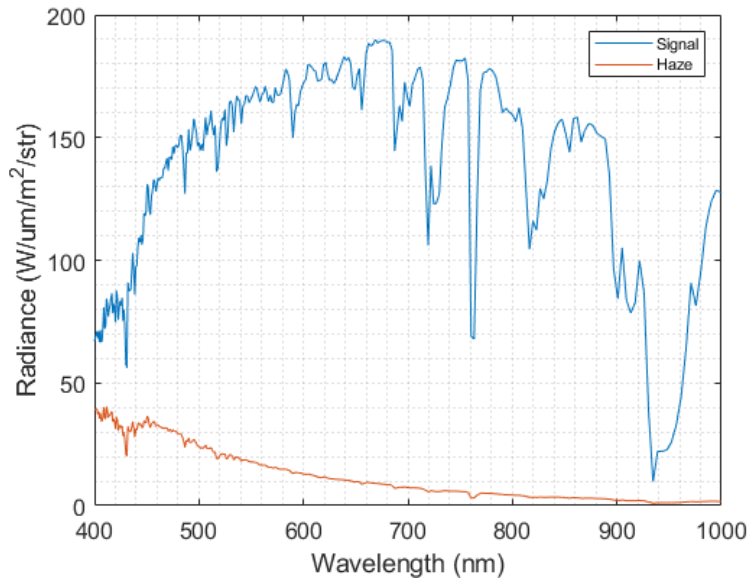


Figure 2.4.2.2. Example 40 SZA signal and haze data calculation by using MODTRAN and IQA.

2.4.3 Applying Polychromatic MTF to Spectrally varying TOA Radiance

Imaging equation in the Fourier domain can be expressed in terms of spatial frequency (lp/mm). Also the spectral width and resolution of the radiance distribution are specified by bandwidth of the spectral band and the spectral resolution of MODTRAN output data. Spectral and spatial frequency scales are generated by considering input sample image spatial resolution, MODTRAN radiance output spectral resolution and spectral band width of the band. Spatial frequency increments of the spatial frequency scale is calculated by considering the input sample image as [16]:

$$\Delta f_x = \frac{r_x}{p_x * N_x} \quad \text{Eq. 2.110}$$

$$\Delta f_y = \frac{r_y}{p_y * N_y} \quad \text{Eq. 2.111}$$

where r_x and r_y are the resampling ratios along x and y directions, p_x and p_y are the pixel pitch sizes along x and y directions, N_x and N_y are the input image dimensions along x and y directions.

Diffraction, Wavefront Error (WFE), defocusing and diffusion MTFs are varying with wavelength. Especially for PAN band polychromatic effects are very significant because of the big difference between initial and final wavelengths. MTF is calculated for each wavelength element in MODTRAN output spectral scale by considering also sampling quality (Q). Resolution scale of polychromatic MTF is given in Figure 2.4.3.1.

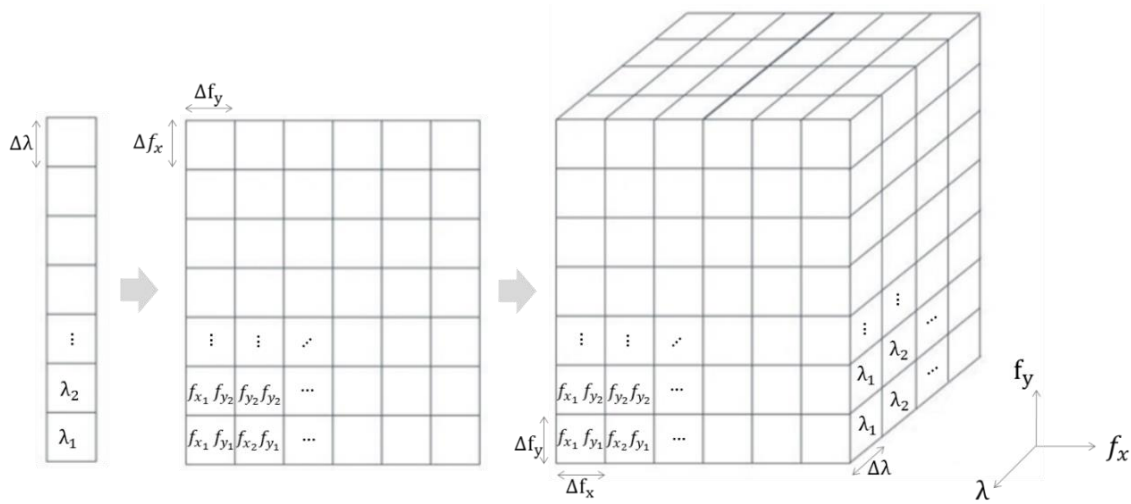


Figure 2.4.3.1. Spatial and spectral resolution scale of polychromatic MTF is calculated by using MTF optimization parameters simulated in GIQE model and spectral radiance data generated by MODTRAN program.

Total system polychromatic MTF function is calculated by multiplying the polychromatic MTF subcomponents modeled for each imaging chain link. Total system polychromatic function is expressed as:

$$MTF_{system}(f_x, f_y, \lambda) = MTF_{opt}(f_x, f_y, \lambda) \cdot MTF_{det}(f_x, f_y, \lambda) \cdot MTF_{smear}(f_x, f_y, \lambda) \dots \quad Eq. 2.112$$

Polychromatic MTF equations used during image simulation are given below in Table 2.4.3.1. Each MTF subcomponent of the polychromatic MTF function modifies the spatial frequency response of the EOIPL. Diffraction MTF is calculated over radially symmetrical spatial frequency input. System spatial frequency cut off is changing over simulated spectral channel. Diffraction MTF for each wavelength increment is calculated separately to form polychromatic diffraction. By using the main assumption that the EOIPL design is an LSI system, aberrations are simulated as Hufnagel statistical aberration model with radial spatial frequency input. On the other hand, detector footprint MTF is only depending on imaging direction and given as the product of the MTFs for along and across directions of scan. Diffusion MTF represents the change in the photon absorption and the random walk of photoelectrons in detector well depending on wavelength. By definition, it is not depending on scanning calculation and calculated by using radially symmetrical spatial frequency input. Platform smear motion is interpreted as linear motion errors in x and y

directions while the platform jitter motion error is evaluated as the high frequency random motion errors in boresight. Platform smear and platform jitter MTF degradations are simulated by using spatially varying and radially symmetrical frequency inputs, respectively. Atmospheric degradations in total system MTF is evaluated by considering cloudlike blur in imaging plane and calculated by using radially symmetrical spatial frequency input. TDI degradations generated by the clock rate mismatch caused by boresight instability is calculated over along scan direction only. Image plane rotations caused during TDI steps are not included in IQA calculations.

Table 2.4.3.1. Polychromatic MTF equations included in image simulation module of IQA program.

MTF Breakdown	Equation
Diffraction	$MTF_{diffraction}(f_r)$
WFE	$MTF_{WFE}(f_r)$
Defocusing	$MTF_{defocus}(f_r)$
Detector Footprint	$MTF_{footprint}(f_x, f_y) = MTF_{footprint}(f_x)MTF_{footprint}(f_y)$
Diffusion	$MTF_{diffusion}(f_r)$
Detector smear	$MTF_{smear}(f_y)$
Atmosphere smear	$MTF_{atmosphere}(f_r)$
Platform smear	$MTF_{smear}(f_x, f_y) = MTF_{smear}(f_x)MTF_{smear}(f_y)$
Platform jitter	$MTF_{jitter}(f_r)$
TDI	$MTF_{TDI}(f_y)$

Imaging equation in the Fourier domain contains TOA radiance spectrum which makes essential to use the Fourier transform of the TOA radiance. It should be noted that after taking the Fourier transform, radiance spectrum should be moved to the center for applying the polychromatic MTF to the radiance spectrum with the same spatial frequency scale [23]. In Figure 2.4.3.2, Fourier transform and center shifting process representations are demonstrated.

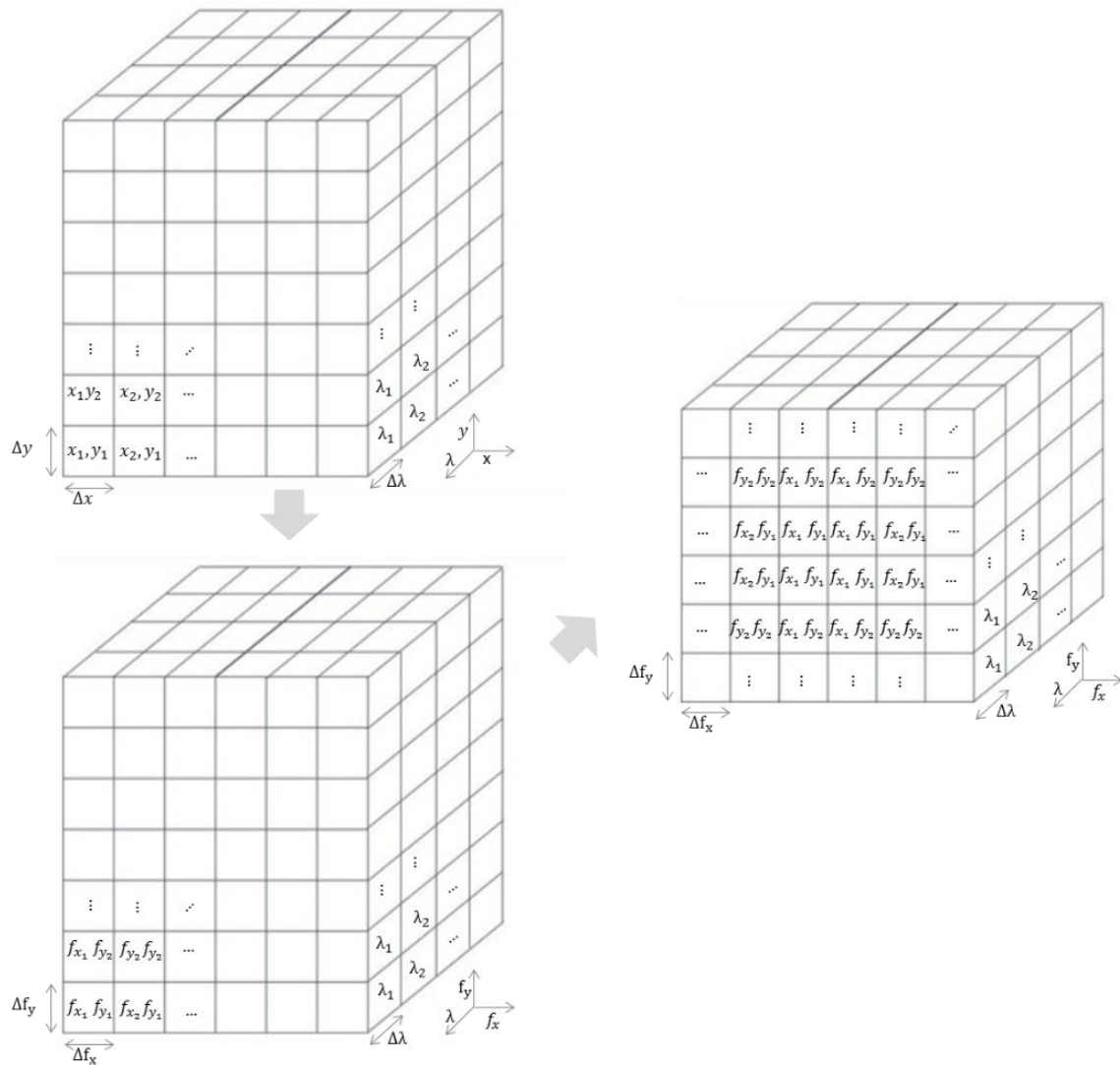


Figure 2.4.3.2. After taking the Fourier transform center of the TOA radiance spectrum is shifted to match the scale of polychromatic MTF function.

By taking the product of polychromatic MTF and TOA radiance spectrum, degraded radiance spectrum is calculated. Schematic example of degraded radiance spectrum generation is shown in Figure 2.4.3.3 TOA radiance spectrum is simulated by using spectral radiance data generated by MODTRAN.

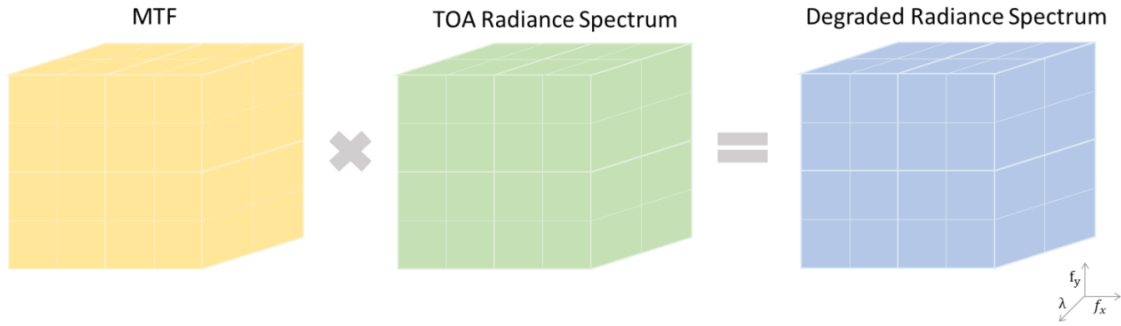


Figure 2.4.3.3. Degraded radiance spectrum is calculated by multiplying MTF and TOA radiance spectrum simulations.

After application of the MTF degraded radiance spectrum is unwrapped from central shift and inverse Fourier transform is applied to attain MTF degraded radiance data.

$$L_{degraded}(x, y, \lambda) = FT^{-1} \{ MTF(f_x, f_y, \lambda) FT\{L(x, y, \lambda)\} \} \quad Eq. 2.113$$

where $L(x, y, \lambda)$ is spatially and spectrally varying radiance data.

Finally by considering the total spectral transmission of the EOIPL, degraded image radiance is calculated by taking the spectrally weighted sum of the MTF degraded radiance data. Spatially varying degraded radiance is given as [16]:

$$L_{degraded}(x, y) = \int_{\lambda_{min}}^{\lambda_{max}} L_{degraded}(x, y, \lambda) TT(\lambda) \frac{\lambda}{\lambda_{mean}} d\lambda \quad Eq. 2.114$$

where $TT(\lambda)$ is total spectral transmission, λ_{mean} is the mean wavelength and λ is wavelength.

2.4.4 GSD Resampling

Image radiance data is resampled to represent the spatial resolution of the simulated EOIPL in IQA program. Spatial scale of the image radiance data

should be resampled by using bilinear interpolation method. Bilinear interpolation method is used to ensure the non-integer resampling ratio resampling operations accuracy [14, 16].

2.4.5 Image Radiance to Photoelectron Count per Pixel Conversion

Image radiance to photoelectron count per pixel conversion included in IQA program is given by following equation [10, 16]:

$$n_{photons}(x, y) = \frac{\left[(1 - e)(p^2)(TDI * T_{int}) \left(\frac{\pi}{4 * \left(\frac{f_{eff}}{D} \right)} \right) \right] (L(x, y))}{\left(\frac{h_{planck}c}{\lambda_{mean}} \right)} \quad Eq. 2.115$$

where e is obscuration ratio, TDI is number of TDI steps, T_{int} is integration time of a pixel, f_{eff} is effective focal length, D is M1 mirror diameter, h_{planck} is Planck constant, c is speed of light and λ_{mean} is the mean wavelength.

2.4.6 Noise Addition to Photo-electron Count

Sensor noise is defined as randomly generated electrons during photo-electron digital number conversion. Main contributors of the noise in the visible band for Charge Coupled Device (CCD) sensors simulated in IQA program are:

- i. photon noise,
- ii. quantization noise,
- iii. read noise

Randomly distributed noise components are quantified by using the statistical distribution standard deviation. Total noise variance is calculated as the sum of each noise source variances if noise sources are independent. Total noise standard deviation is defined as:

$$\sigma_{noise}(x, y) = \sqrt{\sum_{n=1}^N \sigma_n^2} = \sqrt{n_{photons}(x, y) + \sigma_{quantization}^2 + \sigma_{read_noise}^2} \quad Eq. 2.116$$

where $n_{photons}(x, y)$ is photoelectron count, $\sigma_{quantization}$ is quantization noise variance and $\sigma_{read_noise}^2$ is read noise variance.

Photon noise arises because of the random fluctuations in the quantization level. These random fluctuations are results of the differences in the arrival time of the electrons to the detector well. Because of the fact that photon noise shows Poisson distribution, photon noise variance is equal to the photo electron count.

$$\sigma_{photon}^2(x, y) = n_{photons}(x, y) \quad Eq. 2.117$$

During the conversion of photo-electron count to digital number, quantization noise is generated during the conversion of signals into integer values. An example for the quantization noise is given in Figure 2.4.6.1. Four cases are illustrated in the example. Although the photo-electron count for each cases are different, the digital number remains constant. The uncertainty of the number of photoelectron counts in the same digital number bin brings out the quantization noise.

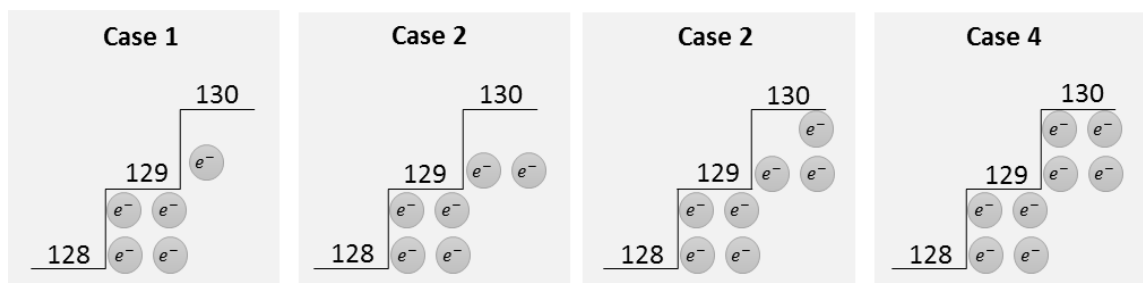


Figure 2.4.6.1. Quantization noise example.

Quantization noise is expressed by using uniform distribution standard deviation because each level of the quantization steps are uniformly distributed. Quantization noise standard deviation is derived by following equations [14]:

$$\sigma_{uniform} = \sqrt{\int_0^1 x^2 dx - \left(\int_0^1 x dx\right)^2} = \frac{1}{\sqrt{12}} \quad Eq. 2.118$$

where $\sigma_{uniform}$ is uniform distribution standard deviation.

$$\sigma_{quantization} = \sigma_{uniform} \frac{FWC}{DR} = \frac{1}{\sqrt{12}} \frac{FWC}{DR} \quad Eq. 2.119$$

where FWC is full well capacity, DR is dynamic range and $\sigma_{quantization}$ is standard deviation of quantization noise.

Read noise (denoted as σ_{read_noise}) ensued as a result of detector voltage variations during reading output voltage. Total noise electron count of the EOIP is calculated by multiplying the total noise standard deviation with a uniformly distributed random matrix between 0 and 1 with the same dimensions as photoelectron count matrix. Noise added spatially varying photoelectron count is expressed by [10, 29]:

$$n_{noise_added}(x, y) = n_{photons}(x, y) + rnd_{(x,y)}(0,1) * \sigma_{noise}(x, y) \quad Eq. 2.120$$

where $rnd_{(x,y)}(0,1)$ is matrix in the size of photon count matrix consists of random numbers between zero and one, $\sigma_{noise}(x, y)$ is total noise and $n_{photons}(x, y)$ photoelectron count.

2.4.7 Photoelectron Count to Digital Number Conversion

The final step of the IQA image simulation module is the conversion between

the photo-electron count to digital number. At this stage the photo-electrons are first converted to voltage. Then by using Analog to Digital Converter (ADC) the signals are quantized to digital numbers. Quantum Step Equivalence (QSE) in Figure 2.4.7.1 represents the scaling ratio of the number of photoelectrons to digital numbers [14]. QSE is the product of the conversion gain and slope of the digital number to number of photo-electrons in the detector well graph. Change in the voltage during readout on each detector well is defined as conversion gain. Conversion gain is depending on the detailed design of the EOIPL readout circuit. In case of the conversion gain is not known, it is calculated for the case that Focal Plane Array (FPA) is not saturated. QSE and Digital Number (DN) are expressed as [14, 16, 21]:

$$QSE = \tan(\theta) = \frac{G_c FWC}{DR} \quad \text{Eq. 2.121}$$

$$DN(x, y) = \text{int} \left\{ \frac{n_{photons}(x, y)}{QSE} \right\} \quad \text{Eq. 2.122}$$

where G_c is conversion gain, FWC is full well capacity, DR is dynamic range, QSE is quantum step equivalence and $n_{photons}$ is number of photoelectrons.

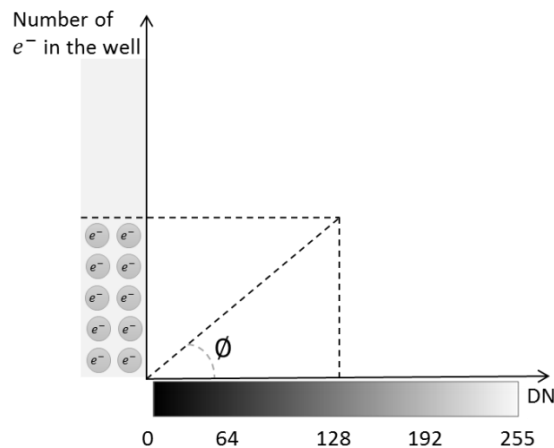


Figure 2.4.7.1. Quantum step equivalence is the slope between number of electrons in the well and the DR.

2.5 IQA Operational Flow and IQA Outputs

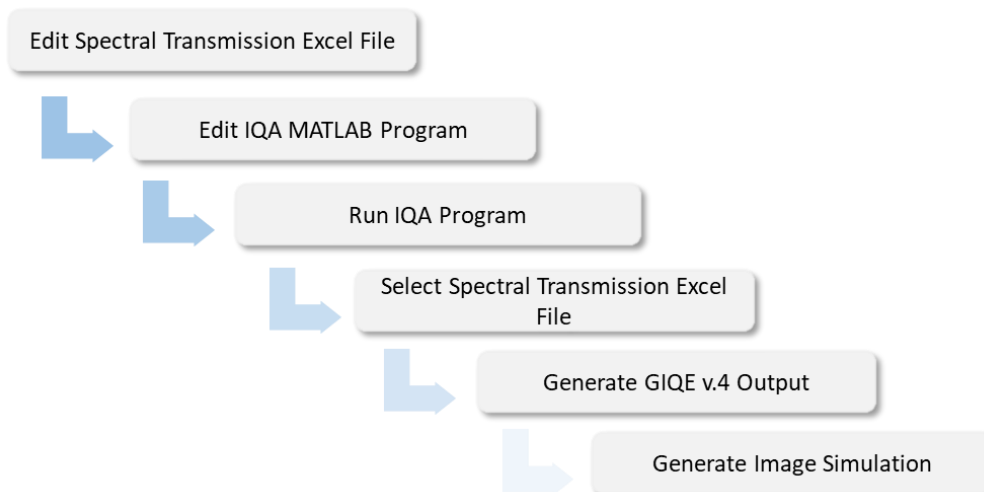


Figure 2.5.1. Operational flow of the IQA program.

In Figure , operational flow of IQA program is represented. Before running the IQA program, spectral transmission excel file of the EO IPL must be edited and emplaced on the folder that the IQA program existed as described in section Spectral Transmission Data Input2.1. After generating the input spectral transmission excel file, the syntax lines that contains input parameters in IQA program must be arranged as indicated in sections 2.1.2, 2.1.3 and 2.1.4. When the user presses on the run button in MATLAB, IQA program requests the spectral transmission input data with generating a pop-up window for selection. After the selection of the spectral transmission excel file, the program will compute the GIQE analysis and the PAN image simulation.

GIQE analysis output is generated as a MATLAB figure format given in Figure . GSD, RER, SNR and GIQE parameter calculated by considering the EO IPL system design parameters and imaging conditions. Also optimized MTF values for EO IPL system breakdown are in between the second and thirteenth lines. MTF optimization parameters described in Table 2.1.4.1 are indicated between fifteenth and twentieth lines. SNR and GIQE parameters are calculated both for constant albedo SNR calculation and SNR definition in GIQE v.4. described in section 2.3.4. Also RER, SNR and GIQE parameters are calculated for both cases with and without TDI application.

	Parameter	Value
1	GSD	0.5000
2	Optics MTF	0.3479
3	RMS MTF	0.9053
4	Defocus MTF	0.9990
5	Detector MTF	0.5910
6	Detector Smear MTF	1.0000
7	Payload MTF	0.1860
8	Smear MTF	0.9992
9	Jitter MTF	0.9990
10	TDI MTF	0.9968
11	Atmosphere MTF	0.9992
12	Satellite MTF	0.1849
13	Satellite TDI MTF	0.1843
14	WFE tolerance	0.0507
15	WFE RMS	0.0502
16	W_pp	0.0140
17	L_D	4.6350
18	Smear error	0.0450
19	Atmosphere error	0.0450
20	Jitter error	0.0140
21	TDI	32
22	RER	0.8332
23	TDI RER	0.8322
24	SNR	134.5628
25	SNR_delta	79.1108
26	GIQE	5.2917
27	GIQE delta SNR	5.2899
28	GIQE TDI	5.2917
29	GIQE TDI delta SNR	5.2899

Figure 2.5.2. GIQE output is generated as a table in “.fig” file format.

Another output of the IQA program is the simulations for panchromatic and multispectral band images. Image simulations are generated based on GIQE model outputs and by considering system design inputs and imaging conditions. Output file format for image simulations are tiff. Image outputs are saved in the file containing the IQA program.

3 EXAMPLE EOIPL DESIGN

In this section; the viewing geometry, telescope and detector characteristics of an example EOIPL design will be examined in more detail. Main assumptions considering during EOIPL design will be given. Following design steps are considering during EOIPL design with high spatial resolution characteristics:

- i. Determining the EOIPL requirements,
- ii. Defining imaging geometry and resolution limits

- iii. Defining telescope and detector characteristics depending on object radiance requirements,
- iv. Calculating image quality link budget of the EOIPL design by considering SNR, MTF and GSD

The common objective of commercial satellites in remote sensing industry is to ensure high quality image production with manageable amount of data rate and low cost. Depending on customer requirements, spectral and spatial resolution characteristics of the EOIPL are specified. As a guideline to the example EOIPL design, properties of some of the sub-meter resolution electro-optic imaging satellites are given in Table. It is obvious that the most important priority of the commercial satellite imagery production is to provide images with high spatial and spectral resolution. Especially depending on utilization area, the number of spectral bands and spectral band widths are determined.

Table 3.1. Commercial high resolution electro-optic imaging satellites [49, 50].

Satellites	Telescope & Detector	GSD (m)	PAN band (nm)	Altitude (km)	MS band (nm)
IKONOS	Cassegrain – TDI CCD	0.82	450-900	681	450-530 (blue) 520-610 (green) 640-720 (red) 760-860 (NIR)
GeoEye-1	Three Mirror Anastigmatic – TDI CCD	0.41	450-900	681	450-510 (blue) 520-580 (green) 655-690 (red) 780-920 (NIR)
EarlyBird	Gimbaled Mirror System - Staring CCD	3	450-800	470	450-590 MS1 610-680 MS2 790-890 MS3
QuickBird-2	Three Mirror Anastigmatic – TDI CCD	0.61	450-900	450	450-520 (blue) 520-600 (green) 630-690 (red) 760-900 (NIR)
WorldView-1	Three Mirror Anastigmatic- TDI CCD	0.5	450-900	496	-

The example EOIPL features a telescope design with Cassegrain type. In Cassegrain telescopes, the incident light falling on the aperture is reflected from the primary mirror to secondary mirror at first. The reflected light from the second mirror passes from the obscuration on the primary mirror and falls on the Focal Plane Assembly (FPA). Primary and secondary mirrors are

paraboloidal and hyperboloidal, respectively [51]. A Cassegrain telescope example ZEMAX figure is given in Figure 3.1. The telescope primary mirror features an M1 mirror with 69 cm diameter and 0.1 obscuration rate with 12 m effective focal length.

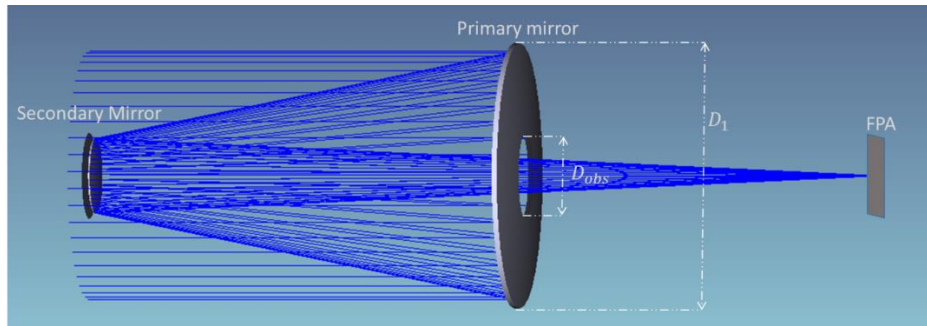


Figure 3.1. Cassegrain telescope example simulated in ZEMAX.

FPA consists of multispectral pushbroom Time Delay Integration (TDI) CCD detector array to scan the objects in the ground. Red, green and blue bands are employed as multispectral bands. PAN and MS band pixel pitch sizes are 10 μm and 30 μm , respectively. Multispectral and panchromatic bands are simultaneously imaging the scene. For the along-scan direction, detector uses multiple TDI lines of the same object to accumulate more electrons to enhance SNR value. Each pixel of the detector is divided into four sub-pixels to increase the data rate efficiency. Subpixels are read out at the same time to increase the data rate. This sub-pixel technology is mostly used in large area sensors [21]. An example of subpixel read out is given in Figure 3.2. Multispectral detector with one PAN and four multispectral channels is based on implementation of the spectral filters on TDI detector arrays. On board electronics of the FPA provides 12-bit image data without data compression.

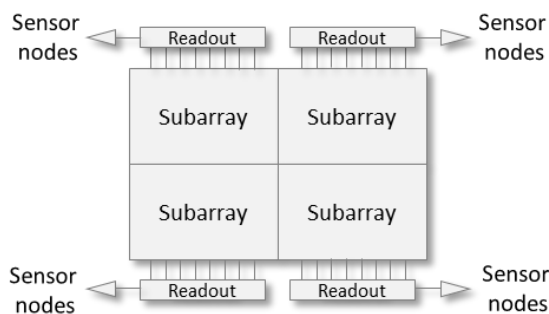


Figure 3.2. Subpixel design of the example EOIPL detector.

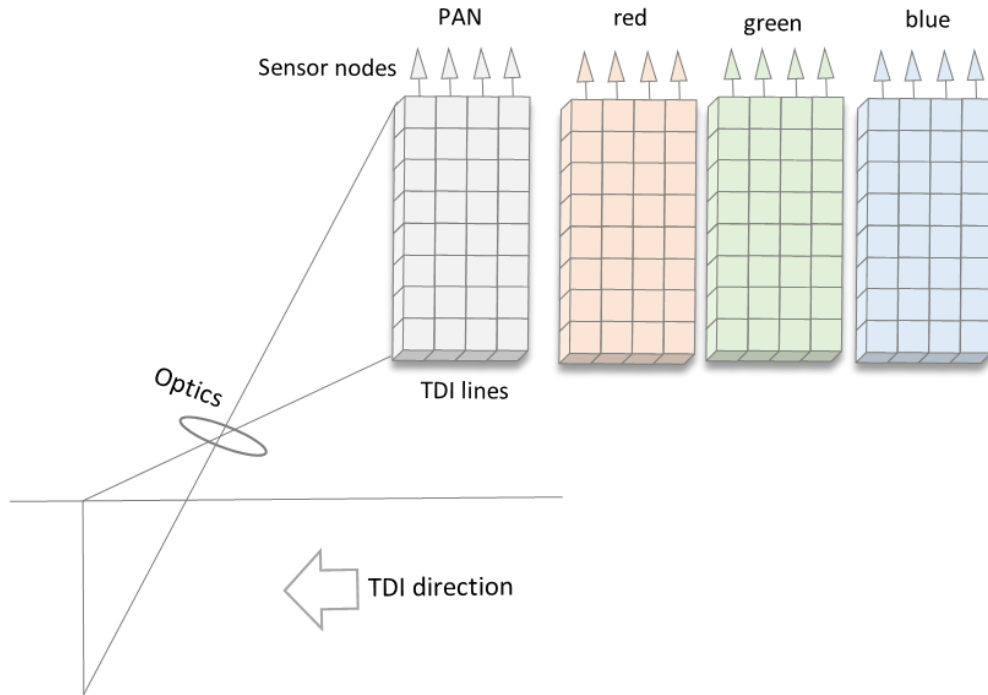


Figure 3.3. Multispectral TDI detector architecture of the EOIPL design.

Pushbroom imaging geometry is defined for viewing geometry at 600 km altitude with 0.5 m GSD. EOIPL scan direction parallel to satellite orbital motion is defined as along scan direction in Push broom imaging geometry. The direction perpendicular to the along scan direction is defined as across scan direction. Projection of each TDI line in the across scan direction covers the swath width of the EOIPL on the ground. Reflected radiance from GSD is degraded by atmosphere and finally accumulated as photo-electrons in detector.

To attain maximum sampling efficiency from the EOIPL design, sampling quality parameter is set to 1. Design parameters of the example EOIPL is given in Table 3.2. Pixel sizes are 10 μm for PAN band and 30 μm for MS bands. The focal length of the telescope is calculated from the operation altitude, pixel pitch size and the altitude.

$$f_{eff} = \frac{p * h}{GSD} \quad \text{Eq. 3.1}$$

where p is pixel pitch size, h is altitude and GSD is ground sampling distance.

Note that optical design parameters are optimized to have sampling quality parameter which is equal to 1. SSF limit is calculated as 100 lp/m while the DSF limit of the EOIPL is calculated 100 lp/mm. Pixel pitch size parameter was kept as variable to attain an EOIPL design with $Q=1$. Aperture size of the EOIPL is based on assumption that sufficient light is entering to the aperture. Spectral transmission characteristics are defined by considering transmission within visible band with red, green and blue channels. Total detector noise and full well capacity parameters are assumed as $50 e^-$ and $15000 e^-$ per pixel as considering the imaging chain simulations in the literature [10, 16]. Total spectral transmission data for example EOIPL design is given in Figure 3.4.

Table 3.2. EOIPL system design parameters.

Physical Design Parameters	Values	Spectral Design Parameters	Values
Aperture size (m)	0.69	Q at (PAN mean) (a.u.)	1
Obscuration rate (a.u.)	0.1	PAN spectral band (nm)	450-700
Focal length (m)	12	Blue spectral band (nm)	450-520
Optical Design	Cassegrain	Green spectral band (nm)	500-600
PAN pixel size (μm)	10	Red spectral band (nm)	600-700
MS pixel size (μm)	30	Average Total PAN Transmission (a.u.)	0.5
Altitude (km)	600	Average Total MS Transmission (a.u.)	0.4
PAN GSD (m)	0.5		
MS GSD (m)	1.5		
Total PAN detector noise (e^-)	50		
Total MS detector noise (e^-)	200		
PAN Full Well Capacity (e^-)	15000		
MS Full Well Capacity (e^-)	150000		
Detector Fill Factor (a.u.)	1		
Quantization (bits)	12		

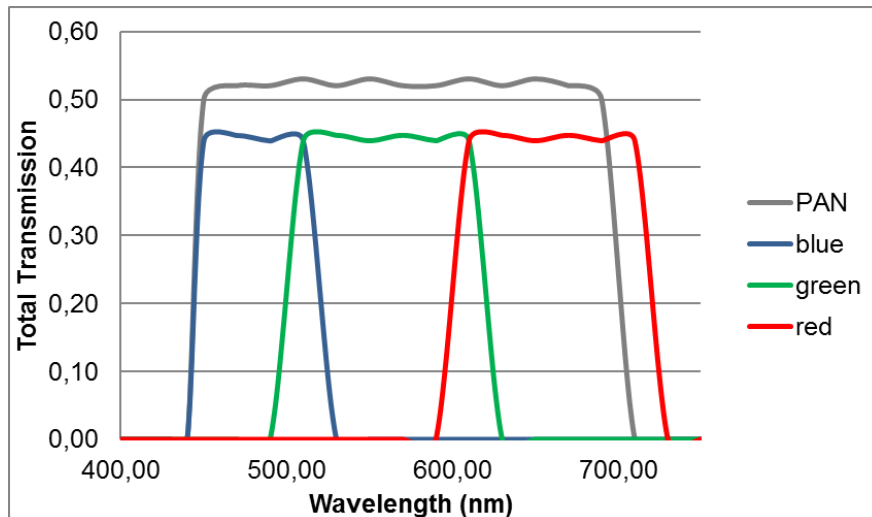


Figure 3.4. Total spectral transmission for example EOIPL design.

4 RESULTS

Image quality analysis of example EOIPL design is evaluated within the scope of this thesis study. GIQE model and image simulations are produced for differential degradation datasets. Degradation tasks are impacted on GIQE model and image simulations to address the relationship between the physical image quality parameters and the image simulations. The results of these simulations are given below.

First of all comparison of the MTF and SNR outputs of IQA and other simulations in the literature are evaluated. The MTF breakdown of generic EOIPL systems included in Picasso and ICS imaging chain simulators are calculated in IQA program. Comparison of the MTF values of IQA and other simulators at sampling NSF are given in Table 4.1. ICS simulator calculates the diffraction MTF by using the normalized autocorrelation of the aperture function. Also ICS contains the diffraction pattern of the spider arms that holds the mirror mechanism. Difference of MTF values at NSF in the order of 0.001 can probably accounted for the fact that IQA does not contain diffraction calculation for spider arms. SNR at constant albedo simulations for GENSAT example included in ICS imaging chain simulator is used for validation of the SNR calculations. SNR simulations are done for 40 SZA, Mid-latitude Summer Atmosphere Model and 23-km visibility. The SNR comparison between IQA and ICS imaging chain simulators is given in Table 4.2. The MTF and SNR values derived from IQA are consistent with the image quality parameters of ICS and

Picasso imaging chain simulators. The PAN channel image simulations for the generic imager designs in ICS and Picasso imaging chain simulators are given in Figure 4.1, respectively.

Table 4.1. MTF calculations are validated by using GENSAT1 and GENSAT2 designs included in Picasso and ICS articles [10, 16].

MTF Degradation (a.u.)	Picasso GENSAT1	IQA GENSAT1	ICS GENSAT2	IQA GENSAT2
Optics MTF	0.377	0.377	0.313	0.309
WFE MTF	0.674	0.674	0.693	0.692
Detector MTF	0.590	0.590	0.249	0.250
Atmosphere MTF	1.000	1.000	0.990	0.990
System MTF	0.150	0.149	0.054	0.053

Table 4.2. SNR at constant albedo calculations are validated by using GENSAT2 design included in ICS article [10].

TDI (a.u.)	ICS GENSAT2 PAN SNR (a.u.)	IQA GENSAT2 PAN SNR (a.u.)
2	19	20
4	33	35
8	55	59
16	88	93
32	133	140
48	167	176
64	196	206
96	243	256
128	282	297



Figure 4.1. Image simulation outputs of IQA program for Picasso GENSAT1(left) and ICS GENSAT2 (right), respectively.

GIQE model and images for PAN and MS bands are simulated for EOIPL design given in chapter 3 by using IQA program. The MTF subcomponent breakdown for example EOIPL design is given in Table 4.3 for PAN and MS bands. The design optimization parameters necessary to attain related MTF breakdown values at NSF are presented in Table 4.4. 0.05λ wavefront error should be implemented for tolerance and rms WFE MTF degradations while 0.07λ peak to peak wavefront error is simulated to have defocusing MTF value described in design for PAN band. Peak to peak wavefront error degradations are varying depending on spectral band while the wavefront errors for tolerance and RMS degradations are kept the same with the PAN simulations for MS bands. For the detector MTF breakdown detector footprint, detector smear and diffusion MTF degradations are calculated. Depletion width of the diffusion MTF degradations that is calculated by keeping diffusion length constant as $150\ \mu\text{m}$ is given in Table 4.4. To calculate satellite level MTF platform smear, platform jitter, TDI and atmosphere smear MTF degradations are implemented on payload level MTF. As it can be seen from the Table 4.4 MS band smear error, jitter error and atmosphere error optimized degraded parameters simulated in IQA are less than PAN band degradation parameters. By design, the MS band pixel pitch sizes are three times greater than the PAN band. This brings out the fact that the ratio between the boresight mismatch distance and pixel pitch size is bigger for PAN band for same velocity error in the orbit. GIQE breakdown for PAN and RGB bands are given in Table 4.5.



Figure 4.2. IQA PAN (top), blue (lower left), green (lower middle) and red (lower right) band image simulations for example EOIPL design, respectively.

As can be seen in the Table 4.6 to Table 4.12 GIQE degradations depending on platform smear, platform jitter, defocusing, wavefront error and number of TDI steps are simulated in IQA as image quality budget analysis of the EOIPL system. The first row of each table contains the degradation level of the image simulation given in Figure .

GIQE breakdown simulated with IQA is given. GIQE model is calculated by using 40° SZA Mid-Latitude Summer atmosphere model. SNR for PAN band is calculated as 79 for 32 TDI steps. Wavelength scale is increased by 3 nm resolution during the calculation of the photon count in SNR calculations. SNR values for blue, green and red bands are calculated as 168, 212 and 246, respectively. RER parameter is calculated as 0.466 for PAN band while ranging between 0.665 and 0.710 for MS bands. Finally GIQE value for PAN band is

5.222. MS band GIQE values are between 4.152 and 4.233 values. Example images simulated for example EOIPL system design with IQA is given in Figure 4.2. PAN band image simulation represents the image quality values of 0.5 m GSD, 0.15 system MTF, 79 SNR for 32 TDI and 40° SZA and 5.224 GIQE value. GSD value of MS band image simulations is 1.5 m as it can be deduced from the detail losses and the image size Figure . SNR values for MS bands are 168, 212 and 246 for blue, green and red bands, respectively. Higher SNR value of red band than blue and green bands brings out the ability to separate objects with close albedo values from each other. Lowest SNR value of blue band introduces degradation of image interpretability. It is important to notice that in spite of the fact that MTF value for PAN band is more less than the half of the average MTF values of the MS band, other image quality degradation factors like SNR and GSD brings out lower image quality in MS bands. IQA simulations point out an important subject which evaluating the image quality of an EOIPL system by using GIQE equations are more reliable than by using individual image quality parameters like GSD, MTF and SNR.

Table 4.3 MTF breakdown of example EOIPL.

MTF Degradation (a.u.)	PAN		Blue		Green		Red	
	aln.	acc.	aln.	acc.	aln.	acc.	aln.	acc.
Optics	0.35	0.35	0.77	0.77	0.74	0.74	0.70	0.70
RMS	0.91	0.91	0.95	0.95	0.94	0.94	0.93	0.93
Defocus	0.98	0.98	0.99	0.99	0.99	0.99	0.99	0.99
Detector	0.58	0.59	0.59	0.60	0.59	0.60	0.59	0.60
Detector Smear	0.97	1.00	0.97	1.00	0.97	1.00	0.97	1.00
Payload	0.18	0.18	0.42	0.43	0.40	0.41	0.37	0.38
Smear	0.90	0.95	0.99	0.99	0.99	0.99	0.99	0.99
Jitter	0.95	0.95	0.99	0.99	0.99	0.99	0.99	0.99
TDI	1.00	1.00	0.97	1.00	0.97	1.00	0.97	1.00
Atmosphere	0.95	0.95	0.99	0.99	0.99	0.99	0.99	0.99
Satellite TDI	0.14	0.15	0.38	0.42	0.36	0.40	0.34	0.37

Table 4.4. Optimized degradation parameters of example EOIPL.

Parameter	PAN		Blue		Green		Red	
	aln.	acc.	aln.	acc.	aln.	acc.	aln.	acc.
WFE tolerance (λ)	0.05	0.05	0.05	0.05	0.05	0.05	0.05	0.05
WFE RMS (λ)	0.05	0.05	0.05	0.05	0.05	0.05	0.05	0.05
W_{pp} (λ)	0.07	0.07	0.10	0.10	0.09	0.09	0.08	0.08
L_D (μm)	4.64	4.64	1.61	1.61	4.04	4.04	9.49	9.49
Smear error (pxl)	0.50	0.35	0.16	0.16	0.16	0.16	0.16	0.16
Atmosphere error (pxl)	0.35	0.35	0.16	0.16	0.16	0.16	0.16	0.16
Jitter error (pxl)	0.10	0.10	0.05	0.05	0.05	0.05	0.05	0.05

Table 4.5. GIQE budget simulations with ± 0.3 error for example EOIPL.

Parameter	PAN	Blue	Green	Red
GSD (m)	0.5	1.5	1.5	1.5
RER (a.u.)	0.466	0.710	0.691	0.665
SNR (a.u.)	79	168	212	246
GIQE (a.u.)	5.224	4.233	4.199	4.152

As can be seen in Table 4.6 to Table 4.11, GIQE degradations depending on platform smear, platform jitter, defocusing, wavefront error and number of TDI steps are simulated in IQA as image quality budget analysis of the EOIPL system. The first row of each table contains the degradation level of the image simulation given in Figure .

Table 4.6. Smear GIQE budget with ± 0.3 error of example EOIPL.

PAN			Blue			Green			Red		
Smear (pxl)	MTF (a.u.)	GIQE (a.u.)	Smear (pxl)	MTF (a.u.)	GIQE (a.u.)	Smear (pxl)	MTF (a.u.)	GIQE (a.u.)	Smear (pxl)	MTF (a.u.)	GIQE (a.u.)
0.5	0.14	5.214	0.2	0.38	4.227	0.2	0.36	4.193	0.2	0.34	4.147
1.0	0.10	5.131	0.5	0.35	4.187	0.5	0.33	4.154	0.5	0.31	4.109
1.5	0.05	5.005	1.0	0.25	4.060	1.0	0.24	4.030	1.0	0.22	3.9887

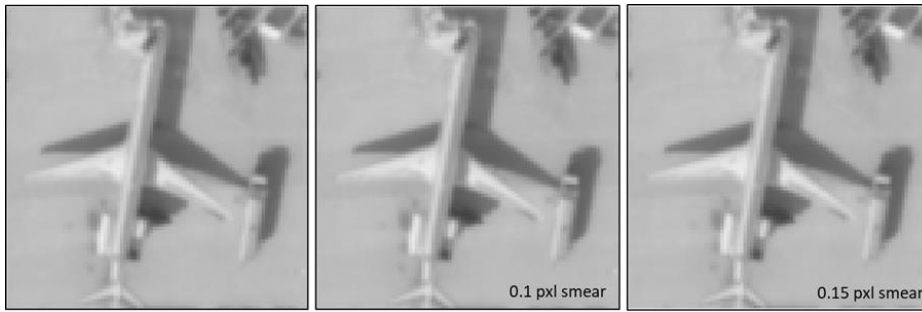


Figure 4.2. PAN band image simulations for no smear (left), 0.1 pixel smear (middle) and 0.15 pixel smear (right) degraded image simulations, respectively.

For the platform smear budget of the EOIPL design image simulation and GIQE model is degraded for 1 and 1.5 pixel smear shifts. The image simulation outputs of the PAN band under given platform smear degradations are given in Figure 4.2. Total MTF is degraded to 0.05 from 0.14 while GIQE is degraded to 5.005 from 5.214 in PAN band. Platform smear with 0.5 and 1 pixel 0.167, 0.163 Δ GIQE for PAN band.

Table 4.7. Jitter GIQE budget with ± 0.3 error for example EOIPL.

PAN			Blue			Green			Red		
Jtr. (pxl)	MTF (a.u.)	GIQE (a.u.)	Jtr. (pxl)	MTF (a.u.)	GIQE (a.u.)	Jtr. (pxl)	MTF (a.u.)	GIQE (a.u.)	Jtr. (pxl)	MTF (a.u.)	GIQE (a.u.)
0.1	0.14	5.214	0.05	0.38	4.227	0.05	0.36	4.193	0.05	0.34	4.15
0.3	0.10	5.117	0.15	0.34	4.185	0.15	0.33	4.152	0.15	0.31	4.11
0.6	0.03	4.877	0.25	0.28	4.108	0.25	0.27	4.077	0.25	0.25	4.03

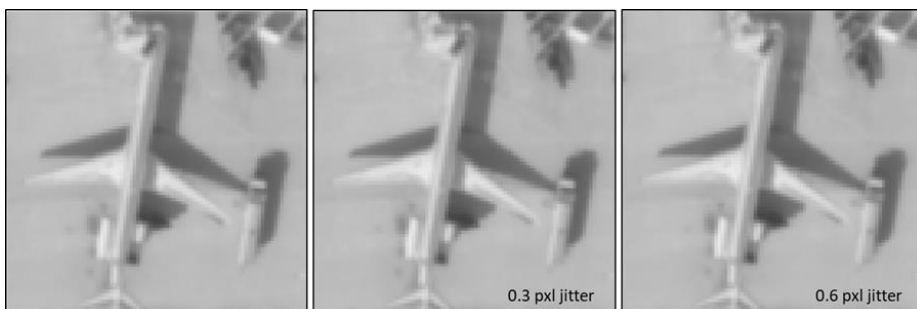


Figure 4.3. PAN band image simulations for EOIPL design (left), 0.3 pixel jitter (middle) and 0.6 pixel jitter (right), respectively.

In Table and Figure 4.3, 0.3 and 0.6 pixel platform jitter are applied to the EOIPL system in IQA. PAN band MTF degrades in the order of 0.11 while Δ GIQE of 0,337 is calculated. Image quality degradation of the PAN band is observed in Figure 4.3. It can be seen that higher GIQE degradation of platform jitter than platform smear is distinguishable as poorer image quality. Also the MS band degradations depending on platform jitter are given in Table 4.7.

Table 4.8. Defocusing GIQE budget with ± 0.3 error for example EOIPL.

PAN			Blue			Green			Red		
Dfcs (λ)	MTF (a.u.)	GIQE (a.u.)	Dfcs (λ)	MTF (a.u.)	GIQE (a.u.)	Dfcs (λ)	MTF (a.u.)	GIQE	Dfcs (λ)	MTF (a.u.)	GIQE (a.u.)
0.07	0.14	5.214	0.10	0.38	4.227	0.09	0.36	4.193	0.08	0.34	4.147
0.25	0.11	5.090	0.30	0.35	4.186	0.30	0.32	4.142	0.30	0.29	4.070
0.50	0.03	4.717	0.50	0.29	4.106	0.50	0.25	4.046	0.50	0.21	3.958



Figure 4.4. PAN band image simulations for EOIPL design (left), 0.25 peak to peak WFE (middle) and 0.5 peak to peak WFE (right) degraded image simulations, respectively.

Defocusing effects for example EOIPL is simulated in Figure 4.4. PAN band MTF is degraded to 0.11 for 0.25 peak to peak WFE while it is degraded to 0.03 for 0.50 peak to peak WFE. It should be considered that even for the fact that the MTF degradation level for 0.50 peak to peak WFE and 0.6 pixel jitter is the same Δ GIQE for defocus error is more than the platform jitter effect. 0,337 GIQE degradation was calculated for 0.6 pixel jitter while Δ GIQE is Δ GIQE for defocusing of the EOIPL. One should pay attention for the case where two simulation results have the same MTF degradation but different GIQE value. MS band defocusing image quality budgets are given in Table 4.8.

Table 4.9. WFE GIQE budget with ± 0.3 error for example EO IPL.

PAN			Blue			Green			Red		
WFE (λ)	MTF (a.u.)	GIQE (a.u.)	WFE (λ)	MTF (a.u.)	GIQE (a.u.)	WFE (λ)	MTF (a.u.)	GIQE (a.u.)	WFE (λ)	MTF (a.u.)	GIQE (a.u.)
0.05	0.14	5.214	0.05	0.38	4.227	0.05	0.36	4.193	0.05	0.34	4.147
0.10	0.11	5.024	0.10	0.32	4.156	0.10	0.30	4.110	0.10	0.27	4.040
0.15	0.07	4.740	0.15	0.25	4.048	0.15	0.22	3.980	0.15	0.19	3.895



Figure 4.5. PAN band image simulations for EO IPL design (left), 0.10λ WFE (middle) and 0.15λ WFE (right) degraded image simulations, respectively.

WFE degradation simulations are given in Figure 4.5 and Table 4.9. 0.1λ and 0.15λ WFE are applied to the example EO IPL for the PAN and RGB bands. MTF is degraded from 0.14 to 0.07 for PAN band while GIQE is decreased to 4.740 for 0.15λ WFE.

Table 4.10. GIQE budget with ± 0.3 error depending on TDI level for PAN band.

TDI (a.u.)	SNR (a.u.)	MTF (a.u.)	GIQE (a.u.)
32	79	0.1438	5.2143
16	49	0.1442	5.2124
8	29	0.1443	5.2075

Table 4.11. GIQE budget with ± 0.3 error depending on TDI level for MS band.

Blue				Green				Red			
TDI (a.u.)	SNR (a.u.)	MTF (a.u.)	GIQE (a.u.)	TDI (a.u.)	SNR (a.u.)	MTF (a.u.)	GIQE (a.u.)	TDI (a.u.)	SNR (a.u.)	MTF (a.u.)	GIQE (a.u.)
32	168	0.3806	4.2267	32	211	0.3626	4.1934	32	247	0.3377	4.1465
16	97	0.4008	4.2367	16	125	0.3819	4.2036	16	149	0.3556	4.1566
4	25	0.4072	4.2298	4	34	0.388	4.1997	4	43	0.3614	4.1543

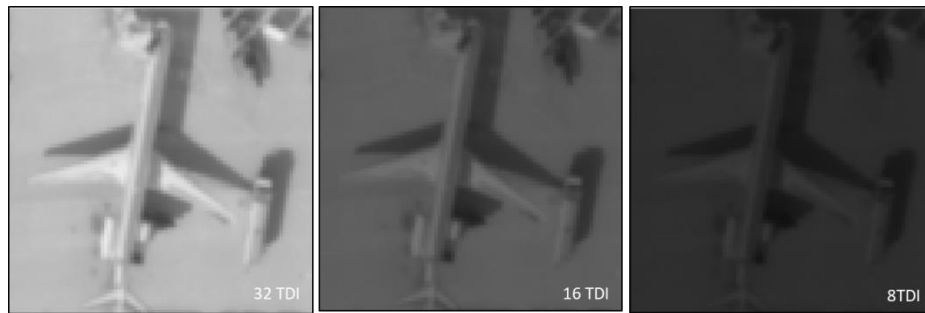


Figure 4.6. PAN band image simulations for 32 TDI step (left), 16 TDI step (middle) and 8 TDI step (right) degraded image simulations, respectively.

In Table 4.10 and Table 4.11, TDI GIQE degradation budgets with ± 0.3 error for PAN and MS bands are given. The image simulation of TDI degradations are given in Figure 4.6 for 32, 16 and 8 TDI steps. As can be seen from the image simulations image quality decreases as the TDI steps decrease. It should be noted that changes in the TDI steps increase SNR while decrease MTF.

Finally, GIQE budget simulations with ± 0.3 error for the cases which SZA changes with 10° are given in Table 4..

Table 4.12. GIQE budget with ± 0.3 error depending on SZA change.

PAN			Blue			Green			Red		
SZA ($^{\circ}$)	SNR (a.u.)	GIQE (a.u.)	SZA ($^{\circ}$)	SNR (a.u.)	GIQE (a.u.)	SZA ($^{\circ}$)	SNR (a.u.)	GIQE (a.u.)	SZA ($^{\circ}$)	SNR (a.u.)	GIQE (a.u.)
0	63	5.2140	0	133	4.2377	0	167	4.2042	0	190	4.1571
10	62	5.2139	10	126	4.2375	10	162	4.2042	10	190	4.1571
20	59	5.2136	20	120	4.2374	20	155	4.2041	20	182	4.1570
30	55	5.2132	30	110	4.2371	30	142	4.2039	30	168	4.1569
40	49	5.2124	40	97	4.2367	40	126	4.2036	40	150	4.1566
50	42	5.2113	50	81	4.2360	50	106	4.2030	50	127	4.1562
60	34	5.2093	60	64	4.2349	60	83	4.2021	60	99	4.1555
70	24	5.2053	70	46	4.2328	70	57	4.2003	70	68	4.1540

5 CONCLUSION

Within the scope of this thesis, an image quality evaluation program based on imaging chain model was developed for use in EO IPL design and system engineering applications. IQA program based on GIQE v.4 and imaging chain model was developed for this purpose. IQA program generates image simulations based on GIQE models that are calculated based on system design parameters and imaging conditions. An optimization module of EO IPL is introduced to IQA program. MTF degradation factors necessary to have the MTF values at NSF are calculated by degradation optimization function. Also an image quality budget case studies for platform stability errors, wavefront error, defocusing error and TDI level are made. Especially the image simulations and GIQE budget simulations demonstrate observable relations of the physical image quality parameters with image data. A spectral radiance library embedded in the IQA program was produced using the MODTRAN program in order to model imaging conditions based on two-path imaging geometry.

Preliminary design of an example EO IPL for earth observation imaging satellite was held by using image quality analysis and image simulations generated by IQA program iterations. 0.5 m PAN GSD is achieved with 600 km altitude. Telescope design includes a Cassegrain architecture with 69 cm primary mirror diameter, 12 m effective focal length and 0.1 obscuration ratio. TDI detector with 10 μm pixel size is used to collect multispectral image data from the scene. To avoid the non-linearities observed in IR band image simulations, multispectral band spectral regions are kept within visible bands with red, green and blue bands. 0.15 average PAN MTF for satellite level is calculated for example

EOIPL design. The satellite MTF calculations are ranging between 0.34 and 0.42 depending on wavelength and scanning direction. SNR defined in GIQE v4 is calculated as 79 for 32 TDI and 40 SZA. The SNR values of 168, 212 and 246 for blue, green and red bands are simulated, respectively. PAN band GIQE is calculated as 5.224 ± 0.3 , where blue, green and red band GIQE values are 4.233 ± 0.3 , 4.199 ± 0.3 , 4.152 ± 0.3 . The EOIPL design is made by taking the commercial submeter EOIPL architectures in the literature into consideration.

Among this thesis study, image quality characteristics of EOIPL systems operating in satellite systems have been analyzed and defined in with different image quality parameters. However, there are some topics that can be contributed to this thesis to improve the thesis. Following topics are considered to be a part of a PhD research project to work on.

This thesis is more likely to focus on the design of the IQA program based on imaging chain model and NIIRS scale. EOIPL design will be more optimized by using IQA simulation iterations. Also MTF degradation breakdown will have more detailed links of the imaging chain like sampling, electronics, atmosphere and display systems. On the other hand, IQA program is designed to evaluate the image quality characteristics of certain type of EOIPL architecture. Program will broaden its scope on different EOIPL architectures. An EOIPL design library will be generated which will be embedded in IQA program. Also IQA simulations are held for nadir cases. Different viewing angle IQA simulations will be added. Also a target detection case study algorithm will be linked up to IQA program. Target detection algorithm will be applied for the case studies where system degradations are applied on the payload level GIQE. At last optical design and tolerance of EOIPL will be held by using ZEMAX program. Also ZEMAX MATLAB communication will be added to IQA simulations.

REFERENCES

- [1] G. Dial, H. Bowen, F. Gerlach, J. Grodecki and R. Oleszczuk, "IKONOS satellite, imagery, and products," *Remote Sensing of Environment*, vol. 88, pp. 23-36, 2003.
- [2] H.-y. Yu, G. Cheng, X.-s. Ge and X.-p. Lu, "Object oriented land cover classification using ALS and GeoEye imagery over mining area," *Transactions of Nonferrous Metals Society of China*, vol. 21, no. 3, pp. 733-737, 2011.
- [3] B. C. Reed, J. F. Brown, D. VanderZee, T. R. Loveland, J. W. Merchant and D. O. Ohlen, "Measuring phenological variability from satellite imagery," *Journal of Vegetation Science*, vol. 5, pp. 703-714, 1994.
- [4] E. Gedik, U. Çınar, E. Karaman, Y. Yardımcı, U. Halıcı and K. Pakin, "A New Robust Method for Bridge Detection from High Resolution Electro-Optic Satellite Images," in *Geographic Object-Based Image Analysis*, Rio de Janeiro, 2012.
- [5] P. Coppo, L. Chiarantini and L. Alparone, "End-to-End Image Simulator for Optical Imaging Systems: Equations and Simulation Examples," *Advances in Optical Technologies*, vol. 2013, 2013.
- [6] P. Coppo, L. Chiarantini and L. Alparone, "Validation and Simulation Examples of an end-to-end simulator for Optical Imaging Systems," in *Remote Sensing*, Dresden, 2013.
- [7] K. Segl, F. Guanter, T. Kuester, C. Rogass and C. Mielke, "S2eteS: An End-to-End Modeling Tool for the Simulation of Sentinel-2 Image Products," *Transactions on Geoscience and Remote Sensing*, vol. 53, no. 10, pp. 5560-5571, 2015.
- [8] S. Wong and R. Jassemi-Zargani, "Predicting image quality of surveillance sensors," Defence Research and Development Canada, 2014.
- [9] R. D. Fiete, "Image Chain Analysis for Space Imaging Systems," *Journal of Imaging Science and Technology*, vol. 51, no. 2, pp. 103-109, 2007.
- [10] K. B. Alici, F. S. Öktem, Ö. Karıcı, A. S. Yılmaz and Ö. Selimoğlu, "Image Chain Simulation for Earth Observation Satellites," *IEE Journal of Selected*

Topics in Applied Earth Observations and Remote Sensing, pp. 1-10, 2019.

- [11] K. B. Alici, Ö. Karci, A. S. Yilmaz, C. Özdemir, F. S. Öktem and Ö. Selimoğlu, "OTF analysis of a spaceborne CMOS imaging sensor," in *8th International Conference on Recent Advances in Space Technologies* , İstanbul, 2017.
- [12] J. C. Leachtenauer and R. G. Driggers, *Surveillance and Reconnaissance Imaging Systems Modelling and Performance Prediction*, Norwood: Artech House, 2001.
- [13] J. M. Irvine, "National imagery interpretability rating scales (NIIRS): overview and methodology," in *Optical Science, Engineering and Instrumentation* , San Diego, 1997.
- [14] R. D. Fiete, *Modeling the Imaging Chain of Digital Cameras*, SPIE, 2010.
- [15] J. C. Leachtenauer, W. Malila, J. Irvine, L. Colburn and N. Salvaggio, "General Image-Quality Equation: GIQE," *Applied Optics*, vol. 36, no. 32, pp. 8322-8328, 1997.
- [16] S. A. Cota, J. T. Bell, R. H. Boucher, T. E. Dutton, C. J. Florio, G. A. Franz, T. J. Grycewicz, L. S. Kalman, R. A. Keller, T. S. Lomheim, D. B. Paulson and T. S. Wilkinson, "PICASSO: and end-to-end image simulation tool for space and airborne imaging systems," *Journal of Applied Remote Sensing*, vol. 4, 2010.
- [17] U. S. G. Survey, "USGS Earth Explorer," [Online]. Available: <https://earthexplorer.usgs.gov/>.
- [18] J. Müller, I. Gartner-Roer , P. Thee and C. Ginzler, "Accuracy assessment of airborne photogrammetrically derived high-resolution digital elevation models in a high mountain environment," *ISPRS Journal of Photogrammetry and Remote Sensing*, vol. 98, pp. 59-69, 2014.
- [19] J. Gao, *Digital Analysis of Remotely Sensed Imagery*, Mc-Graw-Hill, 2009.
- [20] G. D. Boreman, *Modulation Transfer Function in optical and electro-optical systems*, SPIE, 2001.
- [21] G. Holst, *CCD Arrays, Cameras and Displays*, SPIE, 1998.
- [22] J. D. Gaskill, *Linear Systems, Fourier Transforms and Optics*, Wiley & Sons, 1978.

- [23] S. W. Teare, *Optics using MATLAB*, SPIE, 2017.
- [24] G. Arfken, H. Weber and F. E. Harris, *Mathematical Methods for Physicists*, Elsevier, 2012.
- [25] K. T. Tang, *Mathematical Methods for Engineers and Scientists 3, Fourier Analysis, Partial Differential Equations and Variational Methods*, Berlin: Springer, 2007.
- [26] J. W. Goodman, *Introduction to Fourier Optics*, McGraw-Hill, 1996.
- [27] S. Köksal, İ. Canarlan and Ö. Duyar Çoşkun, "Image Quality Characterization of Earth Observation Electro-Optic Imagers Through PSF and MTF Analysis," in *Recent Advances in Space Technologies*, İstanbul, 2019.
- [28] I. O. f. Standardization, *ISO 12233 standard of : Photography-Electronic still picture imaging-resolution and spatial frequency responses 3rd edition*, SO, 2017.
- [29] R. D. Fiete, "Comparison of SNR image quality metrics for remote sensing systems," *Optical Engineering*, vol. 40, no. 4, pp. 574-585, 2001.
- [30] R. G. Driggers, M. H. Friedman and J. Nichols, *Introduction to Infrared and Electro-optics Systems*, Artech House, 2012.
- [31] J. W. Goodman, *Introduction to Fourier Optics*, Bogata: McGraw-Hill, 1996.
- [32] P. Hummel, "Apogeo Spatial," 6 October 201. [Online]. Available: <http://apogeospatial.com/accurate-ground-control/>.
- [33] R. Barakat and A. Houston, "Line Spread and Edge Spread Functions in the Presence of Off-Axis Aberrations," *Journal of The Optical Society of America*, vol. 55, no. 9, p. 1132, 1964.
- [34] R. R. Auelmann, "Image Quality Metrics," 2012.
- [35] R. Barakat and E. Blackman, "The expected value of the edge spread function in the prescence of random wavefronts," *Optics Communications*, vol. 8, no. 1, 1973.
- [36] S. T. Thurman and J. R. Fienup, "Analysis of general image quality equation," in *SPIE Defense and Security Symposium*, Orlando, 2008.
- [37] D. Griffith, "General Image Quality Equation (GIQE)," in *JACIE*, 2012, 2012.

- [38] J. R. Schott, *Remote Sensing, The Image Chain Approach*, New York: Oxford University Press, 2007.
- [39] J. M. Palmer and B. G. Grant, *The Art of Radiometry*, Washington: SPIE, 2010.
- [40] R. D. Fiete and T. Tantalò, "Comparison of SNR Image Quality Metrics for Remote Sensing Systems," *Optical Engineering*, vol. 40, no. 4, pp. 574-585, 2001.
- [41] G. Joseph, "How to Specify an Electro-optical Earth Observation Camera? A Review of the Terminologies Used and its Interpretation," *Journal of the Indian Society of Remote Sensing*, vol. 48, pp. 171-180, 2020.
- [42] F. Bu, D. Yao, Y. Qiu and B. Jiang, "The digital simulation of end-to-end imaging chain in optical remote sensing system based on MTF models," in *International Conference on Computer Science and Network Technology*, 2015.
- [43] R. D. Fiete and B. D. Paul, "Modeling the optical transfer function in the imaging chain," *Optical Engineering*, vol. 53, no. 8, 2014.
- [44] C. A. Gueymard, V. Lara-Fanego, M. Sengupta and Y. Xie, "Surface albedo and reflectance: Review of definitions, angular and spectral effects, and intercomparison of major data sources in support of advanced solar irradiance modeling over America," *Solar Energy*, vol. 182, pp. 194-212, 2019.
- [45] NASA, "Visible Earth by NASA," 10 July 2002. [Online]. Available: <https://visibleearth.nasa.gov/images/60636/global-albedo>. [Accessed 7 April 2002].
- [46] S. Adler-Golden, A. Berk, L. S. Bernstein, S. Richtsmeier, P. K. Acharya, M. W. Matthew, G. P. Anderson, C. L. Allred, L. S. Jeong and J. H. Chetwynd, "Flash, A Modtran4 Atmospheric Correction Package for Hyperspectral Data Retrievals and Simulations," in *Airborne Visible/Infrared Imaging Spectrometer Workshop*, 1998.
- [47] K. Staenz, D. J. Williams and B. Walker, "Surface Reflectance Retrieval From Aviris Data Using Six-Dimensional Look-Up Table," in *Airborne Visible/Infrared Imaging Spectrometer Workshop*, 1996.
- [48] D. J. Williams, A. Royer, N. T. O'Neill, S. Achal and G. Weale, "Reflectance Extraction from CASI Spectra Using Radiative Transfer Simulations and a

Rooftop Irradiance Collector," *Canadian Journal of Remote Sensing*, vol. 18, no. 4, pp. 251-261, 1992.

- [49] ESA, "eoPortal Directory - Mission Database," [Online]. Available: <https://directory.eoportal.org/web/eoportal/satellite-missions/a>.
- [50] H. J. Kramer, *Observation of the Earth and its Environment*, Springer, 2002.
- [51] J. Cheng, *The Principles of Astronomical Telescope Design*, Springer, 2009.
- [52] J. Bai, Y. Sun, L. Chen, Y. Fend and J. Liu, "EO Sensor Planning for UAV Engineering REconnaisance Based on NIIRS and GIQE," *Applied Mathematics for Engineering Problems in Biomechanics and Robotics*, vol. 2018, 2018.
- [53] S. Han, J. Kerekes, S. D. Higbee and L. Siegel, "Simulation Techniques for Image Utility Analysis," in *Algorithms and Technologies for Multispectral, Hyperspectral, and Ultraspectral Imagery*, Orlando, 2018.
- [54] R. D. Fiete, *Formation of a Digital Image, The Imaging Chain Simplified*, Bellingham: SPIE, 2012.
- [55] A. Berk, L. S. Bernstein and D. C. Robertson, "Modtran: A Moderate Resolution Model for Lowtran," United States Air Force, Air Force Geophysics Laboratory, Massachusetts, 1987.
- [56] T. Dalsa, "Multispectral Imaging," [Online]. Available: <https://www.teledynedalsa.com/en/learn/markets-and-applications/aerospace/multispectral/>.
- [57] J. Müller , *Evaluation of different airborne high-resolution digital elevation products in a high alpine environment*, Bonn: Rheinische Friedrich Wilhelms Universität Bonn Department of Geography, 2011.
- [58] S. Wong and R. Jassemi-Zargani, "Predicting image quality of surveillance sensors," Defence Research and Development Canada, Ottawa, 2014.
- [59] T. S. Thurman and J. R. Fienup, "Analysis of the general image quality equation," in *Visual Information Processing*, 2008.
- [60] T. Maurer, "How to PAN-sharpen Images Using the Gra-Schmidt PAN-sharpen Method - A Recipe," in *Int. Arch. Photogramm. Remote Sens.*

Spatial Inf. Sci., Hannover, 2013.

[61] MATLAB, "Introduction to Wavelet Families," MATLAB, [Online]. Available: <https://www.mathworks.com/help/wavelet/gs/introduction-to-the-wavelet-families.html>.

[62] D. Globe. [Online]. Available: <https://www.digitalglobe.com/>.

APPENDIX-A PAPERS PUBLISHED FROM THESIS WORK

Image Quality Characterization of Earth Observation Electro-optic Imagers through PSF and MTF Analysis

Sevi Köksal
Turkish Aerospace Industries, Inc.
Optics and Radar Systems
Ankara, Turkey
sevi.koksal@tai.com.tr

Izzet Canarslan
Turkish Aerospace Industries, Inc.
Optics and Radar Systems
Ankara, Turkey

Özlem Duyar Coşkun
Hacettepe University
Thin Film Preparation and
Characterization Laboratory, Physics
Engineering Department
Ankara, Turkey

Abstract—Modulation Transfer Function and Point Spread Function relationships between components of a conceptual imager were evaluated during optical system engineering applications. Full width half maximum of the flux density point spread function and relative edge response were used for predicting imaging quality performance on the contrast transfer. FWHM of flux density PSF and RER are calculated as 1.7 pixel displacement and 0.2541 for modulation transfer function of a conceptual imager with obscured aperture geometry and contiguous CCD array detector operating in PAN band. MTF sub-components are established to predict system modulation transfer quality of the imaging satellite. MTF model consists of diffraction limit for aperture geometry function, wave front error caused degradation, sampling and detector footprint for contiguous focal-plane array detector architecture. To predict the line of sight stability budget linear motion error and jitter error degraded contrast transfer quality functions are evaluated. 0.4 μ rad jitter value expands flux density PSF FWHM by 1.9 pixel displacement and degrades RER to 0.2224 while linear motion error of 8 mrad/s expands flux density PSF FWHM by 1.5 pixel displacement and degrades RER to 0.2501. FWHM of flux density PSF expansion of 0.5 pixel displacement and 0.2212 RER are observed for 0.2 λ wavefront error input value. MTF Kernel with 3.5 noise gain increased the RER value FWHM of flux density PSF to 0.2680 and 0.3 pixel displacement.

Keywords— PSF, MTF, RER, image quality, electro-optic imager

I. INTRODUCTION

Evaluation of the static and dynamic condition image quality performance of the earth observation electro-optic imagers become more of an issue on high quality imager design and system engineering applications. Image quality analysis of electro-optic imagers provides important information to image analysts, imager designers and system engineers who are working on following applications [1, 2, 3, 4, 5]:

- Selection of the right subsystem components with similar metrics during design process
- Performance prediction evaluation of the electro-optic imager depending on the line of sight pointing stability and jitter effects
- Calibration of the electro-optic imager during mission activities with pre-simulated system calibration parameters
- Generation of the compensation Kernel matrixes which will be used during image processing studies

Relative Edge Response (RER) parameter represents the contrast (sharpness) transfer quality degradation of the object irradiance distribution due to the subsystem components of the imager [2]. Modulation Transfer Function (MTF) is simulated to calculate RER parameter.

Object plane irradiance distribution can be expressed as the decomposition into scaled and shifted delta functions in which each representing a point source on the object plane [6]. Flux Density Point Spread Function (PSF) is defined as the projection of the blurred point source object into the image plane [7, 8, 9]. In addition to the MTF and RER analysis full width half maximum (FWHM) of the flux density PSF measurement and simulations are also used in image quality analysis studies [10, 11]. There are significant studies on image quality simulation in literature [3, 4, 5, 12].

The goal of this study is to analyze image quality of linear space invariant and incoherent ideal earth observation electro-optic imager on the contrast transfer quality scope through flux density point spread function, modulation transfer function and relative edge response value simulations. 2D flux density point spread function, 2D modulation transfer function and relative edge response parameter value simulation program for a conceptual imager design is developed using MATLAB environment. After the development of imager 2D-PSF model platform stability error and wave front error budget estimations for contrast transfer quality are made using the program.

II. CALCULATION METHOD

A. Calculation Method of the Flux Density Point Spread Function

Image quality degradation due to the contrast transfer function is evaluated by examining the relationship between the object irradiance distribution and image irradiance distribution functions. Object plane can be defined as the delta function decomposition of the irradiance distribution function. Scaling and shifting properties of delta function make it possible to present sample irradiance distribution into a 2D matrix format. As the object irradiance distribution matrix pass through each element of the electro-optic imager, distribution function changes and finally it becomes image irradiance distribution. In spatial domain the relationship between the image irradiance distribution and the object irradiance distribution can be defined as a

convolution equation. Image plane irradiance distribution of a linearly shift invariant incoherent imager can be expressed as the superposition of sampled object points that exposed to individual flux density point spread functions. As the FWHM of the PSF function increases image quality degrades in the image plane. Imaging equation in spatial domain can be defined with convolution integral as [13, 14]:

$$g(x, y) = PSF(x, y) ** o(x, y) \quad (1)$$

Point source objects are blurred because of the image quality degradation after the projection from the object plane into the image plane.

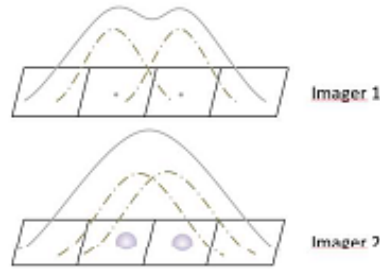


Fig. 1. Point source projection examples in two imagers with different image quality characteristics

Examples of the point source projection in image plane detector surface array with different image quality characteristics are given in Fig. 1 [15]. Image quality degrades more for the second imager. As the FWHM of the blurred PSF increases sampling intervals of the detector pixels become deficient for detecting separate two point sources and imager becomes unable to sample the image irradiance distribution profile.

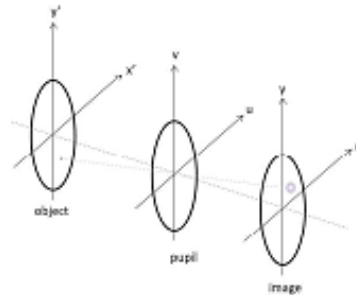


Fig. 2. Image formation geometry

Image formation geometry is given in Fig. 2. Diffraction integral depending on the pupil geometry function can be expressed as [14]:

$$U_o(x, y) = \tilde{C} \tilde{f}_p \iint_a p(u, v) e^{2\pi i(xu + yv)} du dv \quad (2)$$

where $U_o(x, y)$ is the amplitude point spread function at a point on the image plane, $p(u, v)$ is the pupil geometry function, \tilde{C} is complex constant, \tilde{f}_p is the function of coordinates of the point on the image plane, a indicates the surface that the double integral is taken over. Pupil function

is zero everywhere beyond the pupil aperture geometry [14, 13].

Diffraction integral is in a similar mathematical form with Fourier Integral. Relationship between the pupil function geometry and the amplitude point spread function can be expressed as a Fourier Transform. Flux density point spread function is the magnitude squared of the amplitude phase transfer function. Flux density point spread function can be expressed as [14, 16]:

$$PSF(x, y) = [U_o(x, y)][U_o^*(x, y)] = |U_o(x, y)|^2 \quad (3)$$

$$PSF(x, y) = |FT(p(u, v))|^2 \quad (4)$$

Flux density point spread function can also be expressed as the normalized autocorrelation of the pupil function [17, 14, 18]. Imaging equation convolution integral is defined as:

$$g(x, y) = \iint PSF(x, y; x', y') o(x', y') dx' dy' \quad (5)$$

where $g(x, y)$ is the image plane irradiance distribution, $o(x, y)$ is the object plane irradiance distribution, $PSF(x, y)$ is the flux density point spread function.

B. Spatial Frequency Domain Imaging Equation & Modulation Transfer Function Relation

Fourier transform of the irradiance distribution gives decomposition of the irradiance distribution data into its sinusoidal sub-components with different spatial frequencies. Image quality degrading factors such as optical system limits the maximum spatial frequency that imager can sample. Flux density point spread function acts like a low pass optical filter on object irradiance spectrum. Imaging equation in spatial frequency domain can be expressed as the Fourier transform of equation (1) as [19, 20]:

$$G(f_x, f_y) = OTF(f_x, f_y) O(f_x, f_y) \quad (6)$$

$$FT(PSF(x, y)) = OTF(f_x, f_y) \quad (7)$$

$$MTF(f_x, f_y) = |OTF(f_x, f_y)| \quad (8)$$

where $G(f_x, f_y)$ is the image irradiance spectrum, $OTF(f_x, f_y)$ is the optical transfer function, $O(f_x, f_y)$ is the object irradiance spectrum, f_x and f_y are the spatial frequency components along orthogonal directions to the imaging axis. Fourier Transform of flux density point spread function defined as the Optical Transfer Function (OTF). Absolute value of optical transfer function gives the Modulation Transfer Function (MTF).

C. Calculation Method of the Modulation Transfer function & Relative Edge Response

Line Spread Function (LSF) is defined as the irradiance density distribution in the image plane of a line source, while point spread function is the irradiance density distribution in the image plane of a point source [14]. LSF can be expressed as 1D convolution of 2D source object with a delta function point source along one dimension [1, 11].

$$LSF(x) = \delta(x) 1(y) ** PSF(x, y) \quad (9)$$

$$LSF(x) = \int_{-\infty}^{\infty} PSF(x', y') dy' \quad (10)$$

Fourier Transform of both sides of the equation (10) yields to the relation between LSF and MTF as equation [1, 20, 21, 11]:

$$MTF(f_x) = |FT(PSF(x))| \quad (11)$$

$$MTF(f_x) = \int_{-\infty}^{\infty} LSF(x) \exp(-2i\pi f_x x) dx \quad (12)$$

One dimensional image irradiance distribution along the sharp edge transition of an imager to a knife edge target object is defined as Edge Response (ER). The relationship between LSF and ER is given as [1, 21]:

$$ER(x) = \int_{-\infty}^x LSF(x') dx' \quad (13)$$

If MTF LSF relation definition in equation (12) is used, ER can be defined in terms of MTF as [1]:

$$ER(x) = \int_{-\infty}^x \left[\int_{-\infty}^{\infty} MTF(f_x) \exp(2i\pi f_x x') df_x \right] dx' \quad (14)$$

$$ER(x) = 0.5 + \frac{1}{\pi} \int_0^{f_{xc}} \frac{MTF(f_x) \sin(2\pi f_x x)}{f_x} df_x \quad (15)$$

RER definitions in image quality evaluation analysis are commonly defined in terms of number of pixel offset from the knife edge object along the edge transition direction [1]. If the following terms in the equation (16), (17) and (18) introduced to the equation (15) ER depending on number of pixel offset from the edge defined as equation (19) while RER depending on number of pixel offset from the edge can be expressed as equation (20) and (21) [1]:

$$\varepsilon = \frac{x}{p} \quad (16)$$

$$Y_{cut} = \frac{f_{opt}}{f_{det}} = \frac{1}{Q} \quad (17)$$

$$\gamma = \frac{f}{f_{det}} \quad (18)$$

$$ER(\varepsilon) = 0.5 + \int_0^{\frac{1}{Q}} MTF(\gamma) \sin(\gamma) \frac{\sin(2\pi\gamma\varepsilon)}{\pi\gamma} d\gamma \quad (19)$$

$$RER = ER(0.5) - ER(-0.5) \quad (20)$$

$$RER = 2 \int_0^{\frac{1}{Q}} \frac{MTF(\gamma) \sin(\pi\gamma)}{\pi\gamma} d\gamma \quad (21)$$

D. Calculation Method of the Imager System MTF Subcomponents

Diffraction MTF was obtained by the normalized autocorrelation of the exit pupil geometry function of the system [16, 17]. Optical cutoff spatial frequency of the system is defined as [16]:

$$f_{opt} = \frac{1}{\lambda f_n} \quad (22)$$

where f_n the f number of the optical geometry and λ is the wavelength in millimeters.

Sampling cutoff spatial frequency of the system is expressed as [22]:

$$f_{samp} = \frac{1}{p} \quad (23)$$

where p is pixel pitch size.

Detector MTF for contiguous focal-plane array can be obtained by [16]:

$$MTF_{sampling}(f_x, f_y) = \left| \text{sinc} \left(\frac{f_x}{f_{samp_x}} \right) \right| \left| \text{sinc} \left(\frac{f_y}{f_{samp_y}} \right) \right| \quad (24)$$

$$MTF_{footprint}(f_x, f_y) = \left| \text{sinc} \left(\frac{f_x}{f_{samp_x}} \right) \right| \left| \text{sinc} \left(\frac{f_y}{f_{samp_y}} \right) \right| \quad (25)$$

$$MTF_{detector}(f_x, f_y) = MTF_{sampling}(f_x, f_y) MTF_{footprint}(f_x, f_y) \quad (26)$$

Wave front error MTF degradation caused by optical design and alignment error procedures is calculated as [3]:

$$MTF_{WFE}(f_r) = \exp \left(- \left(\frac{2\pi\delta}{\lambda} \right)^2 \left[1 - \exp \left(- \frac{\left(\frac{f_r}{f_{opt}} \right)^2}{\gamma_{ripple}} \right) \right] \right) \quad (27)$$

$$f_r = \sqrt{f_x^2 + f_y^2} \quad (28)$$

where δ is rms ripple amplitude, f is spatial frequency, f_x spatial frequency along x direction, f_y spatial frequency along y direction, γ_{ripple} is ripple correlation scale.

Motion errors on the imaging axis result in image quality degradation. Linear motion error caused MTF degradation is defined as [16, 23]:

$$MTF_{smear}(f_x, f_y) = \left| \text{sinc}(f_x v_{imgx} \tau_e) \right| \left| \text{sinc}(f_y v_{imgy} \tau_e) \right| \quad (29)$$

where v_{imgx} is line of sight mismatch velocity and τ_e is exposure time.

Vibrational motion error caused jitter MTF degradation is defined as [16]:

$$MTF_{jitter}(f_r) = \exp \left(- \frac{2\pi \left(\frac{f_r}{f_{samp_r}} \right) \sigma_{rms}}{IFOV} \right) \quad (30)$$

where σ_{rms} is rms jitter amplitude, IFOV is instantaneous field of view.

For edge sharpening simple 3x3 Kernel method compensated MTF can be calculated by [24]:

$$MTFC(f_x, f_y) = a + 2b \left(\cos 2\pi \frac{f_x}{f_{samp_x}} + \cos 2\pi \frac{f_y}{f_{samp_y}} \right) + 4c \left(\cos 2\pi \frac{f_x}{f_{samp_x}} + \cos 2\pi \frac{f_y}{f_{samp_y}} \right) \quad (31)$$

$$MTFC_{kernel} = \begin{bmatrix} c & b & c \\ b & a & b \\ c & b & c \end{bmatrix} \quad (32)$$

$$a + 4b + 4c = 1 \quad (33)$$

$$G = \sqrt{a^2 + 4b^2 + 4c^2} \quad (34)$$

where a , b and c is MTFC 3x3 Kernel matrix elements, G is noise gain.

III. CONTRAST TRANSFER QUALITY SIMULATION RESULTS DERIVED BY MTF, PSF AND RER MODELS

Contrast transfer quality simulations are developed based on MTF models for linearly shift invariant incoherent ideal imager. 2D MTF, 2D PSF and RER models are evaluated during optical system engineering analysis. As system MTF

degradation subcomponents, diffraction, aberration, sampling, detector footprint, linear motion error and jitter errors are considered. Analysis were made for a conceptual imager with circularly symmetric obscured optics geometry and contiguous CCD array detector operating on PAN band. Reference assumptions and parameters that made during conceptual imager are listed in the Table I and Table II.

TABLE I. CONCEPTUAL IMAGER DESIGN ASSUMPTIONS

Feature	Assumption
Optics	obscured aperture
Detector	contiguous CCD array
MTFC Method	3x3 Kernel MTFC Method

TABLE II. CONCEPTUAL IMAGER DESIGN PARAMETERS

Quantity	Assumption
aperture diameter (mm)	1000
obscuration rate	0.3
focal length (m)	15
central wavelength (nm) (average of PAN band)	650
pixel size (μm)	7
ground sampling distance (m)	0.5
exposure time (μs)	100
ripple correlation scale	0.0746

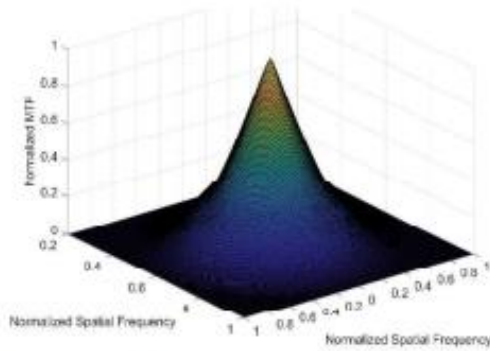


Fig. 3. Static system 2D-MTF simulation result

Static system two dimensional MTF simulations are evaluated by considering diffraction, detector sampling and detector footprint effects on spatial frequency limit. Equations (22) to (26) were calculated in simulation program. 2D-MTF simulation result of the conceptual imager design defined in Table I and Table II is given in Fig. 3. RER value for the imager is calculated as 0.2541.

Two dimensional flux density PSF simulations were evaluated by using the Fourier Transform relations between MTF and flux density PSF specified in equations (7) and (8). 2D flux density PSF simulation result of the conceptual imager design defined in Table I and Table II is given in Fig. 4. Image quality degradation margins were estimated by calculating the FWHM of the flux density PSF model and RER model results.

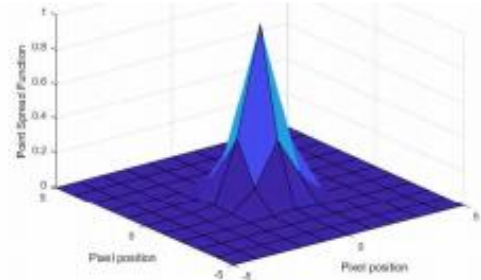


Fig. 4. Static system flux density PSF simulation results

Flux density PSF simulations are evaluated for estimating the image quality degradation budgets of the imager system under degradation and restoration effects. Platform stability and wave front errors are considered during system degradation image quality budget estimations. 3x3 Kernel Method was used for contrast quality restoration.

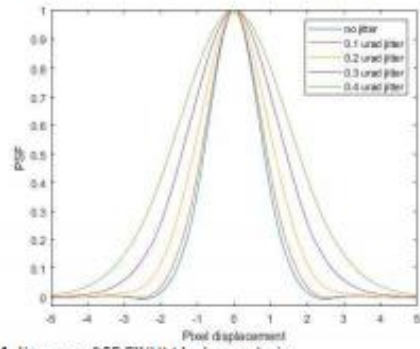


Fig. 5. Jitter error PSF FWHM budget analysis

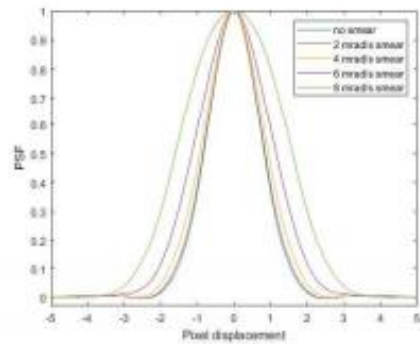


Fig. 6. Linear motion error PSF FWHM budget analysis

Jitter value input for the imager is increased from 0.1 μrad to 0.4 μrad by 0.1 μrad steps. Static system FWHM of flux density PSF is calculated as 1.70 pixel displacement before any degradation factors by using equation (30). It is observed from Fig. 5 that for of 0.4 μrad value, flux density PSF FWHM expands 1.9 pixel displacement. Degraded RER value is calculated as 0.2224 by using equation (21). On the other hand linear motion error input for the program is increased from 2 $\mu\text{rad/s}$ to 8 mrad/s by 0.2 mrad/s steps.

Flux density PSF FWHM expansion of 1.5 pixel displacement and degraded 0.2501 RER value for 8 mrad/s linear motion error are calculated by using equations (29) and (21).

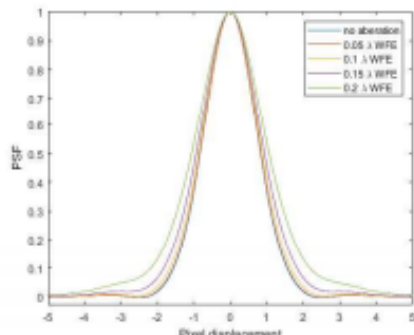


Fig. 7. WFE PSF FWHM budget analysis

System contrast transfer quality degradation due to the wave front error calculations is given in Fig. 7. WFE value input is increased from 0.05λ to 0.2λ by using equations (27) and (28). FWHM PSF expansion of 0.5 pixel displacement is observed for 0.2λ WFE input value. Degraded RER value is calculated as 0.2212 by using equation (21).

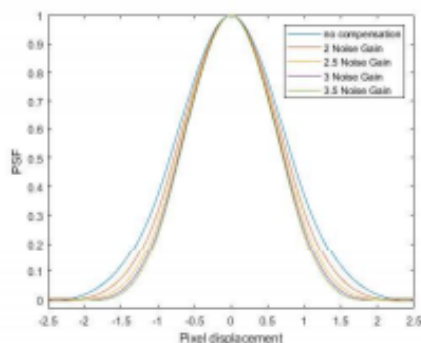


Fig. 8. MTFC PSF FWHM budget analysis

As contrast transfer quality restoration method 3×3 Kernel MTF compensation method is used. Four MTFC Kernel Matrix with increasing noise gain values are implemented to two dimensional MTF matrix of the system by using equation (31) to (34). For gradual increase of 0.5 noise gain value edge sharpening is put in to the imager contrast transfer quality budget. 0.3 pixel displacement of restoration for 3.5 noise gain value is observed from Fig. 8. RER value is increased to 0.26801.

IV. CONCLUSION

A contrast transfer quality simulation program is developed using MATLAB environment for future optical system engineering applications. Contrast transfer quality predictions of a conceptual imager design are made. Analysis results are useful to understand the trades and limits of the imager product in the early steps of the project timeline. Also these calculations developed a common metric for the

evaluation of the contrast transfer quality of different imager system subcomponents. During the calculations two dimensional MTF, flux density PSF and RER values are calculated for a circularly symmetric conceptual imager with obscured aperture geometry and contiguous CCD array detector. For the static system MTF model diffraction limit for the obscured aperture geometry, sampling and detector footprint of a contiguous focal-plane array detector are considered. FWHM of the circularly symmetric flux density PSF is calculated as 1.7 pixel displacements while the RER value is calculated as 0.2541. For the platform stability error budget estimations jitter and linear motion errors are considered. For jitter value of $0.4 \mu\text{rad}$ flux density PSF FWHM expanded by 1.9 pixel displacement and RER is degraded to 0.2224. On the other hand 8 mrad/s linear motion error degrades RER to 0.2501 while flux density PSF FWHM is expanded by 1.5 pixel displacement. 0.2 λ wavefront error expanded the flux density PSF FWHM by 1.5 pixel displacement and degrades RER to 0.2212. As the sharpening method 3×3 MTFC Kernel Method is applied. For a MTFC Kernel with 3.5 noise gain RER value increased to 0.2680 and flux density PSF is decreased by 0.3 pixel displacements.

ACKNOWLEDGMENT

The supports of the entire Turkish Aerospace-Space Systems Group and Hacettepe Physics Engineering Department-Thin Film Preparation and Characterization Laboratory are gratefully acknowledged.

REFERENCE

- [1] S. Wong and R. Jassemi-Zargani, "Predicting image quality of surveillance sensors," Defence Research and Development Canada, 2014.
- [2] R. D. Fieta and B. D. Paul, "Modeling the optical transfer function in the imaging chain," *Optical Engineering*, vol. 53, no. 8, 2014.
- [3] S. A. Cota, J. T. Bel, R. H. Boucher, T. E. Dutton, C. J. Florio and G. A. Franz, "PICASSO - An End-to-End Image Simulation Tool for Space and Airborne Imaging Systems," *Remote Sensing System Engineering*, vol. 4, no. 1, 2008.
- [4] P. Coppo, L. Chiarantini and L. Alparone, "End-to-End Image Simulator for Optical Imaging Systems: Equations and Simulation Examples," *Advances in Optical Technologies*, vol. 2013.
- [5] K. Fliegel, "Modeling and Measurement of Image Sensor Characteristics," *Radioengineering*, vol. 13, no. 4, pp. 27-34, 2004.
- [6] S. W. Smith, *The Scientist and Engineer's Guide to Digital Signal Processing*, San Diego: California Technical Publishing, 1999.
- [7] R. D. Fieta, "Image Chain Analysis for Space Imaging Systems," *Journal of Imaging Science and Technology*, vol. 51, no. 2, pp. 103-109, 2007.
- [8] W. W. Arrasmith, *Systems Engineering and Analysis of Electro-Optical and Infrared Systems*, CRC Press, 2015.
- [9] R. Ryan, B. Baldrige, R. A. Schowengerdt, T. Choi, D. L. Helder and S. Blonski, "IKONOS spatial resolution and image interpretability characterization," *Remote Sensing of Environment*, vol. 88, pp. 37-52, 2003.
- [10] J. E. Harvey and A. Krywonas, "A System Engineering Analysis of Image Quality," in *Current developments in Lens Design and Optical Systems Engineering*, San Diego, 2000.
- [11] S. Lashansky, S. Mansbach, M. Berger, T. Karasik and M. Bin-Nun, "Edge Response Revisited," in *Infrared Imaging Systems: Design, Analysis, Modeling, and Testing XIX*, Orlando, 2008.
- [12] F. Bu, Y. Qiu, D. Yao and B. Jiang, "The Digital Simulation of End-To-End Imaging Chain in Optical Remote Sensing System Based on MTF Models," in *International Conference on Computer Science and*

- Network Technology*, Harbin, 2015.
- [13] J. W. Goodman, *Introduction to Fourier Optics*, McGraw-Hill, 1996.
- [14] S. C. Williams and A. O. Becklund, *Introduction to the Optical Transfer Function*, Washington: SPIE, 2002.
- [15] R. D. Fieta, "Image quality and FN/p for remote sensing," *Optical Engineering*, vol. 38, no. 7, 1999.
- [16] G. D. Boreman, *Modulation Transfer Function in Optical and Electro-Optical Systems*, Washington: SPIE, 2001.
- [17] S. W. Teare, *Optics using MATLAB*, Washington: SPIE, 2017.
- [18] J. Macdonald, "The calculation of the optical transfer function," *Optica Acta*, vol. 18, no. 4, pp. 269-290, 1971.
- [19] I. Powell, "The Calculation of the Optical Transfer Function for Systems with Central Obscuration," *Optical Acta*, vol. 21, no. 6, 1974.
- [20] S. VITEK and H. Jiri, "Modeling of Imaging Systems in Matlab," *Radioengineering*, vol. 12, no. 4, pp. 55-57, 2003.
- [21] A. Manzanares, M. L. Calvo, M. Chevalier and V. Lakshminarayanan, "Line Spread Function proposed by W. H. Steel," *Applied Optics*, vol. 36, no. 19, pp. 4362-4366, 1997.
- [22] A. Eckardt and R. Reulke, "On the Design of High Resolution Imaging Systems," in *ISPRS*, Hannover, 2017.
- [23] S. L. Smith, J. Mooney, T. A. Tantalo and R. D. Fieta, "Understanding image quality losses due to smear in high-resolution remote sensing imaging systems," *Optical Engineering*, vol. 38, no. 5, pp. 821-826, 1999.
- [24] R. D. Fieta, *Modeling the imaging chain of digital cameras*, Bellingham: SPIE, 2010.